UNIVERSIDADE FEDERAL DE SANTA CATARINA
CAMPUS FLORIANÓPOLIS
PROGRAMA DE PÓS-GRADUAÇÃO EM ENGENHARIA MECÂNICA

ADRIANO DE SOUZA PINTO PEREIRA

TiC-REINFORCED INCONEL X750 METAL MATRIX COMPOSITE PRODUCED THROUGH LASER DIRECTED ENERGY DEPOSITION

FLORIANÓPOLIS
2020

TiC-REINFORCED INCONEL X750 METAL MATRIX COMPOSITE PRODUCED THROUGH LASER DIRECTED ENERGY DEPOSITION

Dissertação submetida ao Programa de Pós-Graduação em Engenharia Mecânica da Universidade Federal de Santa Catarina para a obtenção do Grau de Mestre em Engenharia Mecânica.
Orientador: Prof. Dr. Eng. Milton Pereira
Coorientador: Prof. Dr.-Ing. Walter Lindolfo Weingaertner

Florianópolis
2020

Ficha de identificação da obra elaborada pelo autor,
através do Programa de Geração Automática da Biblioteca Universitária da UFSC.

Pereira, Adriano de Souza Pinto
TiC-Reinforced Inconel X750 Metal Matrix Composite Produced through Laser Directed Energy Deposition / Adriano de Souza Pinto Pereira ; orientador, Milton Pereira, coorientador, Walter Lindolfo Weingaertner, 2020.
122 p.

Dissertação (mestrado) - Universidade Federal de Santa Catarina, Centro Tecnológico, Programa de Pós-Graduação em Engenharia Mecânica, Florianópolis, 2020.

Inclui referências.

1. Engenharia Mecânica. 2. Metal Matrix Composites. 3. Directed Energy Deposition. 4. Ni-base Superalloys. 5. Laser Materials Processing. I. Pereira, Milton. II. Lindolfo Weingaertner, Walter. III. Universidade Federal de Santa Catarina. Programa de Pós-Graduação em Engenharia Mecânica. IV. Título.

Adriano de Souza Pinto Pereira

TiC-Reinforced Inconel X750 Metal Matrix Composite Produced through Laser Directed Energy Deposition

O presente trabalho em nível de mestrado foi avaliado e aprovado por banca examinadora composta pelos seguintes membros:

Prof. Dr. Eng. Carlos Enrique Niño Bohórquez
Universidade Federal de Santa Catarina

Prof. Dr. Eng. Rodrigo Perito Cardoso
Universidade Federal de Santa Catarina

Certificamos que esta é a **versão original e final** do trabalho de conclusão que foi julgado adequado para obtenção do título de mestre em Engenharia Mecânica pelo Curso de Pós-Graduação em Engenharia Mecânica da Universidade Federal de Santa Catarina.

Documento assinado digitalmente
Jonny Carlos da Silva
Data: 24/06/2020 16:32:42-0300
CPF: 514.515.064-49

Prof. Dr. Eng. Jonny Carlos Da Silva
Coordenador do Programa

Documento assinado digitalmente
Milton Pereira
Data: 24/06/2020 15:01:11-0300
CPF: 823.484.489-04

Prof. Dr. Eng. Milton Pereira
Orientador

Prof. Dr.-Ing. Walter Lindolfo Weingaertner
Co-orientador

Florianópolis, 29 de Abril, 2020.

À minha família.

É baseado em seu apoio que me ergo.

ACKNOWLEDGEMENTS

I do not consider myself capable of expressing my gratitude as well as some of my colleagues have done in the past, therefore, I tried my best mentioning all who helped me, keeping it simple so my words do not lose meaning.

Thanks to Prof. Dr.-Ing. Walter L. Weingaertner and Prof. Dr. Eng. Milton Pereira for the trust placed in me, the orientation, the lectures, and all the opportunities provided along all these years at the LMP. A special thanks also goes to Prof. Dr.-Ing. Ulrich Tetzlaff and Prof. Dr.-Ing. Marcio Celso Fredel, without their support this master thesis would not be possible.

I am grateful for the support provided by Universidade Federal de Santa Catarina, Technische Hochschule Ingolstadt, Instituto SENAI de Inovação em Sistemas de Manufatura e Processamento a Laser, Villares Metals S.A, and the founding agencies CAPES and CNPq; while also for the help gotten directly from the LCME, Cermat, Labmat, LabConf, and Labsolda, and of course their excelling staffs.

I have met many that helped me to trail this path, some became dear friends, others invaluable co-workers, all have my sincere gratitude. Listed in no specific order are Petters, Volpato, Ferreira, Max, Jurandir, Rafael Nunes, Rodolfo, Wei Lin, Francisco R., Claudio, Jhonattan, L. Heeman, Manuela, Georges Lemos, Ricardo Vilain, Cerruti, Paiva, Michel, Ricardo Knochblauch, Fernando Bordin, Bruno Borges, Fred, Calil, Thaison, Tiago Zilio, Gustavo Truppel, Cledenir, João Osorio, Fernanda, Bruno, and Luam, if I have forgotten a name, come to me that I will thank you personally, be this for the better or not. Honorable mentions go to those that had to handle all the stupid pranks and dull jokes.

There are not enough words to thank the support and happiness my family has given me; they know how much I owe and praise them. One day I hope to do for them as much as they have done for me. Lastly, most thanks go to Denise, for everything.

“All we have to decide is what to do with the time that is given us.”

(J.R.R. Tolkien, 1954)

RESUMO

Compósitos de matriz metálica, ou MMCs, são geralmente classificados como materiais de alto desempenho que são utilizados em aplicações aeroespaciais. No desenvolvimento de tais materiais, pesquisadores exploram a estabilidade térmica de reforços cerâmicos para aumentar as propriedades mecânicas de ligas pré-existentes. Recentemente, com a disseminação de processos de manufatura aditiva baseados na tecnologia a laser (LAM), um novo e amplo espectro de MMCs parece estar ao alcance. Neste trabalho pesquisou-se a possibilidade de se reforçar a superliga de níquel Inconel X750 através da inserção de 15% vol de partículas de carboneto de titânio (TiCp), usando deposição por energia direcionada a laser (DED-L), um processo LAM. Os objetivos principais deste trabalho são viabilizar e analisar a deposição do pó de baixa de processabilidade que foi utilizado como matéria-prima, e caracterizar microestruturalmente o material depositado. DED-1 deste particulado foi possível até certo ponto, dada a baixa fluidez do pó. Tentativas de facilitar o fluxo de pó, como um novo silo alimentador com ângulo interno mais acentuado, foram ineficazes. Porém, métodos para analisar a estabilidade do processo, com base em fotogrametria e em grandezas denominadas fatores de estabilidade, mostraram-se eficazes na determinação de que uma inserção de no mínimo 70 J.mm-1 é necessária para o processamento nas condições testadas. Estes métodos também indicaram que para pós coesivos de baixa fluidez, taxas de alimentação de pó mais baixas, na ordem de 2,5 g/min, provavelmente aumentam a estabilidade do processo. Apesar das dificuldades de escoabilidade descritas, estabilidade de deposição suficiente foi obtida para permitir DED-L, subsequente avaliação microestrutural e análise da relação entre os parâmetros de processo e as grandezas relacionadas aos cordões depositados. As relações aqui reunidas seguem o descrito na literatura, mostrando que este particulado se comportará conforme exigido uma vez que o problema de fluxo de pó for resolvido. Nos cordões analisados, porosidade e trincas não foram encontradas por MO ou MEV. Segregações ou aglomerações das TiCp também não foram detectadas em nenhuma condição de processamento. Análises EDS-MEV de baixo vácuo e EDS-FEG-MEV identificaram que nióbio oriundo da matriz de Inconel X750 se concentrou ao redor de todas as TiCp. A análise DRX realizada, indicou quais foram os prováveis compostos resultantes da reação do Nb, sendo eles NbC e (Nb,Ti)C. Complementarmente, a composição química da matriz foi mensurada por EDS-MEV e comparada com a do pó de Inconel X750, demonstrando igualdade nominal entre as composições. Análises por MET e FEG-MEV mostraram que os precipitados γ` foram produzidos em grande quantidade no MMC pelo tratamento térmico ao longo de sua matriz. Foi observado também que arredores das TiCp estavam majoritariamente ausentes de precipitados γ` primários, mas preenchidos com a sua precipitação secundária. Por FEG-MEV, foi possível analisar a precipitação da γ` secundária nos contornos de grão, o que ocorreu no MMC por toda sua extensão. Nenhum defeito microestrutural grave foi detectado na composição testada que pudesse descartar testes adicionais ou o processamento por DED-L. Deste modo, a avaliação mecânica de amostras deste material permanece para trabalhos futuros objetivando avaliar sua adequação em aplicações onde alto desempenho mecânico é exigido.

Palavras-chave: Compósitos de matriz metálica; Deposição por energia direcionada; Processamento de materiais a laser; Superligas a base de níquel; Reforço por particulado; Caracterização microestrutural.

ABSTRACT

Metal matrix composites, or MMCs, are usually classified as high-performance materials which are used in aerospace applications. Researchers have exploited the thermal stability of ceramic particle reinforcements to enhance creep resistance of alloys. Now, with the dissemination of additive processes based on laser technology, a new broad spectrum of MMCs and applications appears to be at reach. Here, the reinforcement of Inconel X750 with titanium carbide particulate (TiC_p) using Laser Directed Energy Deposition (DED-L) was researched, being the works' main goal to enable and analyse the fine-powdered deposition of this specific MMC composition, focusing in deposition behaviour, process stability and overall microstructural features. The attempts made to ease powder flow, such as a new powder feeder silo with steeper inner angle were ineffective, nonetheless, DED-L of the TiC_p-reinforced Inconel X750 MMC was made possible to a certain extent given the low powder flowability observed. Thereon, methods to analyse process stability, based in photogrammetry and in empirical quantities denominated stability factors, were proven effective in determining that a minimal input of energy per length of 70 $J.mm^{-1}$ is required for processing, while also indicating that for low flowability cohesive powders, lower powder feed rates, in the order of 2.5 g/min, were likely to increase process stability; being these conclusions true, under the conditions here tested. Despite the difficulties, enough consistency in deposition was achieved to allow evaluation of MMC microstructure and the relation between process parameters and deposition quantities. All relations met here followed what is described in the literature, showing that the MMC powder will behave as required by DED-L once the powder flow problem is solved. Scanning electron microscopy (SEM), Field Emission Gun-SEM (FEG-SEM), Transmission electron microscopy (TEM), optical microscopy (OM) and X-ray Diffractometry (XRD) were used to analyse MMC microstructure of single beads and overlapped depositions. Analysis of samples after and before aging heat treatment was essential to understand microstructure formation. The MoO_3-based metallographic etching made possible to analyse gamma prime's secondary precipitation through FEG-SEM. The XRD analysis done enabled characterization of the major MMC constituents and the aftermath of niobium's reaction with the added TiC_p, which likely formed NbC and (Nb,Ti)C. The degradation suffered by the TiC particles was minimal, as the matrix chemical composition remained nominally equivalent to Inconel X750's. The gamma prime precipitates are high occurrent in the heat-treated MMC`s matrix. Their size and distribution are characterized. $TiC_p$ were evenly distributed along the MMC, being present inside grains and at grain boundaries. The $TiC_p$'s surroundings were mostly absent of primary $\gamma$` precipitates but filled with γ`s secondary precipitation. The work evidences that a larger presence of dislocations may lie around these particles, which would be caused by the thermal coefficient misfit between matrix and reinforcement particulate. This high dislocation concentration is likely the cause for the high nucleation of the secondary γ` precipitates around TiC_p. No major defect or material degradation was detected which could discard further testing or processing this MMC composition by DED-L. The mechanical evaluation of this material stays for further works, promising good performance in traction creep when subjected to centrifugal forces.

Keywords: Metal Matrix Composites; Directed Energy Deposition; Laser materials processing; Ni-base Superalloys; Particle Reinforcement; Microstructural characterization.

RESUMO EXPANDIDO

Introdução

Compósitos de matriz metálica, ou MMCs, são geralmente classificados como materiais de alto desempenho que são utilizados em aplicações aeroespaciais. No desenvolvimento de tais materiais, pesquisadores exploram a estabilidade térmica de reforços cerâmicos para aumentar a resistência à fluência e outras propriedades mecânicas de ligas pré-existentes. Recentemente, com a disseminação de processos de manufatura aditiva baseados na tecnologia a laser (LAM), um novo e amplo espectro de MMCs parece estar ao alcance. Neste trabalho pesquisou-se a possibilidade de se reforçar a superliga de níquel Inconel X750 através da inserção de 15% vol de partículas de carboneto de titânio, abreviadas como TiCp, usando deposição por energia direcionada a laser (DED-L), um processo LAM. Os objetivos principais deste trabalho são viabilizar e analisar a deposição do pó de baixa processabilidade que foi utilizado como matéria-prima, e caracterizar microestruturalmente o material depositado.

Metodologia

Os pós de Inconel X750 e TiC foram misturados na proporção visada em um misturador “Y”. Tanto a mistura, quanto os pós puros foram caracterizados por microscopia eletrônica e quantificação de granulometria por interferometria a laser, enquanto a escoabilidade da mistura foi aferida através de funis de Hall e de Carney. Independentemente dos resultados obtidos na etapa anterior, foram feitas adaptações no alimentador de pó do sistema laser para viabilizar o processamento desta mistura de baixa escoabilidade por DED-L. Uma vez que um fluxo de pó considerado adequado foi estabelecido, este foi quantificado ao se mensurar a massa que fluiu ao longo de um período de tempo predeterminado. Os valores obtidos foram utilizados para uma averiguação inicial da estabilidade do processo. Em seguida, uma matriz de parâmetros de processo foi determinada através de conclusões tiradas da literatura, os parâmetros que foram testados são potência laser, velocidade de avanço e fluxo de alimentação de pó. A superfície de cada um dos 90 cordões depositados foi mensurada por fotogrametria ativa, da qual dados estatísticos referentes a estabilidade de cada conjunto de parâmetros foram retirados e comparados. A precisão da fotogrametria ativa em mensurar determinadas dimensões foi aferida por comparação com as mesmas grandezas mensuradas metalograficamente de seções transversais de cada cordão. Como os cordões foram seccionados para metalografia, metade de cada cordão foi tratada termicamente com intenção de reproduzir a microestrutura solicitada da liga Inconel X750 quando em aplicações que exigem resistência a fluência. Deste modo se obteve um espécime tratado termicamente e outro não de cada conjunto de parâmetros, o que permitiu comparação microestrutural entre as condições ao longo de toda faixa de parâmetros. Esta análise foi efetuada por MO, MEV, EDS-MEV e FEG-MEV. Simultaneamente, por análise da relação entre os parâmetros de processo e a dimensões dos cordões, e.g. largura e diluição, se avaliou o comportamento e estabilidade do processo e se estes encontravam-se de acordo com a literatura. Um conjunto de parâmetros foi escolhido para servir como base para a sobreposição de cordões e assim gerar uma deposição de maior volume que permitiria alcançar a composição almejada e a extração de corpos de prova para análise em MET e DRX. Por fim, com toda a informação relacionada às micro e nanoestruturas do material, conclusões foram tiradas sobre a viabilidade e a validade de fabricação deste MMC, bem como sobre o comportamento e a estabilidade deste processo.

Resultados e Discussão

Não foi possível caracterizar o fluxo da mistura nos funis Carney e Hall devido a baixíssima escoabilidade do pó. Deste modo, com o objetivo de facilitar o fluxo de pó, foi construído um novo silo alimentador com ângulo interno mais acentuado, mas este não resolveu o problema. A segunda e final tentativa foi a alimentação direta do pó à tubulação de alimentação do cabeçote de DED-L, o que permitiu o processamento dentro um pequeno intervalo de tempo, suficiente para que amostras de MMC fossem produzidas. Por sua vez, estas dificuldades permitiram a avaliação dos métodos utilizados para analisar a estabilidade do processo. Estes métodos foram baseados em fotogrametria e em grandezas então denominadas fatores de estabilidade, mostrando-se eficazes. Com tais ferramentas foi possível determinar que uma inserção de no mínimo 70 J.mm^{-1} é necessária para o processamento nas condições ensaiadas, além de indicar que taxas de alimentação de pó mais baixas são propensas a aumentar a estabilidade do processamento de pós de baixa escoabilidade por DED-L. No caso deste trabalho valores na ordem de 2,5 g/min s permitiriam um processamento mais estável. Apesar das dificuldades descritas anteriormente, estabilidade de deposição suficiente foi obtida para permitir DED-L, subsequente avaliação microestrutural e análise da relação entre os parâmetros de processo e as grandezas relacionadas aos cordões depositados. Todas as relações mensuradas seguem o descrito na literatura, mostrando que este particulado se comportará conforme exigido e permitirá DED-L por extensões grandes, uma vez que o fluxo de pó for garantido de forma contínua nas vazões necessárias. Porosidade e trincas não foram encontradas por microscopia ótica (MO) ou microscopia eletrônica de varredura (MEV) nos cordões depositados, nos quais foi observado crescimento de grão em orientação preferencial. Também não foram detectadas segregações ou aglomerações das TiCp em nenhuma condição de processamento apesar da diferença de densidade entre matriz e reforço. Análises de espectroscopia por energia dispersiva (EDS) realizadas em MEV de baixo vácuo e em MEV equipado com subsistema do tipo *Field Emission Gun* (FEG) identificaram que nióbio oriundo da matriz de Inconel X750 se concentrou ao redor de todas TiCp. A análise por difração de raios-X (DRX) realizada, que também permitiu a caracterização dos principais constituintes do MMC, indicou quais foram os prováveis compostos resultantes da reação do Nb, sendo eles NbC e (Nb,Ti)C. A formação destes carbonetos, na disposição descrita no trabalho, não foi considerada deletéria ao material. Complementarmente, a composição química da matriz também foi mensurada por EDS-MEV e comparada com a composição do pó de Inconel X750, demonstrando igualdade nominal entre as composições. Estes resultados evidenciam que a degradação sofrida pelas partículas de TiC foi mínima. A análise das amostras pré e pós tratamento térmico foi essencial para entender a formações das microestruturas analisadas e as transformações sofridas e causadas pelos carbonetos adicionados, contudo, um resultado se destaca. A precipitação de Nb foi identificada em ambas as condições, indicando que ela ocorre durante o processamento a laser. Análises por microscopia eletrônica de transmissão (MET) e FEG-MEV mostraram que os precipitados γ` foram produzidos em grande quantidade pelo tratamento térmico ao longo da matriz do MMC. Estas fases mostraram leve aglomeração em certos pontos, mas de maneira geral se distribuíram homogeneamente pela matriz. O tamanho médio dos precipitados $\gamma$` mensurado para o MMC foi menor do que o encontrado no substrato de Inconel X750 forjado à quente. Foi observado também que arredores das TiCp estavam majoritariamente ausentes de precipitados γ` primários, mas preenchidos com a sua precipitação secundária. Vários indícios descritos ao longo do trabalho indicam uma maior presença de discordâncias ao redor das partículas, fenômeno decorrente da diferença entre coeficientes térmicos da matriz e das TiCp. Esta alta concentração de discordâncias é provavelmente correlacionada com a alta nucleação de γ' secundária em torno das TiCp, uma vez que as discordâncias serviriam de nucleadores para as γ' secundária durante o tratamento térmico. Com o ataque metalográfico utilizado, foi possível analisar a precipitação da γ` secundária nos contornos de grão através de FEG-MEV, que ocorreu no MMC por toda a extensão dos contornos. Esta formação pode auxiliar no deslizamento dos contornos quando o material for submetido a esforços mecânicos, sendo sua análise de interesse para o desenvolvimento do material.

Considerações Finais

DED-L de Inconel X750 reforçado com TiC se mostrou promissor apesar das dificuldades em processar o pó de baixa escoabilidade. As ferramentas testadas e os métodos descritos no trabalho se mostraram eficazes em determinar quais condições de processamento DED-L são adequadas ou não, ficando como contribuição para trabalhos futuros junto com técnicas de caracterização microestrutural para o estudo de processamento DED-L de superligas de níquel. Nenhum defeito microestrutural grave foi detectado na composição testada que pudesse descartar testes adicionais ou o processamento por DED-L. Deste modo, a avaliação mecânica de amostras deste material permanece para trabalhos futuros objetivando avaliar sua adequação em aplicações onde alto desempenho sob fluência é exigido, por exemplo lâminas de turbinas. Se ressalta a fluência sob tração, uma vez que a densidade do MMC desenvolvido é menor que a de Inconel X750, podendo assim reduzir as forças centrifugas da lâmina além de reduzir o peso total da turbina.

Palavras-chave: Compósitos de matriz metálica; Deposição por energia direcionada; Processamento de materiais a laser; Superligas a base de níquel; Reforço por particulado; Caracterização microestrutural.

LIST OF FIGURES

LIST OF TABLES

LIST OF ACRONYMS AND ABBREVIATIONS

ABNT	Associação Brasileira de Normas Técnicas
AM	Additive Manufacturing
AMS	Aerospace Materials Specifications
ASTM	American Society for Testing and Materials
Cermat	Ceramic & Composite Materials Research Laboratories
DED	Directed Energy Deposition
DED-L	Laser Directed Energy Deposition
EDM	Electric Discharge Machining
EDS	Energy-dispersive X-ray spectroscopy
FCC	Face-Centred Cubic
FEG	Field Emission Gun
FGM	Functionally Graded Materials
LabConf	Laboratório de Conformação Mecânica
LabMat	Laboratório de Materiais
LAM	Laser additive Manufacturing
LCME	Laboratório Central de Microscopia Eletrônica
LENS^{TM}	Laser Engineered Net Shaping
LMP	Laboratório de Mecânica de Precisão
MMC	Metal Matrix Composite
MMC$_p$	Particle-reinforced Metal Matrix Composite
MPC	Metal Matrix Composite
RPM	Melt pool circumference
SAD	Selected Area Diffraction
SEM	Scanning Electron Microscope (or Microscopy)
TEM	Transmission Electron Microscope (or Microscopy)
TiC$_p$	Titanium Carbide Particulate (or Particles)
UFSC	Universidade Federal de Santa Catarina
XRD	X-ray diffractometry

LIST OF SYMBOLS

A_{dep}	Deposition area
A_m	Dilution area
d	Bead dilution
$\dot{D}$	Deposition rate
E	Input of energy per millimetre
F_H	Adhesive force between particle and surface
F_V	Force applied into bulk solid
F_Z	Bulk solid cohesive force measured
G	Thermal gradient
g	Gravitational acceleration
H	Initial curvature at the apex of the Young-Laplace plot
h	Bead height
h'	Bead melt pool depth
$\dot{m}$	Powder feed rate
o	Bead overlap
O_A	Deposition area stability factor
O_h	Height stability factor
P_L	Laser power
R	Particle radius
R_S	Solidification front velocity
s	Spacing between beads
S_A	Bead's deposition area standard deviation
S_h	Bead's height standard deviation
x	x-coordinate in a cartesian plan of reference
x_i	x-coordinate iteration for the Young-Laplace plot
z	z-coordinate in a cartesian plan of reference
z_i	z-coordinate iteration for the Young-Laplace plot
w	Bead width

Greek Letters

γ	Gamma phase
γ'	Gamma prime precipitate
γ_{lv}	Surface tension between liquid and vapor
η	Eta phase
η_{pd}	Powder efficiency
ρ_{liq}	Liquid’s density

ρ_t	Theoretical density of powder mixture
σ_t	Bulk solid cohesive tensile strength measured
θ	Tangential angle (or wetting angle)

CONTENTS

1 INTRODUCTION

Metal matrix composites, or MMCs, are usually classified as high-performance materials which are commonly used in aerospace applications [1]. These applications are sought to be expanded to components such as vanes, stators and blades. For such, researchers have exploited the thermal stability of ceramic particles to enhance creep resistance and other mechanical properties of alloys [2–6]. MMCs are defined as a combination between a metallic matrix and one or more ceramic reinforcements. When varying the proportion between these components, their nature or characteristics, or the MMC's manufacturing process, one is altering material performance while altering its microstructure [7].

Nowadays, with the dissemination of additive manufacturing processes based on laser technology, a new broad spectrum of MMCs and related applications appears to be at reach. Due to these processes, refined solidification conditions and component shape flexibility became feasible. Here, the reinforcement of Inconel X750 with the addition of 15%vol of titanium carbide particulate through laser additive manufacturing (LAM) was evaluated, in a continuation of the work of Lemos *et. al.* [8,9] from the Technische Hochschule Ingolstadt (THI). They processed this same composition by low energy mixing, uniaxial pressing and sintering. The idea behind adding such large amount of TiC particles is mainly the reduction of Inconel X750's density, without significantly decreasing this superalloy's creep resistance. The reason for targeting this is the intention of eventually applying this MMC composition to a specific application, the turbine blades. These components are subjected to high tensile-centrifugal forces, thus, in their case, less weight means less stresses and longer component lifespans. The work done by Lemos *et. al.* resulted in an MMC with greater compressive creep resistance and indeed smaller density. However, due to mechanical sintering's restricted material fusion, the metallic matrix was not sufficiently molten to avoid the added TiC particles to be constrained and agglomerate into grain boundaries. Such agglomeration is highly likely to be detrimental to creep resistance when tensile, and not compressive, forces are applied to the MMC, restricting this MMC application into turbine blades.

Their work led to the conclusion that in order to expand the number of applications for this composite composition, a process which dealt with powder and could melt the powder mixture's metallic volume, without generating other microstructural complications, is necessary; based in such, the Precision Engineering Laboratory (LMP) settled this master thesis topic while also started a partnership with the THI, thus allowing results and resource sharing for this and subsequent works. The manufacturing process chosen to be evaluated in this master thesis was the Directed Energy Deposition with laser (DED-L), which lies inside the LAM group and is being intensively researched at the LMP [10–14]. This master thesis is the first to include the research of MMCs manufactured by DED-L to the laboratory's repertoire.

After the expressed, it is proper to expose that this master thesis presents a degree of novelty, not due processing a composition not yet explored by LAM, but since few have attempted to process by DED-L a low-flowability powder mixture which includes a large amount of fine-powdered carbides (0.2 μm to 3.3 μm), and fewer or none have discussed the process viability and evaluated its stability due to adding a powder with these characteristics. Fine powders tend to have poor flowability, which is detrimental to processing in most DED-L systems. The current work aimed to test and provide methods that may be used to identify when a DED-L process has reached its feasible boundaries. A major part of this work is also the microstructural characterization of the MMC deposits. Through this, it aims to identify which reactions the TiC particles and the Inconel X750 may have suffered during laser processing. Characterization was performed both in heat treated and non-treated samples, which is also an aspect not often found in the literature since most researches that study the production of superalloy-MMCs by LAM aim for coatings, therefore, with wear or corrosion resistance in focus rather than creep resistance. Challenges were expected, as carbide dissolution due to excessive laser heating could occur, and that the DED-L system available could not be suitable to process the low flowability powder and would require adequation.

1.1 Objectives

This master thesis' main objective was to enable and analyse the fine-powdered laser additive manufacturing of TiC-reinforced Inconel X750 metal matrix composite, focusing in deposition behaviour, process stability and overall microstructural features.

1.1.1 Specific Objectives

With this main objective in mind, the following specific objectives are listed below:

a) Evaluate the means to attain DED-L process stability and itself, while using the process to obtain the MMC described;
b) Develop DED-L system modifications and powder feeding procedure, both necessary to allow processing of fine-powdered feedstock;
c) Determine criteria for definition of DED-L parameters, and evaluate the criteria chosen;

d) Analyse the correlation between main process parameters and deposition behaviour;
e) Characterize the microstructure of laser deposited MMC and the hot-rolled Inconel X750 substrate at the micro- and nanoscale, thus allowing evaluation of the effect that the addition of TiC particles and the DED-L processing exerted in microstructure;
f) Analyse the effects of AMS 5668 heat treatment in the microstructure of the DED-L manufactured MMC.

2 LITERATURE REVIEW

The literature review is divided in three main topics: laser directed energy deposition (DED-L), particulate metal matrix composites and a combination of both, ceramic particulate reinforced MMCs obtained through laser additive manufacturing; ending the review close to this work's topic. In some circumstances, articles that used other laser processes were referred here when adequate, due to the similarity that DED-L has to such process. This is mostly frequent in the topics 2.1.1, 2.2.2 and 2.3, as melt pool solidification phenomenology is comparable within these processes, and since correspondences in the metallurgy of ceramic reinforced MCCs manufactured through different processes can be found, especially when their feedstock's chemical compositions are similar.

2.1 Laser Directed Energy Deposition

Directed Energy Deposition (DED) is a class of additive manufacturing processes applied in surface coating and for the repair or manufacturing of components. Their operation principle is described as a continuous material feed into a melt pool formed by a concentrated energy source. When this intersection point is set in motion a bead may be obtained, and from it, a part, a repair or a coating may be built. Generally, this deposition occurs under the presence of an inert shielding gas [15,16].

According to recently established standards, ASTM 52900:2015 and ASTM F3187-16 [17,18], many systems configurations and processes, are classified as DED. When considering just the processes which deal with metals in their molten state, classification is made over, but not limited to, the feedstock material form and the type of energy source applied, as shown in Figure 1 and expressed in the standards.

Figure 1 – Classification of Directed Energy Deposition Processes

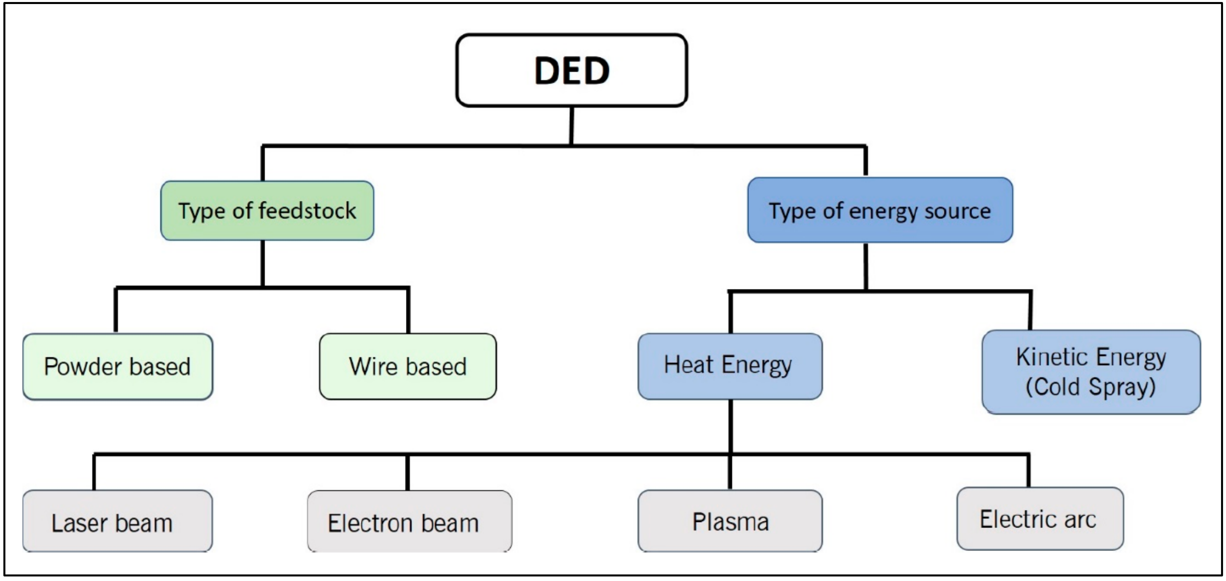

Source: [16]

From the subclasses defined by type of energy source, the laser based one is the most explored recently and the one researched in this work. Here it will be referred to as DED-L, the small "l" standing for laser. However, despite standardization, DED-L is still referred to by many other names, such as laser engineered net shaping (LENS™), laser metal deposition, blown powder additive manufacturing, and directed laser deposition. Thus, articles and other references with different nomenclatures to this process can be seen in this work's bibliography.

DED-L may have powder or wire feedstocks, and albeit wire fed DED-L processes usually allow greater depositions rates, the powder-fed processes are more researched by material scientists and engineers [16,19]. The preference for powder in this field is explained by the ease in which new material compositions can be attained and the great available spectrum of feedstock materials. When mixing two or more powders, a large number of final alloys compositions and microstructures can be achieved.

Feedstock mixture may occur before or during laser processing, revealing that an interesting resource of DED-L is the possibility of building functionally graded materials (FGM). Many works have built FGM with similar compositions than the metal matrix composite built here, with interesting results that will be partially described in section 2.3. Schematics of DED-L processes using each wire and powder feedstocks are depicted at Figure 2, other system configurations than the ones described are possible, *i.e.* with feedstock being fed from different directions and/or form multiple points, as summarized by Gutjahr in his master thesis [14].

Figure 2 – Wire (a) and powder (b) schematics of DED-L

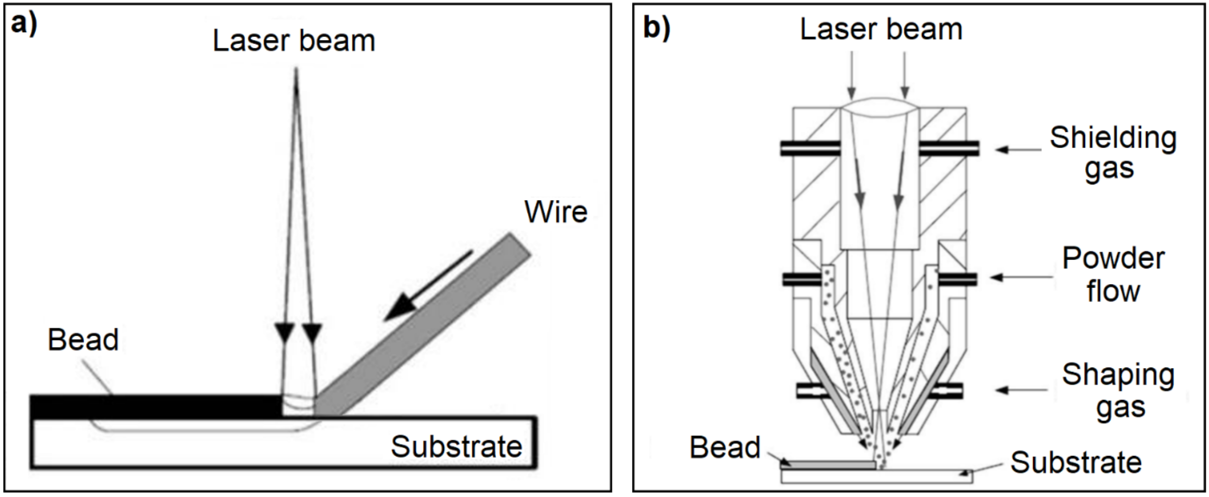

Source: Adapted from [15]

DED-L operation principle implies in a considerable number of variables which control the process outcomes; thus, careful parametrization is crucial to achieve functional results. The laser beam itself, focused or not, adds several variables to the system, such as beam spot size (focal distance), energy distribution etc [20]. DED-L related quantities and parameters usually found in the literature are depicted in Figure 3.

Figure 3 – Overlapped beads' cross section exposing main process parameters.

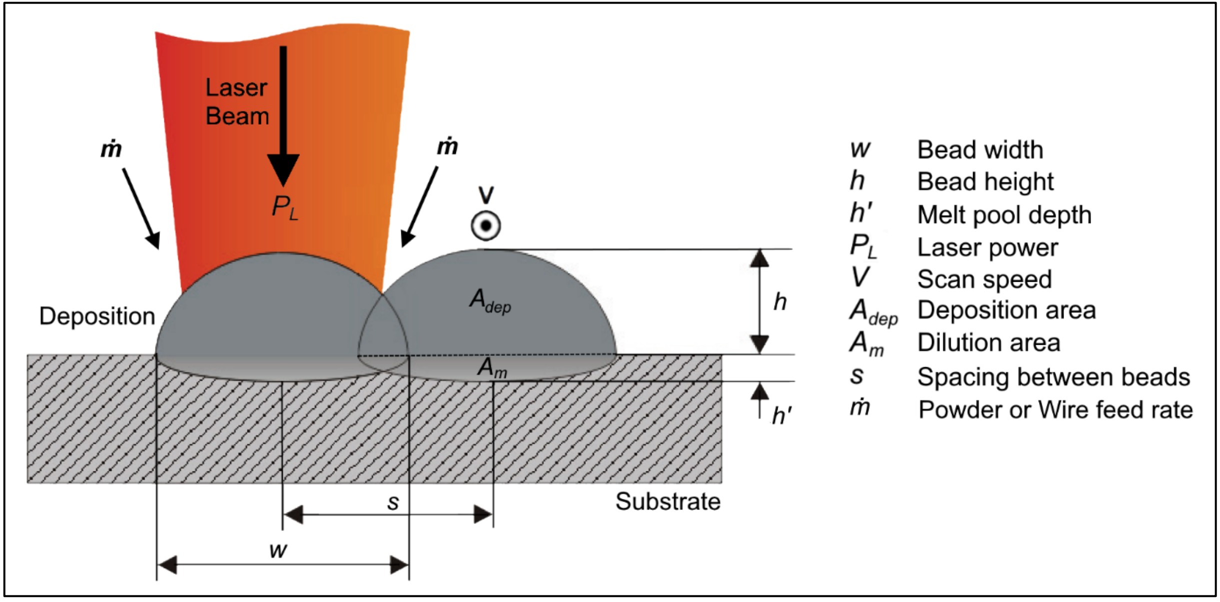

Source: Adapted from [21]

An addendum to the list from Figure 3 would be the dependent quantities of bead overlap (o), bead dilution (d), energy input per millimetre (E), and deposition rate ($\dot{D}$). The equations for calculating these quantities are found in the literature [21,22] and are of easy deduction, being expressed in Equations (1) to (4).

$$o[\%] = \frac{(w - s)}{w} * 100 \tag{1}$$

$$d[\%] = \frac{A_{dep}}{(A_{dep} + A_m)} * 100 \tag{2}$$

$$E = \frac{P_L}{V} \tag{3}$$

$$\dot{D} = A_{dep} * V \tag{4}$$

These are only some of the possible combinations between process parameters and other quantities, chosen to be cited since they are used in this work; some have more than one way to be calculated or measured. The absorptivity of the laser radiation by the irradiated materials, and the process' powder efficiency, which depends on powder catchment, will be addressed further in this text as to keep concept and result close together.

Regardless of definitions, the procedure of taking DED-L process variables and bead quantities and relate them to final component properties is complex, thus works in the fields of computer modelling [23], machine learning [24], process monitoring [25] and material science [16,26], the last being considerably present in this thesis, are trends in both academy and industry. Materials science's part is to supply conclusions over which material compositions promise useful microstructures, what occurs during melt pool solidification, and how these materials behave under stress.

These topics, including better description of referenced works will be addressed in further sections, but first it is necessary to describe the basic theory behind microstructure formation during melt pool solidification and to provide a review over powder feeders and powder flowability, since the DED variant used in this work was powder-fed DED-L.

2.1.1 Melt Pool Solidification

DED-L and similar laser additive manufacturing processes have been intensely researched regarding the understanding of solidification conditions of the molten pool and how it will be possible to take advantage of them, resulting in breakthroughs, such as DED-made single crystal growth [23,27,28]. This and other achievements would not be possible without the understanding of solidification modes and phenomena that coexist in a melt pool.

The phase-transformation heat transfers and its momentum at the solid/liquid interface are perhaps the most technically sophisticated phenomenology inherent to powder-based DED. The blown powder mass addition contributes to melt pool instability and transient morphology, while density-based and Marangoni convection also impact the heat transfer during solidification. This complex phenomenology is further coupled with the temperature-dependent microstructure evolution that depends strongly on material type. Solidification for carbon steels is different than that of Ti-6Al-4V and this is due to the various chemical elements in the alloys. Microstructural evolution describes the nucleation and growth of grains, through the solidification modes that can either be columnar, planar, dendritic or equiaxed dendritic. [25]. However, some relationships and concepts available can, in simple terms, grant insight over the microstructural evolution and, therefore, allow preliminary analysis of the microstructure evolution and formation in DED-L beads.

A melt-pool's solidification mode, or the morphology of the solidification structure, is approximated by the ratio between two quantities, the thermal gradient, *G* (*K/mm*), and the solidification front velocity, R_S (*mm/s*). A similar statement can be made over the multiplication of these two quantities, as this control the size of the solidification structures. Figure 4 outlines the influence of G/R_S and $G.R_S$ in a solidifying material.

Figure 4 – Influence of G/R_S in the solidification mode.

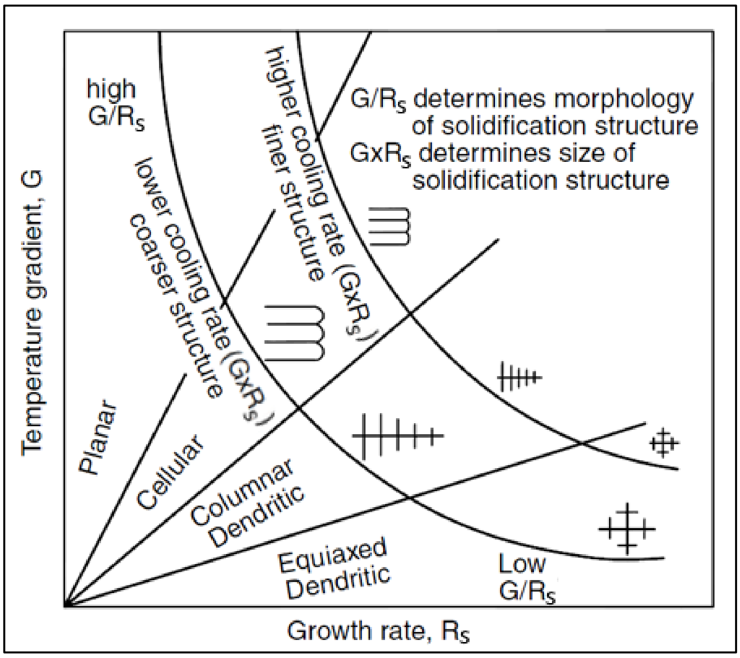

Source: Adapted from [22]

Applicable to solidification in other process, the information described in Figure 4 presents the usual order in which the four solidification modes are found, together with the direction to where finer structures can be achieved. However, the influence of G/R_S in DED-L must be complemented by considering the Melt Pool Circumference (MPC) length, which is measured from the bottom to the top-front point of the melt pool, Figure 5. This dimension is also an important factor in the prediction of solidification outcomes, since it works as an approximation to the volume from where new grains may form, and to the thermal gradient's spatial orientation [16,23,29]. The following process maps at Figure 5 describe how the MPC and some DED-L parameters exert influence in nucleation during solidification.

Figure 5 – Process maps for DED-L relating nucleation and G/R_S to process parameters.

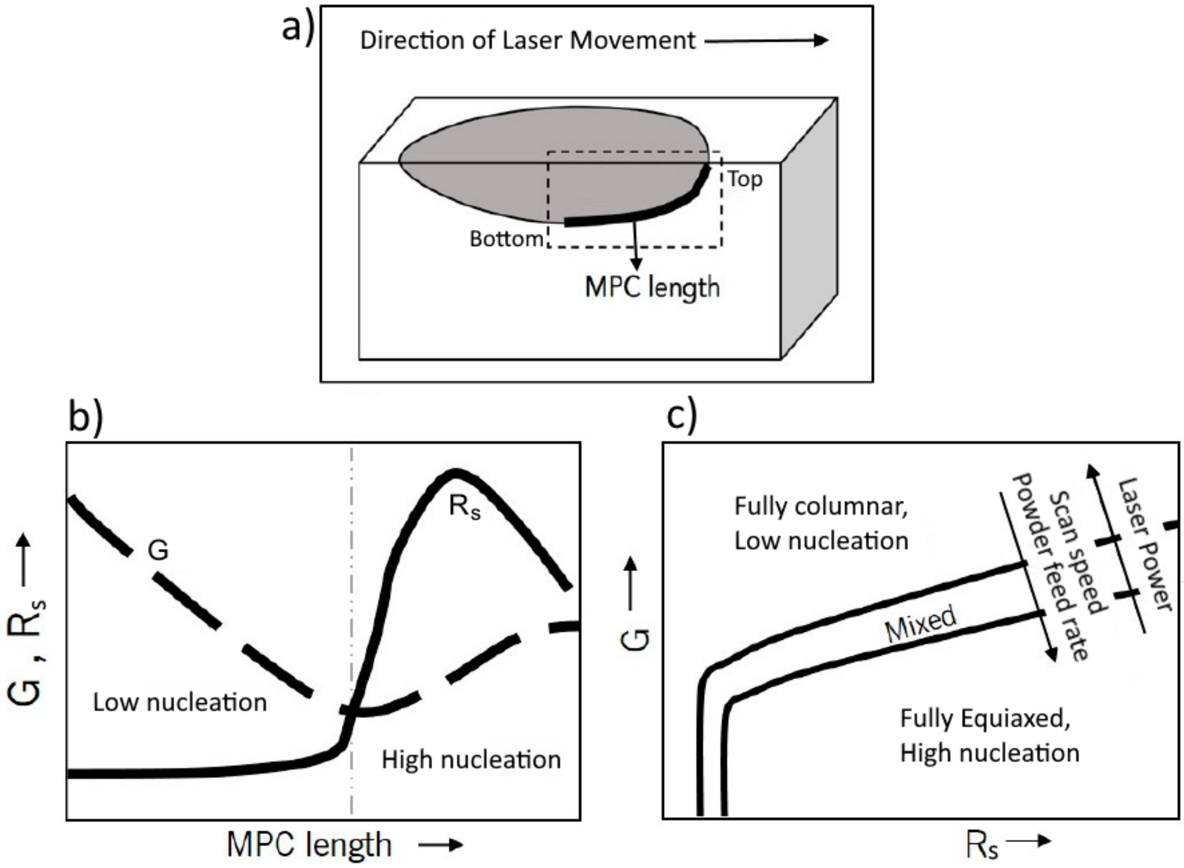

Source: Adapted from [16]

According to Figure 5, nucleation decreases with increase in laser power and increases with decreases in scan speed or powder feed rate. However, as much as the information regarding the influence of process parameters in nucleation due to *G* and R_S are relevant [16], the fact that un-melted powder particles will behave as nucleation sites within the solidifying melt pool must be also considered [25]; and having the three DED-L parameters just cited different effects in powder fusion and catchment [30], two concurrent phenomenology with regard to nucleation are met. The effect which will reign, will depend on the materials being processed and the ranges of processing conditions in which the particles captured by the melt pool melt, if they do it at all. This is exposed here, since DED-L made MMCs usually contain ceramic particles, powders naturally resistant to fusion.

Aside of such, DED-L beads may present grain growth in a preferential orientation, as growth direction is dependent of *G* [31], and *G* is likely aligned with the laser beam, which is inserting heat into the melt pool. This explains the reason why DED-L can present anisotropy, a characteristic which may or may not be beneficial to the final application [32]. This alignment between G and the laser beam may even cause epitaxial growth in some conditions, being intensified when substrate seeding occurs, as crystals will nucleate without the need to overcome any energy barrier caused by misalignment between *G* and the crystalline structure of the substrate [33].

2.1.2 Powder Flowability

Bulk solids are an assembly of solid particles in a number large enough for the statistical mean of any of its properties to be independent of the number of particles [34]. Considering the powder amounts used in DED-L processes, the concept of bulk solid is applicable to all cases.

The flow properties of a fine-grained bulk solid are mainly influenced by adhesive forces (F_H) between its particles due to liquid bridges (if moisture is present) and van der Waals forces (dominating force for dry, fine-grained bulk solids) [34]. Therefore, drying powders before DED-L is desired and often done to reduce the sum of adhesive forces, thus increasing flowability [15]. Both liquid bridge and van der Waals forces are proportional and increase with particle size, *x*, as shown in Figure 6.

Figure 6 – Influence of particle size on the force between a spherical particle and a wall

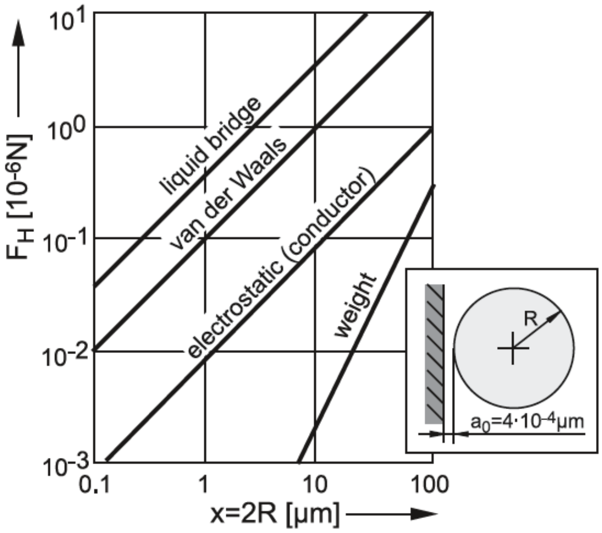

Source: [34]

However, the general experience with bulk solids is that flowability increases with increasing particle size, even if according to Figure 6 one would expect a higher flowability with smaller particles [15,34]. The reason for this is found in considering the spatial interaction that particle size exerts over an area, to outline this, the influence of particle size on the tensile strength of a bulk solid is examined in the following.

For idealized measurement of tensile strength, suppose a plate of area A coated with a thin layer of glue on its underside vertically pressed into a powder sample with a force, F_V (Figure 7). In sequence, the plate is slowly pulled straight until a part of the bulk solid detaches from the rest. A tensile strength, σ_t, is then determined with A and the portion of the force related to the strength of the bulk solid (F_Z), following Equation (5) [34].

Figure 7 – Hypothetical measurement of the tensile strength joining a layer of particles

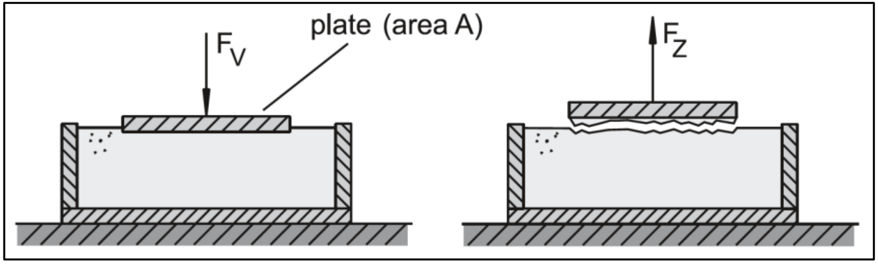

Source: [34]

$$\sigma_t = \frac{F_Z}{A} \tag{5}$$

Now, if F_Z is regarded as the sum of the adhesive forces of several particle contacts and being a particle`s adhesive force proportional to its diameter ($2R$), as described in Figure 7, the following Equations (6) and (7) may be delineated, respectively.

$$F_Z = n * F_H \tag{6}$$

$$F_H \propto (2R) \tag{7}$$

The number of particles (n) is also proportional to A and inversely proportional to the square of the particle diameter, leading to Equation (8).

$$n \propto \frac{A}{(2R)^2} \tag{8}$$

By joining Equations (5) to (8), it is demonstrated that σ_t, the tensile strength to separate the particles of a bulk solid is inversely proportional to the diameter of the particles that compose the volume, as described at Equation (9) [34].

$$\sigma_t = \frac{F_Z}{A} \propto \frac{n * F_H}{n * (2R)^2} \propto \frac{(2R)}{(2R)^2} \propto \frac{1}{(2R)} \tag{9}$$

This relation leads to the conclusion that if the gaps between a homogeneous set of particles are filled with smaller particles, one increases even further the adhesion that this new bulk solid would have, when compared it to the previous. Thus, good powder flowability can be difficult to achieve in a real-world particle distribution, were particles sizes normally range within two values in Gaussian-like distributions and were two or more particle distributions may be found in mixture.

Particle shape and other factors also significantly influence the flowability of bulk solids, however, general statements over such influence cannot be made, as flow properties vary significantly from one type of particles to another. Nonetheless, flowability test procedures can always be made to characterize their properties [34]. That said, most powders provided for DED-L are metallic and present near-spherical shape to ease powder flow [35–39]. However, in the production of MMCs by DED-L, the powders used are not exclusively metallic; ceramic powders are processed together to a powdered alloy being included into the melt pool or melted into it. Ceramic particle reinforcements are widely available, usually found in their crushed form and thus presenting jagged shapes [37]. These shapes may severely impair flowability, depending on powder combinations and preparation [34].

2.1.3 Powder Feeders

Many powder feeder configurations are used to provide the flow of powder required by DED-L systems. The feeders may be categorized in groups depending on the operation principle they apply; being gravity-based, mechanical screw, fluidized bed, and vibratory, the most usual categories [15].

Only gravity-based and fluidized bed are better detailed here, since traditional mechanical screw and vibratory powder feeders are likely to present problems in working with most powders used in MMC manufacturing. These problems are, the interaction of moving parts with abrasive powder particles, which cause rapid wear when regarding mechanical screws; and vibration-induced powder segregation, which depends on powder characteristics and the oscillation parameters used in vibratory feeders.

Gravity based powder feeders are the most common type of feeders applied in DED-L. They operate based on the fall of powder from a silo, or powder chamber, through a relatively small orifice into a metering system, be this a disc, a wheel or a weighing mechanism controlling the orifice aperture. Usually when more precise flow is required from such systems, one of the two later metering mechanisms are preferentially applied, and a back pressure is forced into the silo to help increasing flow stability. Systems with these features are schematized in Figure 8.

Figure 8 – Schematics of gravity-based powder feeders

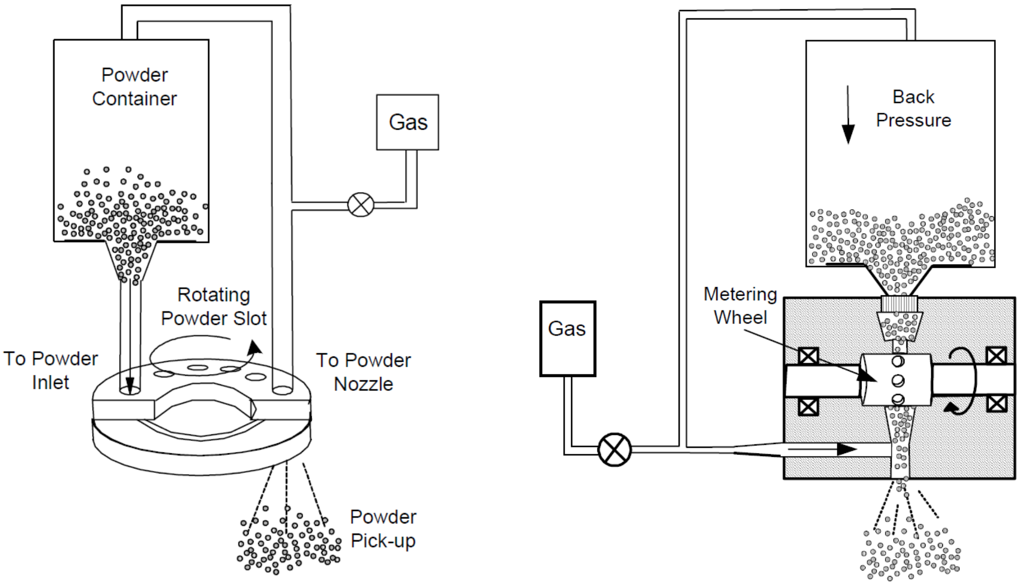

Source: Adapted from [15]

Since fluidized-bed feeders are based in fluidics, they discard the control of powder flow by mechanical parts. They do so by converting the fed bulk solid in a fluid through insertion of a gas flow to separate and carry its particles, as depicted in Figure 9.

Figure 9 – Schematic of fluidized-bed powder feeder

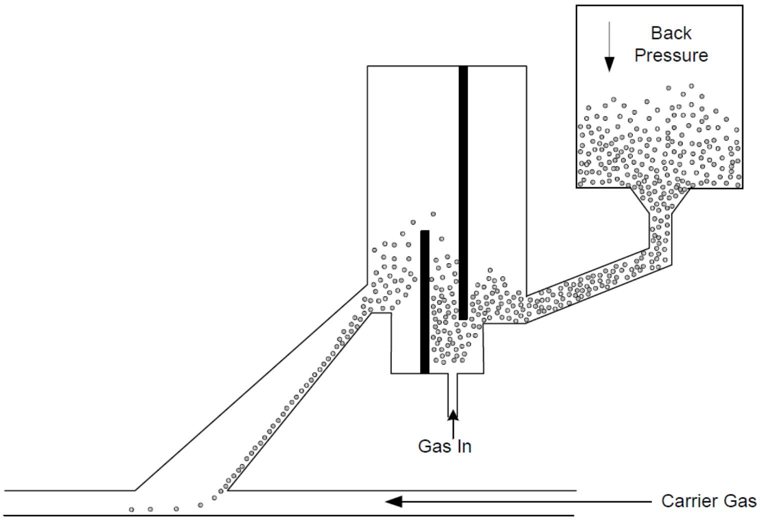

Source: Adapted from [15]

This operation principle also may lead to particle segregation, since light particles are more susceptible to lift than heavier ones, however, this can be mitigated, as done by Alves *et al*. [40]. Their work joined characteristics of both gravity-based and fluidized-bed feeders, by adding a metering wheel before the fluidization chamber, thus restricting the possible amount of segregation as only a small amount of powder is fluidize at a time, while also stabilizing feed oscillations caused by the metering wheel.

Powder feeders are a well-developed technology which has not stagnated. Current efforts have been aiming precise dosing and feed of low flowability powders, such as finely powdered ones, through development of novel and hybrid types of powder feeders, as well as new control systems. These efforts have been partially driven by the proliferation of powder based additive manufacturing processes.

Peng *et al*. [41] designed a gravity-based feeder with an grooved stirrer which, more than forcing the powder through the aperture, also controls feed by varying silo aperture size. In this manner, fine powders were fed. Their work also included the development of a novel control system based in gravimetric principles, while also evaluated the influence of stirrer rotational speed and orifice aperture in powder feed rate.

Suri *et al*. [42] developed a novel cartridge type powder which applies a principle of “subliminal fluidization”. They define the principle as volume-restricted aeration of the powder near the cartridge’s exit, also known as the silo’s exit. Fluidizing gas and carrier gas come from the same channel, thus exiting particles are replaced inside the cartridge by gas. Their paper also lists and describes several other powder feeder designs published from 1959 to 1996.

Kumar *et al*. [43] described the behaviour of small exit hoppers of different profiles applicable to gravity-based feeders. The work also suggested changes in a mathematical correlation which describes powder flow rates in gravity-based feeders, presented possible automatic valving of some hopper designs through vibration, and proposed the use of these findings in simultaneous laser additive manufacturing of different materials.

Another aspect of powder feeders still needs to be presented. There are several designs of silos for storing bulk solids, being the most usual design a cylindrically shaped tube with a conical hopper as exit. The maximal inclination of this hopper walls to the vertical axis of the cylinder is defined by a subtraction of the angle of wall friction from the 65° angle value, as state by Schulze [34]; Being, the angle of wall friction defined as the slope of a line running from the origin of an experimental normal and shear stresses diagram to a point where a steady-state sliding was achieve between the bulk solid and the “silo’s” wall. And since the higher the angle of wall friction, more stress is necessary for a powder to flow, it is possible to conclude that the more vertical the walls of a silo are, the easier is to a bulk solid to flow from it.

2.2 Particulate Metal Matrix Composites

Composite materials attempt to enhance the properties of monolithic materials through the addition of a reinforcement phase into a matrix, this reinforcement phase can be ceramic or not. As the name describes, metal matrix composites (MMC) have a metallic matrix which is usually made of iron, aluminium, titanium, nickel or cobalt alloy. The definition of MMC has two takes in the literature, the broad definition includes every material with a pronounced dispersoid phase, such as oxide dispersion strengthened alloys, perlitic steels and others; and the more conservative view considers as MMC only those materials whose reinforcement phase remains distinguishable along the material`s complete manufacturing process [1,7,44,45].

These materials can be manufactured through several processes, such as casting, sintering or additive manufacturing. Whereon, their reinforcement phase can be added in several shapes, such as fibres, whiskers or particulates [46]. Particulate reinforced metal matrix composites (MMC_p) come to interest due to their cost-effectiveness, isotropic properties and thermal stability. Their processing versatility also is an important factor, as they can be processed with technologies similar to the ones used for monolithic materials [6,47] and with most DED processes. In MMC development, the improvement of tribological, thermal and, mechanical properties is pursued, were reinforcement and matrix characteristics and compatibility must be taken in account as they directly affect material performance [8,37].

Chemical compatibility is necessary so that the reinforcement maintains its properties by not reacting with the matrix during application or secondary processing, thus maintaining desired properties. This requirement is sometimes not fully met despite design efforts, limiting the component's useful timespan, especially in cases were the application exposes the material to high temperatures. Thermal compatibility is also relevant, uneven thermal expansion may lead to stress concentration after manufacturing or during application at high temperatures. All considered, severe stress concentration due to thermal mismatch may or not be a problem in MMC_p depending on factors as volume fraction and particles size. MMC_p also do not concentrate as much stress as, for example, whiskers reinforced MMCs; since particles are closer to isometric solids [1,6,46]. The effect of particle size in MMC strengthening will be readdressed further on. Differences in density also may lead to anisotropy due to segregation during liquid metal processing, this may be solved by stirring and controlled solidification [1,45].

The classical strengthening mechanism present in composites, and extended to MMC_p, is described as load transference from a weaker matrix to the stiffer reinforcement, such causes the reinforcement to support much of an applied load. However, since reinforcement particles are near-isometric, load transfer is not as efficient as in other types of MMC, diminishing the intensity of this effect.

Due to thermal mismatch between matrix and reinforcement, MMC_ps may generate dislocations in the interfaces between matrix and reinforcement to accommodate stress. This thermally induced dislocation punching, which occurs during cooling from manufacturing, is also a strengthening mechanism, since it provides localized plasticity and annihilation or anchoring of deformation-derived dislocations [6,48,49]. Another relevant phenomenon caused by these dislocation agglomerations is found in age-hardened alloys, such as superalloys. During quenching or similar heat treatment, the dislocations serve as heterogeneous nucleation sites for precipitate formation, turning the interface around reinforcement particles into regions of preferential precipitation. The region, thus, is strengthened while time for peak-aging may also be decreased. As final remark to this stays that an increase in reinforcement volume fraction or a decrease in particle size, increases the amount of interfacial area and, therefore, enhances related strengthening mechanisms [6,44].

Introducing particles which are resistant to the heat of liquid manufacturing processes, causes the final material to have a smaller grain size when compared to their non-reinforced counterpart. This happens since any solid particles in a solidifying melt pool serves as a crystal nucleation sites or grain boundary constrainers. Thus, most MMC_ps possess finer grain sizes than their raw metal matrix. Another strengthening mechanism derives from such, the Hall-Petch relation, which determines that dislocation pile-up at grain boundaries is larger in coarse-grained materials, by assuming that grain boundaries are insurmountable obstacles to dislocations. The larger the pile-up, the larger the stress concentration and more prone is a material to yield to a given strain. In order words, stress is more evenly distributed in fine-grained materials, since dislocation pile ups are necessary smaller [6,44,50,51].

2.2.1 Nickel-base superalloys

Superalloys are complex material systems which combine resistance to creep, environmental degradation and fatigue above limits accessible to martensitic steels, i.e. 540°C, sometimes maintaining these qualities at temperatures near their melting point. Historically they were developed to replace materials in applications related to gas turbines, being nowadays usually classified by generation or by the prominent chemical elements in them. The later form of classification makes a list consisting primarily of cobalt-based, iron-based, iron-nickel-based and nickel-based superalloys [52–54]. Further remarks done here will refer only to nickel based-super alloys, since a material from this group is one of this work's foci.

Classification by generation refers to breakthroughs involving concept changes and processing optimization. Examples of such steps forward are the suppression of grain boundaries by directional solidification, which resulted in highly thermally stable single crystalline superalloys, or the increases in gamma prime phase percentage with gains in mechanical properties. These are properties that, together with cost-effectiveness, make Ni-base superalloys to stand out from other concurrent alloys and materials [52–54].

As by design, Ni-base superalloys are widely applied in gas turbines, receiving attention recently since they are excellent candidates to serve as MMCs matrixes. Carbides and borides are common to polycrystalline superalloys where they are mostly used to strengthen grain boundaries, avoiding slip and reducing diffusion. Adding further reinforcement particles is seen as promising when aiming to improve mechanical properties, i.e. mechanical wear, hardness and creep resistance [4,44,55–57]. However, to understand the effects of adding reinforcement particles in Ni-base superalloys it is necessary to first know their microstructure to have a base of comparison. An introduction is given in the following, focusing in polycrystalline Ni-base superalloys.

2.2.1.1 Microstructure Overview

Four microconstituents are described in the following, the two first are present in most Ni-base superalloys [52–54]:

- the gamma phase, γ, is in most cases continuous along the alloy [58]. It has face centred cubic (FCC) structure and is mainly constituted of nickel. Chromium is its primary alloying element, replacing nickel as solid solution in around a quarter of the atomic sites. Mo, W, Ta, Nb, Re and Co may also exert similar role. Since all these elements have different atomic radii, they deform the crystalline lattice, stiffening the material while increasing the energy necessary for dislocations to move;
- the gamma prime phase, γ', forms often-coherent FCC precipitates which are the principal strengthening phase of several superalloys. It is usually composed of Ni_3Al, with other possible compositions, i.e. $Ni_3(Al, Ti)$. This ordered phase assumes the shape of spheres, cubes, arrays of cubes and

eventually solid-state dendrites depending on ageing and composition. Dispersed throughout the matrix, they serve as considerable barrier to dislocations as their lattice misfit with the matrix exerts force against the movement of dislocations [59];

- Carbides may assume the following chemical formulae MC (cubic), M_6C (FCC), $M_{23}C_6$ (FCC), and M_7C_3 (hexagonal), with "M" standing for one or more types of metal atoms, usually Cr, Ti, Nb, Fe, W, Mo or Hf. They precipitate in diverse forms such as films, globules, blocks, platelets, lamellae, and cells, and are present in almost every polycrystalline superalloy. Elongated shapes are avoided when aiming for creep resistance since they are prone to cracking. When lodged in grain boundaries most carbides reduce grain-boundary sliding, being this the role to which they are more often designed for. However, in cast and wrought alloys they may also be included in grains to increase strength by dispersion hardening, being it secondary to γ' precipitation hardening but still significant. Carbide density varies significantly with chemical composition;
- the eta phase, η, is of hexagonal compact habit, composed of Ni3Ti and found in extensively aged superalloys with high titanium/aluminium ratios. It may form in cellular shapes between grains or intraganurlarly as acicular platelets following a Widmanstätten pattern. The latter form is usually detrimental to mechanical properties.

Around the 60's, Ni-base superalloys designed for turbine applications received a larger increase in the volume fraction of γ' in relation to γ as it was proven to considerably increase mechanical properties. Earlier versions optimized the shape of gamma prime precipitates to cuboidal shapes [54]. Recently, the effect of laser additive manufacturing in the microstructure of Ni-base superalloys has been researched by many authors.

Lopez-Galilea *et al.* [38] indicated that heat treatments from cast or wrought superalloys must be adjusted when applied to equivalent laser additively manufactured (LAM) materials. The finer microstructure achieved by production of the CMSX-4 single crystalline superalloy through selective laser melting (SLM), a powder-bed process, requires shorter holding times for dissolution of primary precipitates. Shorter two-step aging treatments would also be recommendable, as microstructure stabilized in shorter period, developing a very fine γ/γ' microstructure with a unimodal γ'-precipitate size distribution. The plateau temperature of the aging treatment`s first step, should also be adjusted to avoid formation of unwanted phases.

With the same material as the previous, Bürger *et al.* [60] also recommended adjustments in heat treatment, but to an smaller extent, adding considerations about the microstructure formed and describing the equivalent-to-better creep resistance of the additively manufactured (AM) counterpart. Previous to heat treatment, the dendrite arm spacing of the AM manufactured material was smaller, evidencing the reason why microstructure homogenization is easier in comparison to cast materials. Their preliminary transmission electron microscopy (TEM) results indicated that the deformation mechanisms which rule creep rate are equivalent to ones of cast alloys, being directly influenced by parameters related to γ/γ'-microstructure. The effect of the refined microstructure on deformation rates in the early stages of creep is small but positive.

Luo *et al.* [61] analysed the effect of different heat treatments in the corrosion resistance of LAM-made Inconel 718, a polycrystalline Ni-base superalloy. Solubilization heat treatments at higher temperatures favoured corrosion resistance while also solubilized some undesirable phases and increased grain size due to coalescence.

Cao *et al.* [62] investigated the formation and microstructure of γ and γ' through high resolution TEM and other technics, in SLM- made Inconel 718 samples. Reporting the formation of 10 to 50 nm γ' precipitates within a cellular γ matrix.

All these works indicate that LAM-made materials, be it through DED-L or other, are promising but must have their complete production chain optimized, from powder manufacturing to heat treatment, to allow a next step in Ni-base superalloys technology to be taken.

2.2.1.2 Inconel X-750

Inconel X-750 is a precipitation-hardenable nickel-based superalloy used for its corrosion resistance and high strength at temperatures up to 700°C. Depending on the properties desired, different heat treatments can be employed to alter its properties. For rotor blade applications, where centrifugal loads and temperatures above 600°C are imposed, optimum properties are achieved by a triple stage heat treatment, as described in the standard AMS 5668. This treatment in designed to induce considerable precipitation hardening, which reinforces the material until temperatures equal to 700°C. Nonetheless, such heat-treated material has useful strength up to 980°C [63]. Composition is shown in Table 1.

Table 1 – Inconel X-750 Limiting Chemical Composition (wt%)

Ni	Cr	Fe	Ti	Al	Nb	Mg	Si	S	Cu	C	Co
≥70.0	14.0-17.0	5.0-9.0	2.25-2.75	0.40-1.00	0.70-1.20	≤1.00	≤0.5	≤0.01	≤0.50	≤0.08	≤1.00

Source: [53,63]

Other applications of Inconel X-750 are rocket-engine thrust chambers, thrust reversers, hot-air ducting systems, heat-treating fixtures, forming tools, extrusion dies, and test machine grips [54,63]. All these applications may be benefited by enhancement of this alloy through ceramic particulate reinforcement. This superalloys has the density of 8.28 g.cm^{-3}, melting point inside the range between 1393 °C and 1427 °C, coefficient of linear thermal expansion around $12.6 \cdot 10^{-6}$ K^{-1} and elastic modulus of 207 GPa [64].

2.2.2 Titanium Carbide – as reinforcement particle

Titanium carbide (TiC) may be produced by a solid-state reaction between carbon and titanium dioxide (TiO_2) at low pressures, or by another solid-state reaction which includes titanium hydride (TiH_2) instead of the oxide [45]. TiC has the theoretical density of 4.94 g.cm^{-3}, melting point ranging between 2940°C and 3160 °C, coefficient of linear thermal expansion around $7.6 \cdot 10^{-6}$ K^{-1} and elastic modulus inside the range of 310 GPa to 462 GPa [64]. Radiation absorbance of its powdered form was measured for the wavelength of 1060 nm by Tolochko *et al.* [65]. In their work, TiC powder presented 82% of absorption, a higher amount than that of a nickel alloy similar to Inconel X750, which absorbed only 72% of the incident radiation. Carbides usually show better absorbances to this wavelength than oxides, the absorbance of Al_2O_3 to this wavelength is 3%, for example.

Recently, titanium carbide has been widely researched in its application as a reinforcement particulate for MMCs manufactured by additive methods, frequently having Ni-base superalloys as matrix. Particle sizes added in these researches are divided between the nanoscopic and the microscopic scale. The works referenced in the following had particle sizes distributed inside the ranges of 40 nm to 150 nm or 1 µm to 40 µm. Although through different reinforcement mechanisms for each particle range, researches look for understanding, measurement or improvement of the same characteristics, being them listed as tensile strength, wear resistance, machinability and corrosion resistance [2–5,56,66–69]. Each of the cited works in this paragraph used as matrix one of the following nickel-based superalloys, Inconel 625 or Inconel 718; but none studied Inconel X750.

Cooper *et al.* [37] compared the addition of equivalent amounts of three ceramic reinforcements, including TiC, to Inconel 625 by an SLM-like process, where a 4 kW

Ytterbium fibre laser with nominal wavelength of 1070 was used. Alumina (Al_2O_3), Silicon carbide (SiC) and TiC were dosed as 5 wt% for each case, while laser processing parameters were the same to all samples. Samples with Al_2O_3 formed pores, supposedly due decomposition of the oxide, while samples with SiC presented severe cracking and the largest hardness increase. The TiC particles (TiC_p) reinforced material showed the best results, with no cracks or pores, increase in hardness and good deposition geometry and processability.

2.3 Ceramic particulate reinforced MMCs through laser additive manufacturing

A recent trend in the development of particle reinforced metal matrix composites is their production through laser additive manufacturing. The process chosen for an MMC's manufacturing directly affects possible component geometries, microstructure and final properties [46]. LAM allows almost free-form component construction, provides localized control over material microstructure, and enables access to novel solidification conditions. These characteristics are what make DED-L and other processes included in the LAM group, versatile and promising tools for MMC production.

When producing MMC_ps by LAM, a proper design of feedstock materials and process parameterization induces reinforcement precipitation or reinforcement solubilization; these are two manufacturing routes, and yet another classification for the LAM-MMCs. *In-situ* MMCs are precipitation-induced and follow the broader definition of MMC, their reinforcement phase is generated during processing by precipitation of a secondary phase, after complete or partial melting of feedstock materials. *Ex-situ* MMCs introduce a reinforcement particulate into the melt pool, which remains recognizable and does not produce further ceramic phases, thus they adhere to the stricter definition of MMC. In the following paragraphs, the manufacturing conditions, resultant properties and other aspects of these technologies will be described.

In-situ MMC manufacturing is achievable using fusible nano-particles of the desired reinforcement phase or powders with alloying elements designed for reinforcement phase precipitation. Cao *et al.* [56] researched the former method, where they evaluated the effect of the input of energy per millimetre (E) in the wear performance, the hardness, and the resultant reinforcement particle size. Through DED-L, they added 2.5 wt% of a TiC particulate with a 40 nm-mean in particle size. TiC was fused and re-precipitated as a larger equiaxed-dendritic phase (125 to 290 nm); where the larger the value of E, the larger the reinforcement particle were. Larger values of E also increased hardness and decreased wear rate.

Following the latter method, Gopagoni *et al.* and Zhou *et al.* used graphite powder as alloying element to precipitate TiC in two different *in-situ* MMCs [69,70], achieving similar results regarding wear and hardness to Cao *et al.* [56], but with different matrixes and higher percentages of reinforcement particles. Hardness increases in nano-reinforced and micro-reinforced MMCs happens due to different mechanisms. Nano-reinforced materials, as the ones just mentioned, have their hardness enhanced majorly by grain size refinement [3] and dislocation anchoring, but micro-reinforced materials are also improved by distributing indentation load thought the particle's interface with the matrix.

Ex-situ MMCs may be produced by addition of nanoscopic and microscopic reinforcements, however, microscopic particles are more likely to survive laser processing, since they have more volume to melt before losing their identity. A considerably larger number of authors have studied ex-situ MMCs, adding weight fractions of reinforcement particulate from 5 to 50% of various chemical compositions. Abioye *et al.* [36] and Huebner *et al.* [71] worked with tungsten carbides, highlighting the increase in carbide dilution with increases in *E* and the amount of particle reinforcement. The same was detected to a lower degree by LAM processing Ni-base superalloys reinforced with Cr_3C_2 [72] and TiC [55], however, no analysis on the effect of the amount of particle reinforcement was done. Notably, *E* is a parameter commonly used to analyse the microstructure response to processing conditions.

Most of the recent works done, focus in the application of MMCs as coatings, hence there is focus in corrosion and wear resistance, properties reported to enhance when reinforcement amounts and processing parameters are optimized. Bakkar *et al.* [68] and Xu *et al.* [5] added micro-TiC particles to Inconel 625 and compared MMC corrosion resistance at potentiodynamic polarization experiments to the pure superalloy, registering that corrosion resistance was improved for exposure to solutions containing NaCl and H_2SO_4. Similar result was measured in another work for Inconel 625 reinforced with tungsten carbides and exposed to NaCl [36]. Meanwhile, the commonly expected of wear resistance when increasing the hardness of a metallic materials was also reported, all works cited at this paragraph's end described that when hardness increased wear resistance to pin-on-disk tests was also increased. This being regardless of the reinforcement particulate size [55,57,68,69,72].

Looking at applications other than coatings, researchers also aimed to improve the tensile and flexural behaviour of nano- and micro-reinforced MMCs. For this, particle size was reported to be kept at values bellow 10 μm, supposedly to avoid the easy cracking of reinforcement particles or the nucleation of defects by them, especially when the material is under stress. In fact, the works of Bi *et al.* [3], Hong *et al.* [4] and Xu *et al.* [5] added TiC particles in amounts lower than 5 wt% to their respective Ni-base superalloy and tested their resultant MMCs for uniaxial tension. They arrived to similar results that indicate an almost all-win scenario where yield strength and tensile strength are higher for the MMC than for the pure superalloy. Elongation was slightly smaller only in Xu's *et al.* [5] results, since titanium carbides were added in layers and agglomerated, however, in the other works elongation was higher due grain size refinement. Gains in tensile and yield strength are also justified by dislocation movement impairment. The flexural Modulus of an Inconel 718-based MMC reinforced by low weight amounts (<1wt%) with TiC nano-particles was reported, by Wang *et al.* [2], to increase the higher the amount of TiC.

None of the listed works above applied heat treatments to their materials prior to analysis. This is comprehensible as the aimed applications, such as coatings, do not include the need for such, but it leaves a gap in material development since much can happen to the properties of an MMC_p during heat treatment.

The use of LAM for MMC manufacturing expands the access to another promising technology. Functionally grade materials (FGM) have, by definition, properties anisotropy with localized displacement which are designed to provide better resistance to the stresses of a given application. FGM research was intensified due to the inherent layer-by layer component construction enabled by LAM as it is possible to alter powder composition during processing. Wilson *et al.* [57] researched the microstructure and wear properties of a FGM manufactured from Inconel 690 and micrometric TiC by DED-L. Wear resistance and hardness increased with TiC_p's weight percentage, which was raised gradually from 0 wt% to 49 wt%. At values above 30 wt% fine dendritic TiC phases precipitated from the partially melted TiC particulate. Ramakrishnan *et al.* [73], made a detailed characterization of the phases formed throughout 16 layers of HY282 Ni-base superalloy reinforced with SiC from 0 wt% up to 15 wt%. Each layer presented different microstructures. Post-processing heat treatment was also applied, and non-treated microstructure and hardness was compared to their heat-treated counterparts. Showing that heat treatment homogenizes the microstructure from each layer, while also increasing hardness due to due to γ' precipitation or linearizing it along the laid layers due to residual stress relief.

3 METHODOLOGY

Figure 10 is a flowchart describing the methodology used in this work. Please, in sake of context, skip to the following topic and use the flowchart just as an overview of the applied methodology. The numbers inside the boxes relate steps and analysis to objectives.

Figure 10 – Methodology flowchart

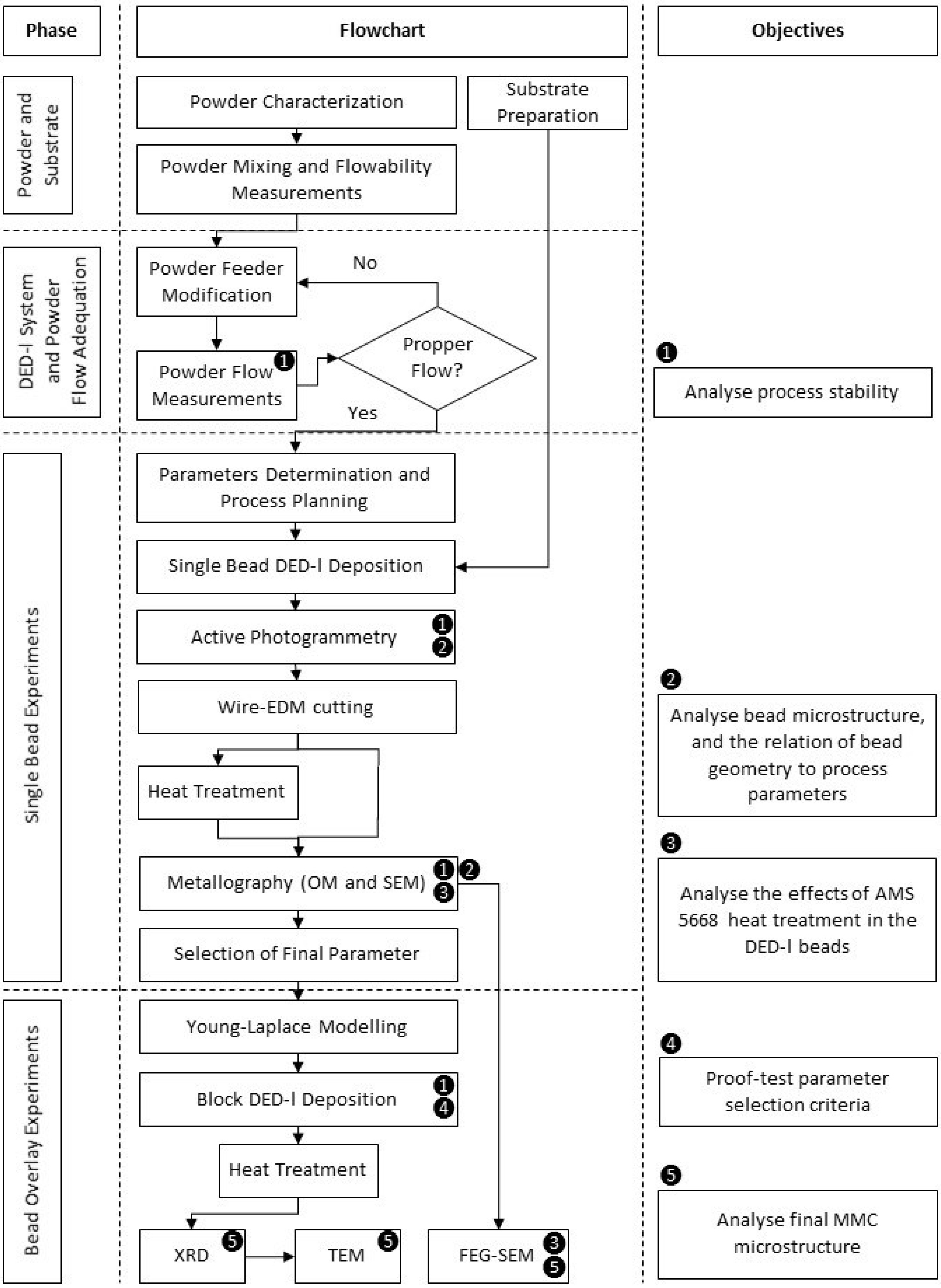

Source: Author

3.1 Powder and Substrate

As already described, Inconel X750 and titanium carbide powders were used in the present research. Inconel X750 hot-rolled substrates were also acquired, aiming to avoid contamination of deposits and allow comparisons between Inconel X750 in its current application condition and the MMC. In the following topics, these resources preparation and characterization are described.

3.1.1 Powder Characterization

Initial powder characterization was done through two technics, scanning electron microscopy (SEM), in a HITACHI TM3000 microscope, and laser diffraction particle measurement, in a CILAS 1190 (liquid mode). Further on, after mixing to the desired proportion, powder mixture flowability was also measured.

3.1.2 Powder Mixing and Flowability Measurements

Mixing was done by low energy milling in a homemade symmetric Y-mixer coupled to a lathe available near to where the final mixture was to be laser processed. The Y-mixer, spamming approximately 30 cm in radius from the rotation axis, having an 40° angle between diagonal arms, an inner edge radius of around one millimetre, and made from tubes of 50 mm in diameter, can be seen mounted in the lathe at Figure 11. A final amount of 300 g was considered enough for laser processing, therefore, by considering the alloy and carbide density as 8.28 g/cm³ and 4.93 g/cm³ respectively, the weights of Inconel X750 and TiC added to the mixer were 271.5 g and 28.5g. Inconel and TiC powders were weighted in a scale with ± 0,1 g. These masses would theoretically result in a MMC with 15% in volume of TiC. The powders were mixed in the lowest ratio of revolutions per minute available, 60 RPM, for 120 minutes, until no perceivable segregation could be seen to assisted eyes.

Figure 11 – Used Y-shaped powder mixer

Source: Author

After mixing, powder flowability was measured following the procedure described in ASTM standards B212-17, B213-17 and B964-16. These standards are based in Hall or Carny flowmeters funnels and the measurements of flowtime of a pre-determined weighed mass or, when measuring apparent density, its weight when levelling powder into a specific volume. Prior to powder mixing, mixture flow measurements and laser processing, the powders were dried in an oven at 110°C for four hours to enhance its flowability. Other than this, none was done to improve powder flowability through the change of its properties, as there couldn't be attempts due to lack of the proper means to it, or since there was the proportion between the powders was fix, not allowing more of the better-flowing Inconel X750 to be added. Therefore, laser processing was to be attempted from a powder in theses conditions, and information extracted from powder flow measurements would be used just as reference or to elucidate the results found.

3.1.3 Substrate Preparation

Inconel X750 substrates were provided in a single block, roughly 14 cm x 14 cm x 30 cm, made of cast hot-rolled non-heat-treated metal. A ten-millimetre-thick slice was cut by wire electrical discharge machining (EDM) from its smaller face. EDM parameters were set to result in the thinnest recast layer possible, then estimated to be around 30 µm. The slice was nonetheless sand blasted with glass microspheres to minimize the inclusion of impurities when laser processing it.

3.2 DED-L System and Powder Flow Adequation

The laser metal deposition system used is fed by an IPG YLS-10000 fiber laser source, with nominal wavelength of 1070 nm, and a GTV Verschleiss-Schutz powder feeder. The powder feeder operates under the operation principle of a rotating notched disk and has only one disk-subsystem installed. Samples are fixed inside a process chamber that will be described further on, relative movement between sample and deposition nozzle is done along three orthogonal axes. The deposition nozzle is a Coax-50-S from Fraunhofer ILT, being it coupled to a Precitec YW-52 welding head to complete the DED laser head. In Figure 12, this assembly and the process chamber designed for powder-fed DED are depicted.

Figure 12 – Deposition head and process chamber

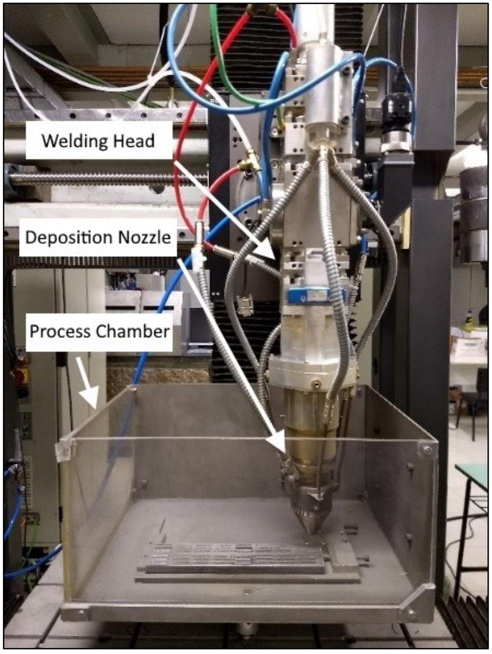

Source: Author

During DED of sensitive or high-performance materials, a process chamber which guarantees an adequate processing environment is often necessary to avoid detrimental reactions between heated materials and the atmosphere. Since the material chosen to be processed here fits this description, a device that would suffice this requirement was designed and built. See Figure 13 for the chamber CAD and Figure 12 for its product.

Figure 13 – CAD of the developed process chamber

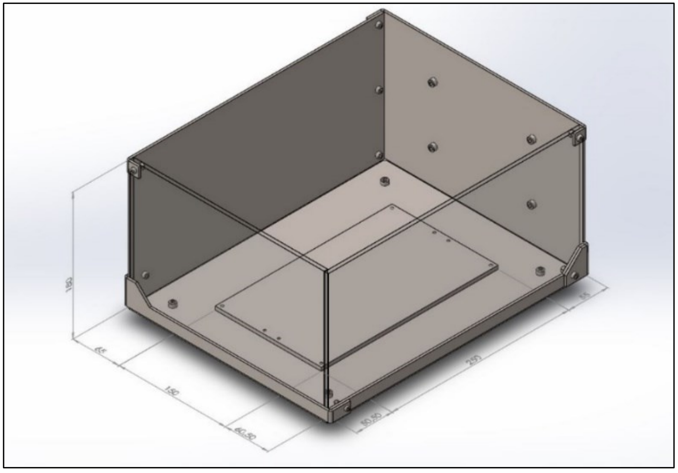

Source: Author

The chamber's operation principle is simple, since argon is denser than breathable air, it travels downwards before mixing with the atmosphere. Thus, if one feeds argon to a tide reservoir at greater rate than its dissipation into the atmosphere, it is possible to produce a gas pond around the process's sensible volume. This is such device ideal use, however, due to shortages in the laboratory’s argon supply, the chamber was used mainly to avoid powder spreading and external perturbations to the process gas flows. After this laser processing phase, it was concluded that the provided protection was enough for contaminants not to affect the conclusions taken here.

In addition to the process chamber, a simple cooling system was also developed to help in the laser processing of the lengthier depositions, which will be described further on. Using a small electric pump, water was pushed from a reservoir into a substrate holder, or support, which by its part forced the water into direct contact with the substrate’s bottom. This system was tested before this work’s experiments, proving to be efficient in maintaining substrate temperature equal to the room temperature in conditions considerably more aggressive than the ones tested in this work. A photography of the cooling system is depicted at Figure 14, it restrains substrate size to a size near to 50 mm x 50 mm x 10 mm.

Figure 14 – Substrate cooling system

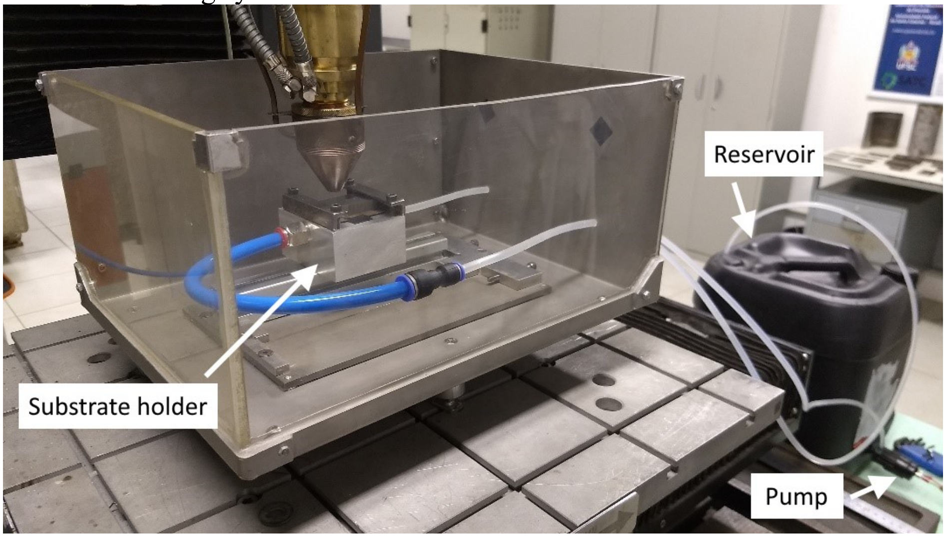

Source: Author

3.2.1 Powder Feeder Modification

Since powder flow was an early concern, another apparatus was prepared even before powder acquisition. This apparatus was a new cylindrical silo with a funnel presenting a steeper inner angle than the one in the original silo. To understand its application, it is necessary to understand the powder feeder system used, for such, a schematic and a photography of both is depicted at Figure 15.

Figure 15 – Description of the powder feeder new silo

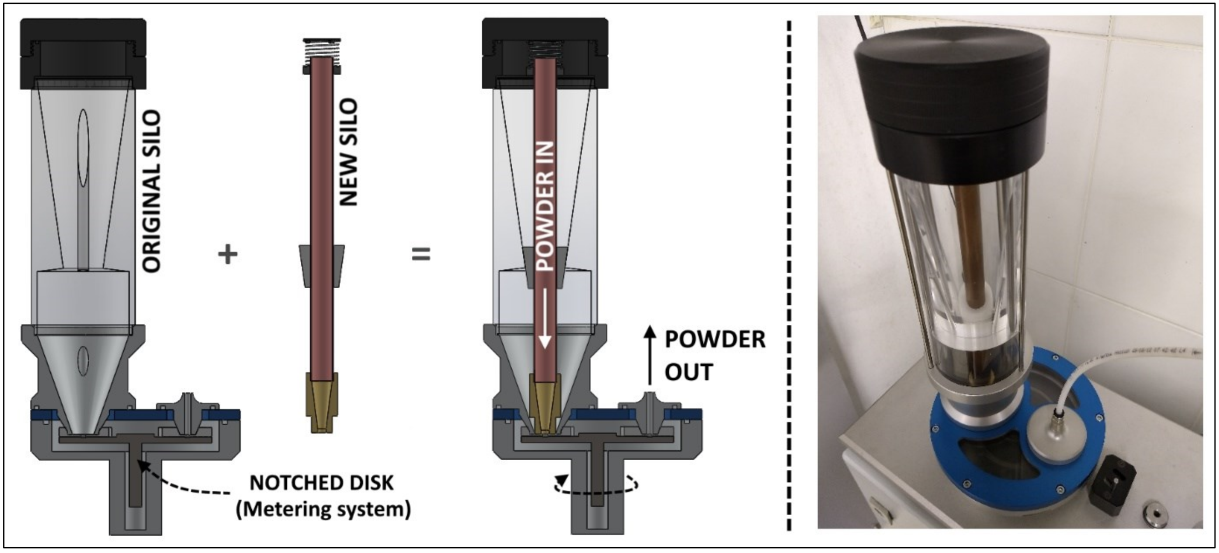

Source: Author

The chosen inner angle and funnel bore were also designed to allow powder to flow more easily than in the Hall or Carney flowmeters, therefore, in the eventuality that the measurements in the calibrated flowmeter funnels failed, it was judged that there still would be a chance that this apparatus would allow powder feeding, due to the stated in section 2.1.2. At Figure 16, one may find a comparison between the inner angles and exit apertures of the flowmeters and the new silo funnel.

Figure 16 – Comparison between the flowmeters and the new silo funnel.

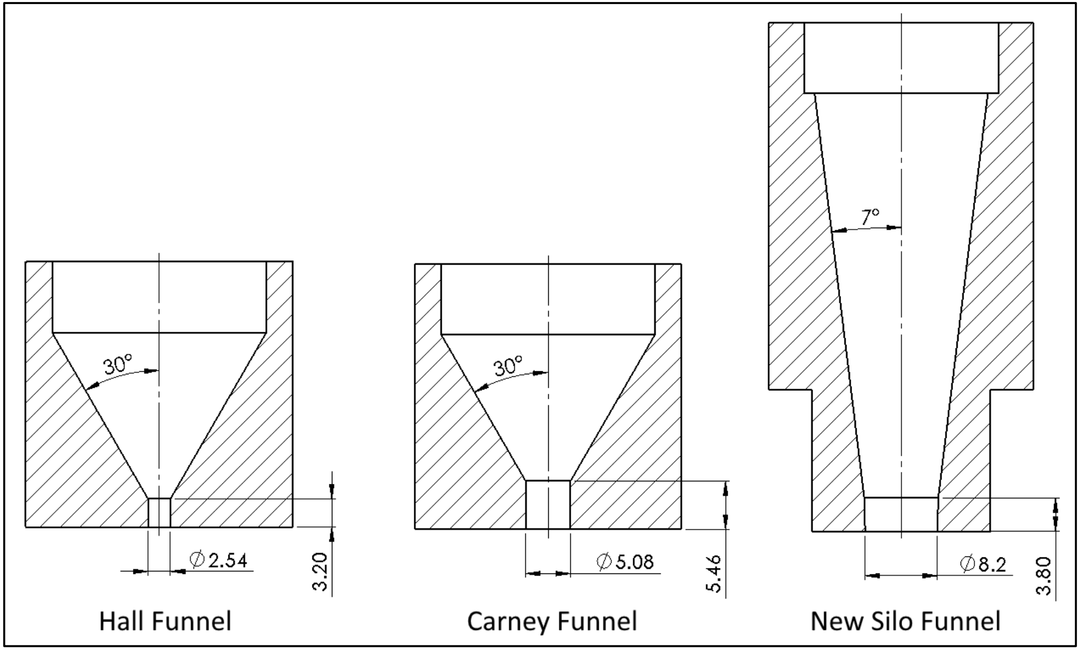

Source: Author

3.2.2 Powder Flow Measurements

As it could be seen until now, steps were taken regarding measurement of powder flowability and the ease of its flow, however, before laser processing it was necessary to infer if the measures taken allowed the powder feeder to provide a constant flow to the deposition nozzle. In other words, if the taken measures worked. Thus, if by some method, it would become evident that proper flow was seemingly achieved, the measurement of the ratio between the powder feeder's rotations per minute (RPM) and the number of grams per minute fed would be used to validate powder feeding.

This measurement was done by setting the powder feeder to three specific RPM and weighting the mass which flew through the deposition nozzle along set periods of time. Weighting was done by catching the powder with a half-filled beaker of water positioned over a scale laid below the deposition nozzle. A photography of this experiment setup is shown at Figure 17.

Figure 17 – Setup form measurement of powder feed rate

Source: Author

As it is expected from a notched disk powder feeder, the plot between powder flow and disk RPM shall result in a straight line. If inadequate linear fitting through the method of least squares would be found, assumed here as to have R² lower than 0.98, another method of powder feeding would be attempted, even if it implied in manually powder-bed feeding MMC powder.

3.3 Single Bead Experiments

To be faced with questions regarding every effect that each processing condition exerts in the outcomes can be considered almost inherent to a study such as this one, however, efforts must be made to not lose track of the main objective and what evidences are being searched to achieve it, therefore, the single bead experiments described in the following were analysed with three points in mind:

- Analyse process stability;
- Analyse bead geometry and derived quantities to main process parameters;
- Analyse the effects of AMS 5668 heat treatment in the DED-L beads.

3.3.1 Parameters Determination and Process Planning

A 3-variable matrixial design of experiments was used. The parameters varied were laser power, processing speed and powder flow. The first two parameters are usual to almost every DED parametrization, but powder flow is not so often found. This parameter was studied here because it was expected that it would directly affect deposition height, thus ensuring the presence of useful beads. The boundaries which constrained each parameter were determined by literature research. One can see at Table 2 the references used and their listed values; all works used laser sources with wavelengths within 1060 and 1070 nm.

Table 2 – References used to define parameters for single bead experiments

Ref.	P_L (W)	V (mm/min)	$\dot{m}$ (g/min)	E (J/mm)	**Material**	**Process**
[70]	350	254	2.57	82.7	Ni+10at%Ti+10at%C	DED-L
[55]	700 - 1300	500	2.4	80 - 160	Inconel 718+TiC	DED-L
[57]	350	1020	10.7	20.6	Inconel 690+TiC	DED-L
[4]	500-800	300-900	2.4	33 - 160	Inconel 625+TiC	DED-L
[37]	800-1000	6000 - 7000	-	6.9 - 10	Inconel 625+TiC	SLM

Source: Author

Most of the slice taken from the Inconel X750 block was destined to be used during single bead parametrization, since it was necessary to use it almost completely in order to fit a relevant number of beads. Based on a minimal spacing between beads and their planned length, 20 mm, a number between 86 and 106 parameter-sets was to be tested. By considering the boundaries listed, this number was determined to be 90. The parameters tested are the permutation of the values listed at Table 3.

Table 3 – Single bead experiments parameters

P_L (W)	V (mm/min)	$\dot{m}$ (g/min)
350	300	2.5
540	440	4.0
730	580	5.5
920	720	-
1100	860	-
-	1000	-

Source: Author

The single bead experiments did not used the developed cooling system, as the whole slice did not fit into the system. Nonetheless, care had to be taken to avoid thermal influence between beads, phenomenon which could lead to misconceptions during analysis of results. Since it would be timewise impossible to wait for the substrate to cool down between each bead, two measures were taken to minimize such effects:

- Beads were laid in random order over the substrate, therefore, mixing eventual thermal influences between beads into measurement errors;
- After each row of beads laid, a process pause was made until substrate temperature went below 40°C. This temperature was measured by K-type thermocouple placed in the centre of the substrate's lower face.

3.3.2 Heat Treatment

After the first laser processing phase, the sample was cleaned from unattached powder particles and each bead was tagged by laser marking to ensure the traceability. In sequence, the sample was sliced by wire-EDM. Each bead was transversally cut, while also separated in groups of three to ease metallographic preparation. The remaining substrate left untouched was cut to pieces that fit the cooling systems; these would later serve for the bead overlay experiments.

Ninety bead halves, each representing a different process parameter set, were heat treated to induce formation of Inconel X750`s application-ready microstructure. This and all other heat treatments in this master work were performed according to AMS 5668 standard for heat treating cast Inconel X750. The cycle there described aims for high creep resistance, having the following stages:

a) Dissolution treatment at 1150 °C for 4 hours, followed by air cooling to room temperature;

b) Stabilization treatment (intermediate aging) at 843 °C for 24 hours, followed by air cooling to room temperature;
c) Precipitation treatment (final aging) at 704 °C / 20 hours, followed by air cooling to room temperature.

The furnace used was a calibrated Jung TB3012 chamber-oven, with ± 1 °C of temperature error and available at LabConf - UFSC. No inert atmosphere was applied.

3.3.3 Single Bead Analysis

Two methods were used to measure bead dimensions, as each had different advantages. Active photogrammetry was used for external bead geometry while cross-section metallographic analysis was used for microstructure and external and internal bead dimensions. Since there is overlapping between these techniques, brief comparison regarding their effectivity in performing this task was also done.

3.3.3.1 Active Photogrammetry

Prior to the EDM cutting described at Section 3.3.2, the laser marked substrate with all beads on top was digitalized by active photogrammetry using an Atos-5 system from the company GOM, this device was available at LabMetro/CERTI – UFSC. GOM also provides a software to handle the data acquired from measurements, called GOM Inspect. However, bead measurement through this software proved not to be simple, thus a Python script was used to convert and handle data from GOM Inspect to a Microsoft® Office Excel sheet. This measurement followed similar procedure to the one done by Gonçalves [74] in her master thesis.

The dimensions acquired through this procedure were, bead height, width, and deposition area. For each bead, theses quantities were measured at 8 locations along their length, thus providing statistics which were used to make considerations over laser process stability.

3.3.3.2 Metallographic Procedure

Both halves of each bead – heat treated and untreated – were cold embedded together in transparent epoxy, providing better handling during metallographic grinding and polishing processes. The metallographic samples were sanded through 80, 120, 220, 400, 600,1200, 2000 sandpaper grits, followed by polishing with 3 μm diamond paste.

Sample etching was necessary to reveal microstructure, allowing the measurement of bead inner dimensions and microstructural analysis of beads. A proper etching should allow analysis of the following features:

- Carbides, being them originated during solidification or added as reinforcement;
- Grain boundaries, to analyse grains size and form;
- The gamma and gamma prime phases, including – if possible – the secondary precipitation of gamma prime;
- Bead dilution into the substrate and heat affected zones.

However, no reagent designed specifically for revealing these features in Inconel X750 was found in the literature, nor for its MMCs. Only reagents designed for revealing one of the listed features or used in similar alloys were found, therefore, based in these options found five reagents were tested, they are listed:

- HF-based (Found in Turazi's doctor thesis [75] and [76]): 61 ml lactic acid, 36 ml nitric acid (65%) and 3 ml hydrofluoric acid;
- Kalling's no. 2 [76] or Waterless Kalling: 100 ml hydrochloric acid (32%), 100 ethanol and 2 g copper chloride (II);
- Reagent 3 [76,77]; 25 ml nitric acid (65%), 50 ml hydrochloric acid (32%), 200 ml distilled water and 2 g copper chloride (II);
- MoO_3-based [78,79]: 15 ml nitric acid (65%), 100 ml hydrochloric acid (32%), 15 ml distilled water, 1 g Molybdic acid and 5 ml of neutral dish soap;
- Adjusted MoO_3-based (Adapted from [78–80]): 30 ml nitric acid (65%), 30 ml hydrochloric acid (32%), 30 ml distilled water and 0.3 g Molybdic acid.

This experiment phase proved to be quite laborious, as etching was performed though immersion and swabbing, with samples having to be analysed through SEM for each etching time set, and finally assuring etching reproducibility. Between etchings, the samples used were re-prepared starting from grit 2000. Only the final etching procedure is described in the results section, but all observations regarding it and the failures are listed in Appendix A.

Macrographs of each bead cross-section were taken by optical microscopy from the metallographic-prepared samples; a Leica DM4000-M-LED microscope was used for such. From these images, bead width, height, melt pool depth deposition area, apparent dilution area and heat affected zone were measured with the image analysis software ImageJ. Higher resolution micrographs were taken with the HITACHI TM3000 scanning electron microscope, aiming for titanium carbide reinforcement and gamma prime precipitates visualization. At this point SEM-EDS was also used to identify phases and attempt to detect carbide dilution.

3.3.4 Parameter Set Selection Criteria

Only one process parameters set was to be used in bead overlay tests. The first criterion for bead selection was low dilution of the bead, without compromising bead weldment to the substrate. The second criterion was high powder efficiency, due to cost efficiency. The third was high deposition rate, and the fourth, if necessary and measurable, was low dilution of the added TiC_p. Powder efficiency (η_{pd}), or how much of the blown powder becomes attached to the substrate was calculated by the following Equation (10):

$$\eta_{pd} = \frac{A_{Dep} * \rho_t * V}{\dot{m}} \tag{10}$$

Being $\dot{m}$ powder feed rate, A_{Dep} deposition area, V deposition speed and ρ_t the MMC's theoretical density, calculated by a pondered average from Inconel X750 and TiC densities. Since small oscillations in A_{dep} could cause high discrepancies in the results obtained from Equation (10), the overall behaviour of η_{pd} against laser power, $\dot{m}$ and V would be considered to guarantee that the results from that parameter set were no outliers.

3.4 Bead Overlay Experiments

Beads laid over a substrate may mix their composition with it. In other words, although the single bead experiments can give interesting results regarding process behaviour and microstructure, the actual MMC with 15% vol of TiC could only be attained if previous layers of similar material were deposited. This was essential to really analyse and eventually compare results with MMCs with the same composition but produced by other manufacturing process.

Considering the mentioned, DED-L manufacturing of an orthohedric volume with dimension equivalent to 25 mm x 19 mm x 8 mm was planned. This volume was to be built in order to provide samples for the final microstructure analysis, proof-test parameter selection criteria, re-analyse process stability, and supply cylindrical samples which would eventually be tested for compressive creep resistance. These creep tests, and their results, are not included in this master thesis, but were planned in alignment to the exposed in Section 1.

3.4.1 Young-Laplace Modelling

Bead overlay implies in changes in bead cross section, since beads are deposited one over another. This makes the prediction of deposition shape difficult and, therefore, hampers coordination of nozzle movement with part growth. In partnership with other co-workers, parallel to this master thesis, a simple and straight forward model was developed to predict the cross-section of several overlaid beads. The complete description of its workings and validation will be described in a journal article yet to be written, however, it was found proper to register its principles here. Preliminar model validation was already registered by Souza in his master thesis [10].

The model is similar to the one proposed by Nenald et al. [81], with one difference, instead of attempting to model every bead cross-section outline with a parabola or an ellipse, the outline is calculated with the Young-Laplace equation, which relates the capillary pressure difference sustained across the interface between two static fluids, thus describing mathematically this interface's shape. This equation is often used to approximate cross-sections of droplets or meniscus in liquid-filled tubes. The form as it was used in the model is described throughout Figure 18 and Equations (11) to (14).

Figure 18 – Coordinate system used for the Young-Laplace modelling.

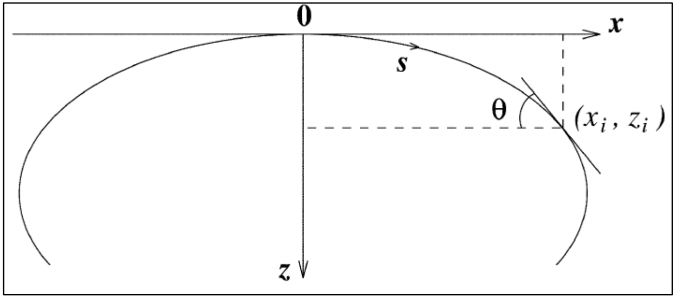

Source: [82]

$$\frac{\delta x}{\delta s} = \cos\theta \tag{11}$$

$$\frac{\delta z}{\delta s} = \sin\theta \tag{12}$$

$$\frac{\delta\theta}{\delta s} = 2 * H + \frac{\rho_{liq} * g}{\gamma_{lv}} z - \frac{\sin\theta}{x} \tag{13}$$

$$\frac{\delta A_{dep}}{\delta s} = x * \sin\theta \tag{14}$$

Being H the (initial) curvature at the apex, ρ_{liq} the liquid's density, g the gravitational acceleration, γ_{lv} the surface tension between liquid and vapor, θ the tangential or wetting angle, and A_{dep} the bead deposition area. The variables x and z are also used in calculations regarding bead width and area. Note that ρ_{liq}, g and γ_{lv} from Equation (13) may be treated as constants. The values assumed for these constants during modelling were 7.54 (g/cm^3) [83], 9.81 (m/s) and 1.85 (N/m) [84,85], respectively. Other than theses values, width and deposition area are the only other constraints given to the model for it to plot the case which describes the outline of a given bead. For bead overlay, overlapping percentage, and number of layers and tracks are also inputted. The model assumes *A* to be constant from one bead to the other regardless of its shape, this is an approximation which has been already proven adequate for most cases by Nenald et al. [81].

Overlap value, number of layer and number of tracks were interactively set to provide a prediction that had flat layers, which are less prone to defects such as lack of fusion, but that also achieved the target deposition volume, with some extra margin. All computations were done in Matlab 2018a and took around five minutes for each plot.

3.4.2 Final Microstructure Characterization

Refined microstructural analysis, focused in secondary gamma prime precipitation and phase identification, was planned to be executed in samples extracted from the final heat-treated DED-L deposition. Albeit, due to the possibility of extracting more information from the single bead experimentation done, additional analysis was also done in three beads chosen.

The criteria used in the beads' selection was not the one described at Section 3.3.4, but the following: they had to be all in one of the samples cut, have similar dilution to the substrate and contain different inputs of energy per millimetre (*E*). The intention behind these criteria was to deepen the knowledge regarding the effect *E* in carbide dilution. Thus, the concern for the choice of beads with equivalent dilution is justified as an attempt to isolate the influence of *E*, since more substrate mixed into the melt pool is likely to increase the susceptibility for carbide dilution.

3.4.2.1 Transmission electron Microscopy

Sample preparation for TEM was done mostly manually. A 1-milimitre slice was cut by diamond wire cutting from the final MMC. This slice was reduced to a thickness of 75 µm by grinding the sample with the same progression of sandpaper grits and polishing described at Section 3.3.3.2. Both sides of the samples were grinded and polished, and thickness was measured with an ±0.01 mm micrometre. From this thin slice, as many 3-milimeter disks as possible were punched in a small die puncher. These disks followed to the electrochemical polishing procedure.

Electrochemical polishing is done with the objective of forming a hole with edges thin enough for the TEM's electron beam to go through it. This requires calibration of polishing process parameters; therefore, more than one sample was prepared to feed this parametrization. A TenuPol-5 from Struers, which works with the "twin-jet" design was used at all electrochemical polishing procedures. The chemical used was a mixture of a third of methanol with two thirds of nitric acid (65%) at -10°C, as described at standard ASTM E1588-09 for when polishing aluminium alloys. This reagent was used for this work's MMC since it was already successfully applied by the laboratory in works with nickel-based superalloys. After electropolishing, the samples were taken to the microscope for analysis. The complete TEM-sample preparation procedure, including notes regarding etchant handling, is described in Appendix B.

TEM analysis were done in a JEM1011 from JEOL. The targeted regions were the TiC surroundings, and gamma prime precipitates from substrate and MMC matrix. Diffraction patterns were to be acquired if necessary. If secondary gamma prime precipitation occurred, its identity would be confirmed by finding an aperture position in which it shone together with primary gamma prime precipitates, since aperture size could not be reduced to allow selected area diffraction (SAD) exclusively from the secondary precipitates. Detailed morphology of carbides and gamma prime was also expected to be observed.

3.4.2.2 X-Ray Diffractometry

Before electropolishing the samples for TEM, an attempt to characterize the MMC phases by XRD was made. Based on the angle boundaries and peak positions found in the literature [8] for TiC and Inconel X750, a MiniFlex600 XRD from Rigaku with a copper X-ray source was used to scan the samples from 2θ equal to 25° until 115°. Angle stepping was done in 0.025° intervals with one-second of acquisition times at each step. The software used for indexing XRD peaks was Match!3 from Crystal Impact.

3.4.2.3 Higher Resolution Scanning Electron Microscopy

Although visualization of gamma prime precipitates was to be done mainly by TEM, a JEOL JSM-6701F Field Emission Gun-Scanning Electron Microscope (FEG-SEM) was also used to complement these results, however, the samples analysed by FEG-SEM were not the final depositions, but single beads. FEG-SEM was also used to analyse carbide dilution and compare heat-treated with untreated samples. Chemical composition quantifications were done thorough Energy Dispersive X-ray Spectroscopy (EDS).

For insertion into the high vacuum required for this microscope model to function, samples were taken out of their plastic embedment. They were not gold-coated and were only grounded with copper tape. Abstaining from these measures seen to hamper visualization of nanoscopic phases. For gamma prime’ visualisation, the acceleration voltage was set to 5 kV and the working distance to 6.4 mm, while a 15-kV acceleration voltage was used for other imaging and EDS.

4 RESULTS AND DISCUSSION

The results are mostly described in three major section, addressing power related issues, process analysis and microstructural analysis. Additional results are mentioned as they were faced during experimentation.

4.1 Powder Characterization and Flowability Results

The SEM images taken from the powders, shown at Figure 19, evidence the manufacturing process which made each of them, gas-atomization for Inconel X750 and milling for the TiC powder. They also indicate one of the reasons why it was expected that the mixture from them would have low flowability, TiC particles jagged morphology does not favour flow.

Figure 19 – SEM images from TiC (a,c) and Inconel X750 (b,d) powders at different amplifications

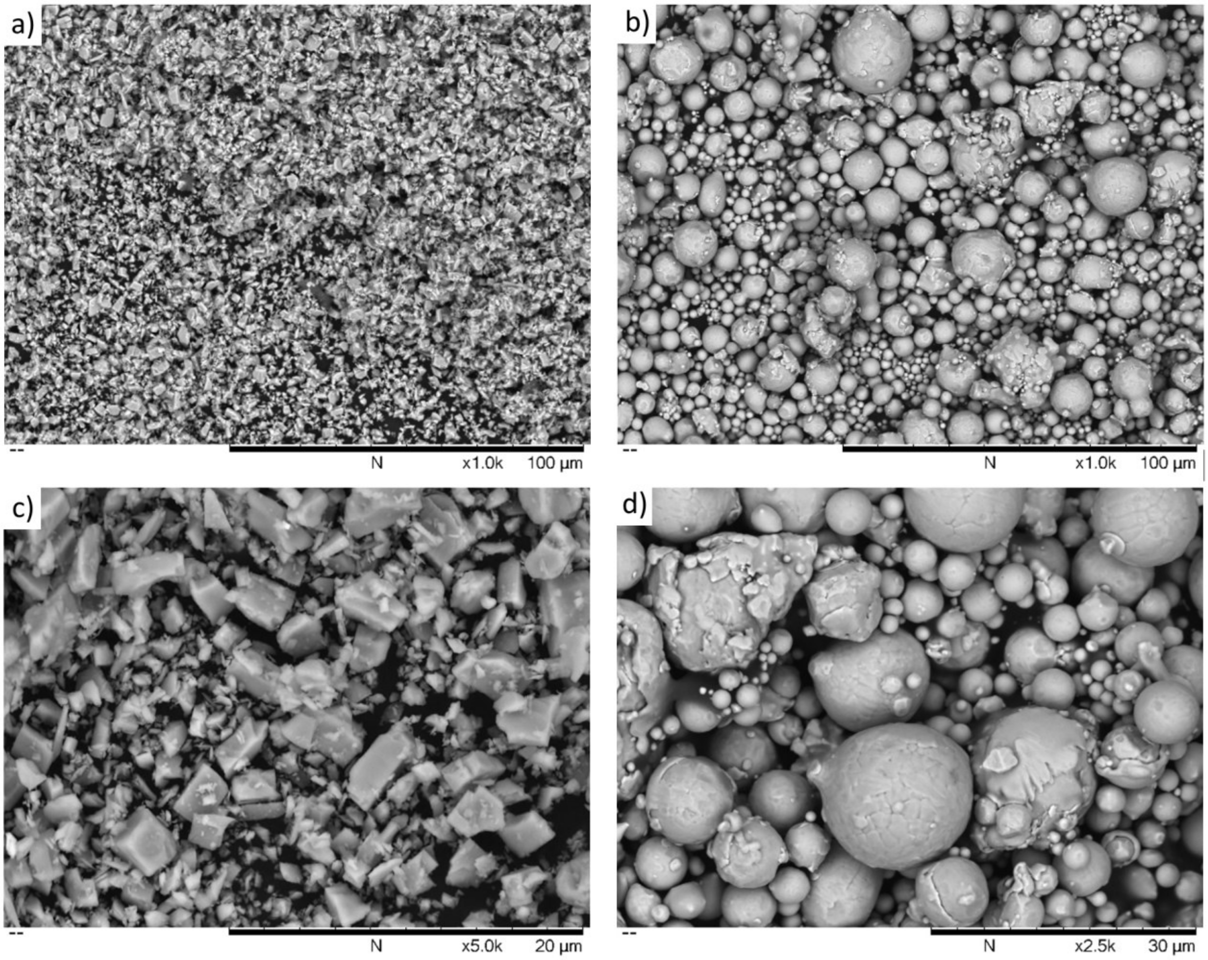

Source: Author

Complementing the results from SEM, the measured particle distribution in volume from each powder is shown at Figure 20, together with the theoretical distribution for the MMC with 15% vol of TiC particles. The TiC particles diameter ranges from 0.18 µm to 3.29 µm (10%-90%), while Inconel X750 particles range from 8.02 µm to 24.05 µm. Both powders have bi-modal distributions with peaks that do not overlap when mixed, thus providing a mixture with multimodal distribution.

Figure 20 – Measured powder distributions (a) TiC and (b) Inconel X750, and the theoretical distribution for the mixture.

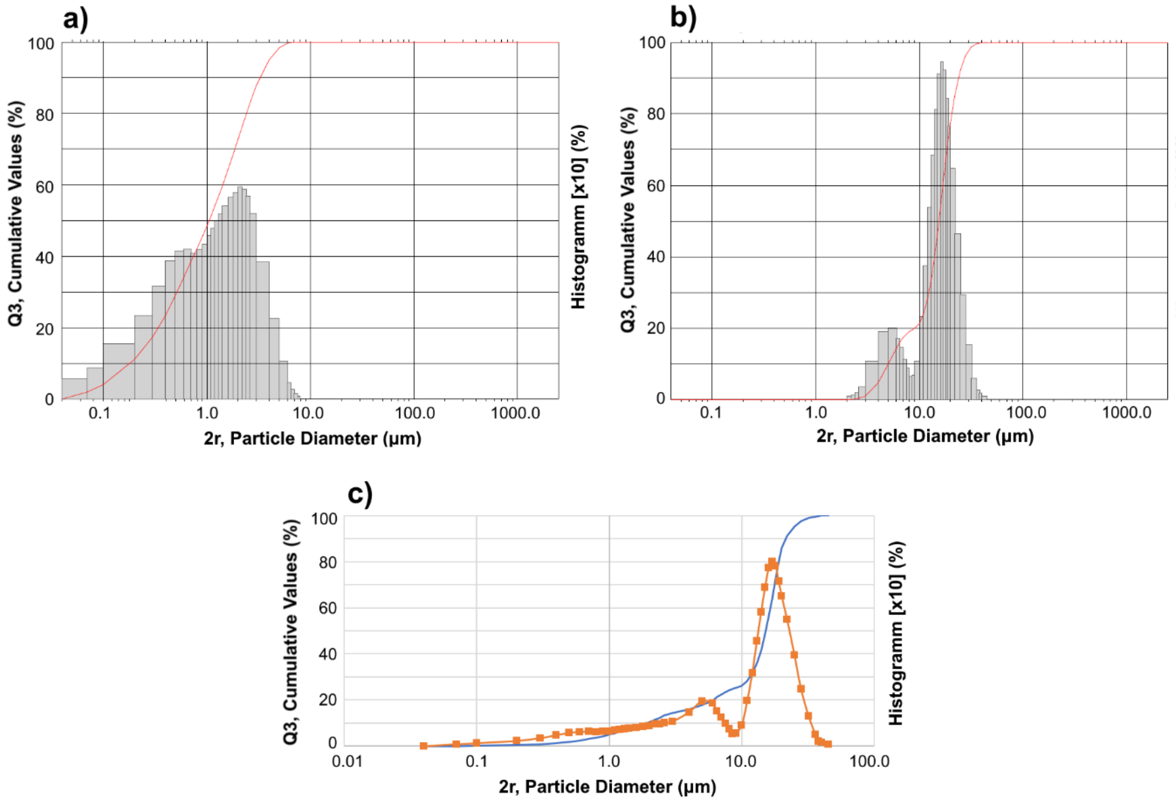

Source: Author

The type of distribution shown in Figure 20.c is proper for mechanical sintering but is not likely to have good powder flow. Particles from smaller mode are prone to lodge themselves in the spaces formed between particles of the next larger mode, increasing the friction coefficient of the powder mixture.

Flowability measurements from Hall and Carney flowmeters confirmed the expected from the two previous analysis, as the powder mixture did not flow freely through neither of them. A photography taken from the filled Carney flowmeter with his outlet open, but no powder flowing is shown at Figure 21.

Figure 21 – Powder mixture fails to flow in Hall and Carney funnels.

Source: Author

4.2 Powder Flow Adequation

Regardless of the results achieved in the analysis described at Section 4.1, an attempt to feed powder to the powder feeder disk with assistance of the device described at Section 3.2.1 was done. Unfortunately, it did not provide a constant powder flow, albeit slight improvement was seen from using the powder feeder without it. Since the powder flowed intermittently measurements of powder flow were not done for both cases.

After these failures and, more significantly, seeing the behaviour of the powder mixture, another solution was proposed to the problem regarding powder feeding into the notch of the powder feeder's disk. The mixture was to be manually spread into it, while a simple replacement of one of the powder feeder's components would allow the minimal 20-seconds processing window, enough to perform the planned experiments.

The component substituted was the spreader, a polymeric component which is the interface between the silo's funnel and the notched disk. This component has a small relief in its lower part that fits the disk's notch, restricting the amount of powder that can be on the notch at one given time. By replacing the spreader with substitute without the notch, it became possible to have the whole notch filled at once and achieve the necessary processing window. The replacement is clarified at Figure 22, bellow, where the notch already filled and ready for processing can also be seen.

Figure 22 – Powder feeder component replacement to achieve minimum processing time

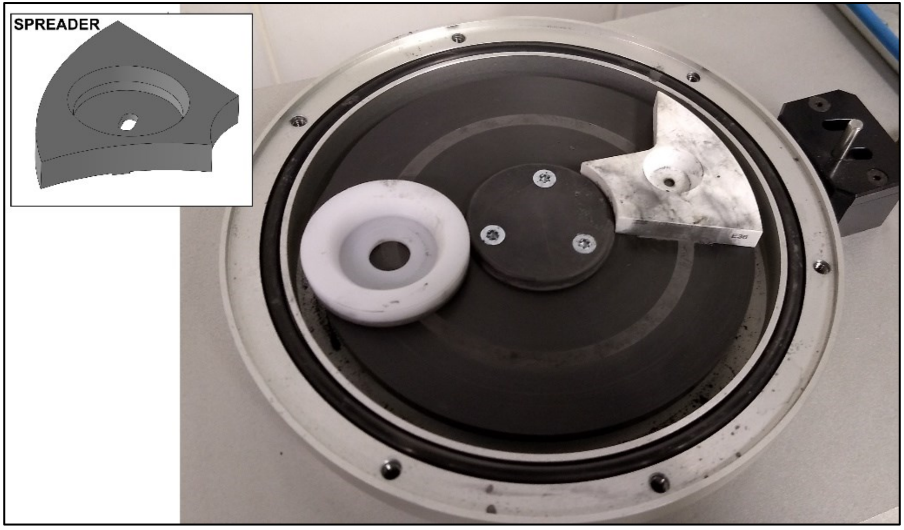

Source: Author

The powder feeding procedure consisted in opening the powder feeders' upper section to allow access to the disk, laying the powder into the notch and levelling it with a straight edge. This theoretically left the feeder ready for a short period of DED-L. The length of the processing window would be defined by the RPM set for the disk to spin, being 2.2 RPM the maximal possible value which would still allow useful processing time. A picture of the powder feeder's disk in loading process is shown at Figure 23.

Figure 23 – Powder feeding procedure of the disk's notch

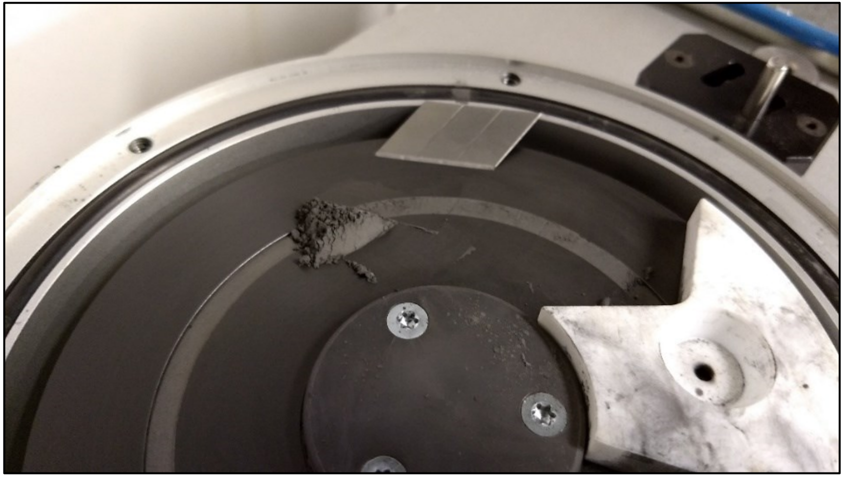

Source: Author

Process gases were calibrated prior to powder flow measurement, being 5 l/min and 10 l/min set for carrier and shielding gas, respectively. The powder feeding procedure was tested following the described in Section 3.2.2, and it showed good correlation. Linear fitting was performed over the acquired data, resulting in a R^2 of 0.9902. Due to the restriction in processing time, the measured flow rates were calculated from weights formed along different time periods. The graph representing the data acquired can be seen at Figure 24 – Relation between $\dot{m}$ and revolutions per minute.

Figure 24 – Relation between $\dot{m}$ and revolutions per minute

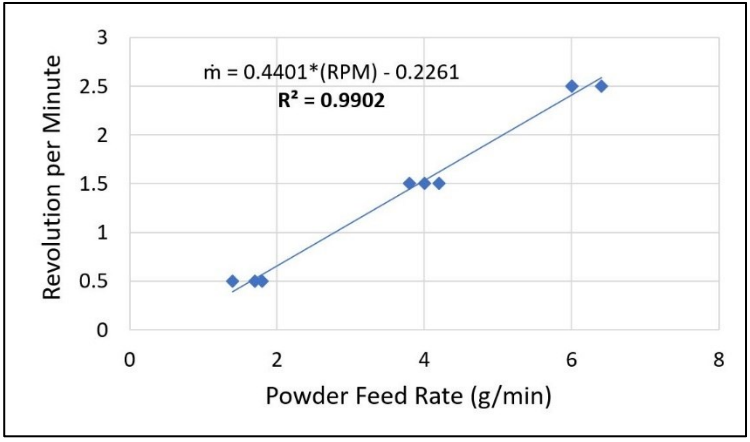

Powder flow is one of the main concerns regarding process stability in DED-L. Achieving a linear fit such as the one shown, indicated that process stability was in stage adequate to move to further experiments.

4.3 Process Parametrization – preliminary results

Processing occurred exactly as stated in Section 3.3, with only two differences, powder was also refilled during the cooldown time and each row of parameters had a single $\dot{m}$, being the rows themselves also randomly displaced. In Figure 25, the sample with the beads on top and the under-attached thermocouple is shown by the side of its digitalization by active photogrammetry.

Figure 25 – The just laid DED-L beads (a) and their digitalization by photogrammetry (b)

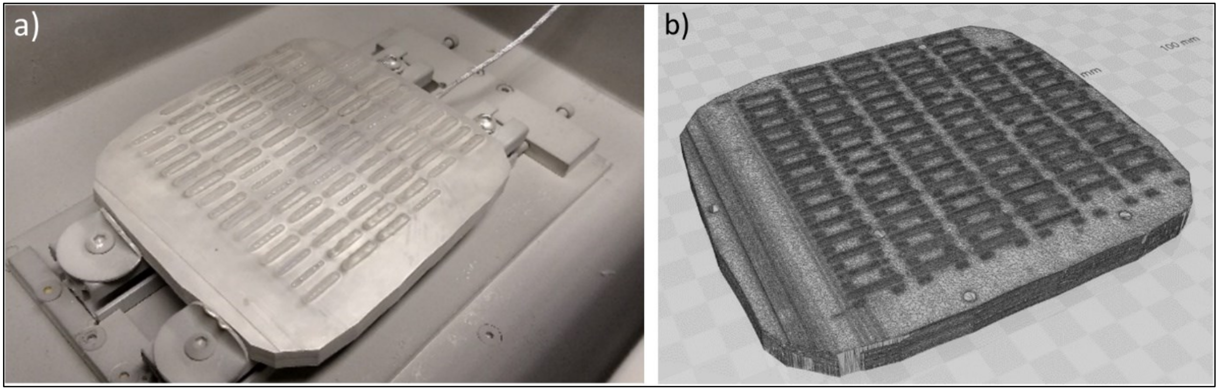

Source: Author

In the as processed sample, it was possible to see that unexpected small oscillations in powder flow caused bumps and widenings in the deposited beads. These seemingly random topographic defects were registered by the digitalization, as well as the laser markings which were done just before. The data extracted from the digitalization will be discussed further on, for now, it suffices to say that these defects were then considered to be irrelevant to most of the other analysis and tests still to be done, as there was still plenty of length in a defected bead which could be analysed without interference.

In sequence, the sample was EDM cut and laser marked. Heat treatment was successfully done, with heat-treated samples presenting different tonality due to oxidation. The laser markings survived this process. Metallographic preparation also strictly followed the stated in the methodology, were samples were prepared together with their other half. Illustrations from the samples after these stages can be seen at Figure 26.

Figure 26 – Steps for single bead analysis: EDM (a), heat treatment (b), grinding (c)

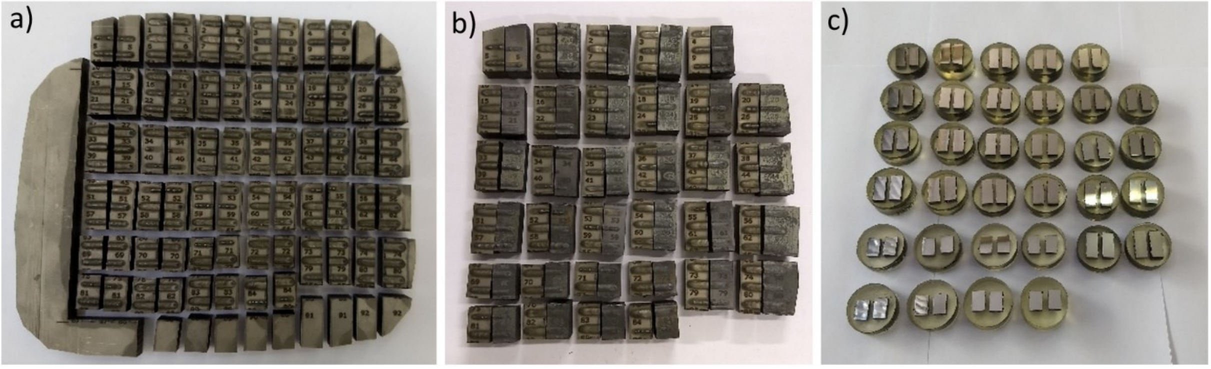

Source: Author

The only metallographic etchant which permitted the visualization of all targeted microstructural phases and granted reproducibility was the “Adjusted MoO_3”, its application was done by slow swabbing with lens cleaning tissues through 150 seconds for each embedded sample. Cotton swabs, normally used for this task, severely scratched the samples during etching. Both untreated and heat-treated samples’ halves received the same etching time. Therefore, this timespan was adjusted to provide better observation conditions in the heat-treated half. Although interesting structures could still be seen in both. Examples from the extracted micrographs by optical microscopy are depicted at Figure 27. Further on, more micrographs will only be used when exemplifying results.

Figure 27 – Examples of OM images acquired from the transversal sections of heat treated (b) and untreated beads (a). The images exposed are referent to the bead deposited with 730 W, at 440 mm·min^{-1} and feeding 5.5 g·min^{-1}.

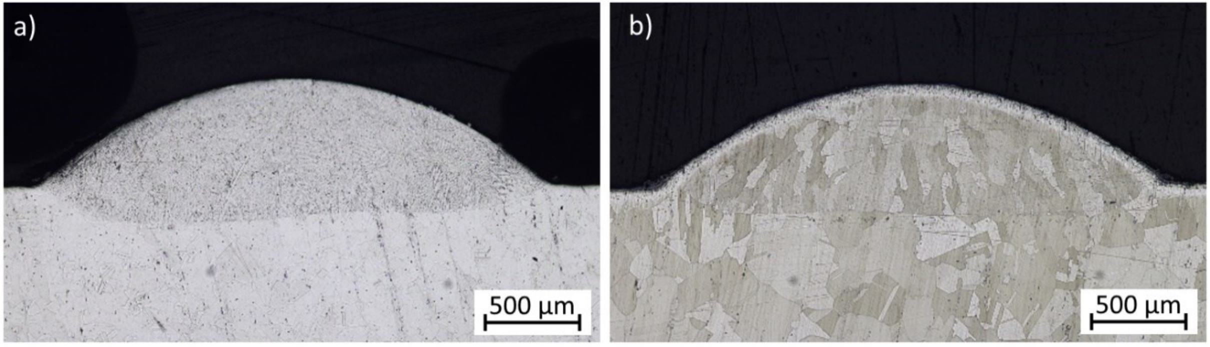

Source: Author

4.4 Corrosion and dislocation etching of MMC single beads

An approximately 65 ± 6 µm thick white layer could be seen along the surface of all heat-treated samples, Figure 27.b. This layer was analysed by EDS-SEM linear scans, Figure 28, and proven to be depleted of chromium, an element included in Ni-base superalloys to provide corrosion resistance [53,54]. During heat treatment chromium partially diffused to the surface and reacted with the heated oxygen in the atmosphere, forming an oxidized layer above the Cr-depleted layer. EDS-SEM measurements in the untreated sample are also presented for comparison between the conditions. The formation of this white layer brought up another relevant consequence of adding TiC particles into Inconel X750. Corrosion resistance of DED-L beads was seemingly lower when compared to substrate`s, as evidences were found which indicated that TiC particles may sensitize the immediate region around them.

Figure 28 – EDS-SEM analysis of the white layer, depleted of Cr in heat treated samples.

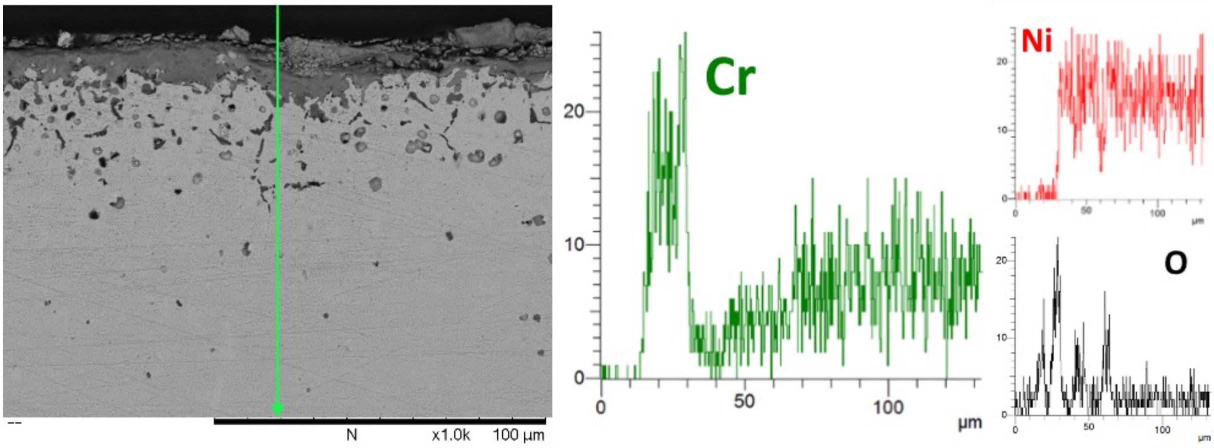

Source: Author

Figure 28 – Continuation. Untreated sample`s surface EDS-SEM analysis for comparison.

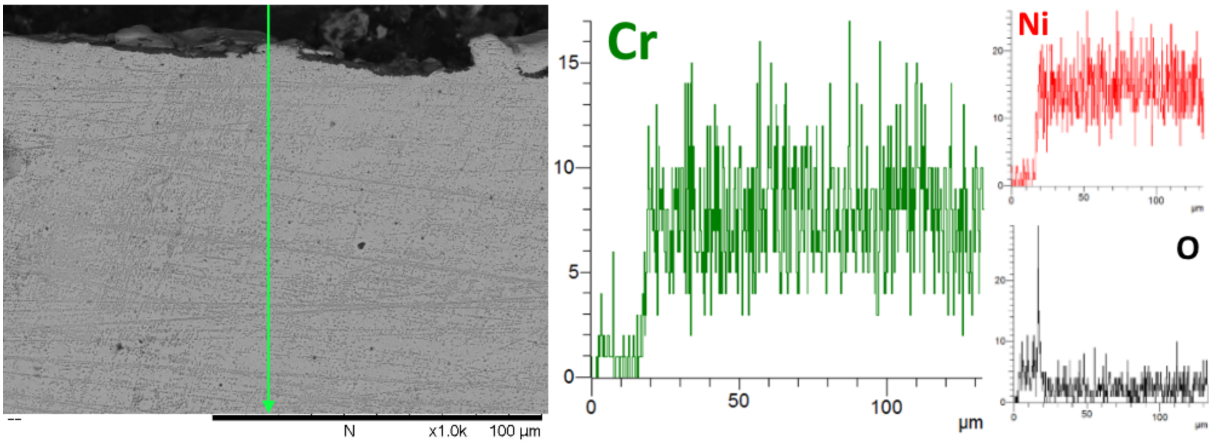

Source: Author

These evidences, as one may suppose, are not differences in white layer thickness from substrate to MMC, but are the presence of pyramidal holes, or pits, dispersed in the layer, being them considerably more frequent in DED-L beads than the substrate. The pits are formed during metallographic etching, apparently exists some relation between these structures and laser processing parameters, although, since this was not this thesis focus, this relation was not quantified to allow deeper study. Nonetheless, the opportunity was taken to study what caused this phenomenon; at Figure 29, micrographs from these formations and an EDS point analysis revealing a still-attached TiC_p inside of one of the holes can be seen.

Figure 29 – Several pyramidal pits inside a Cr-depleted layer (a), EDS-FEG-SEM measurement points of a TiC_p still inside of a pit.

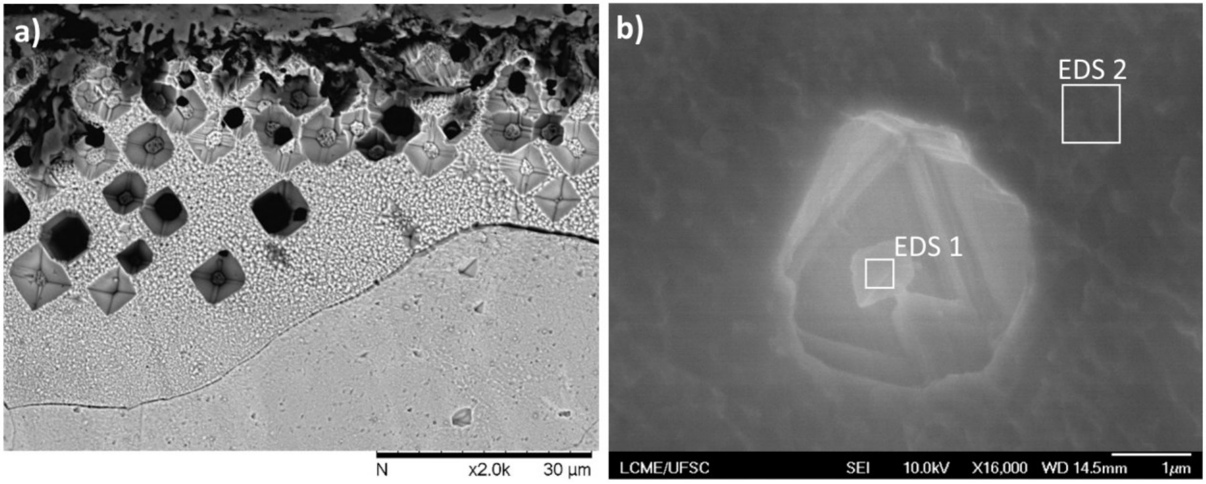

Source: Author

Figure 29 – Continuation. EDS measurements referent to the previous images. Note the different contents of Ti, Nb and C.

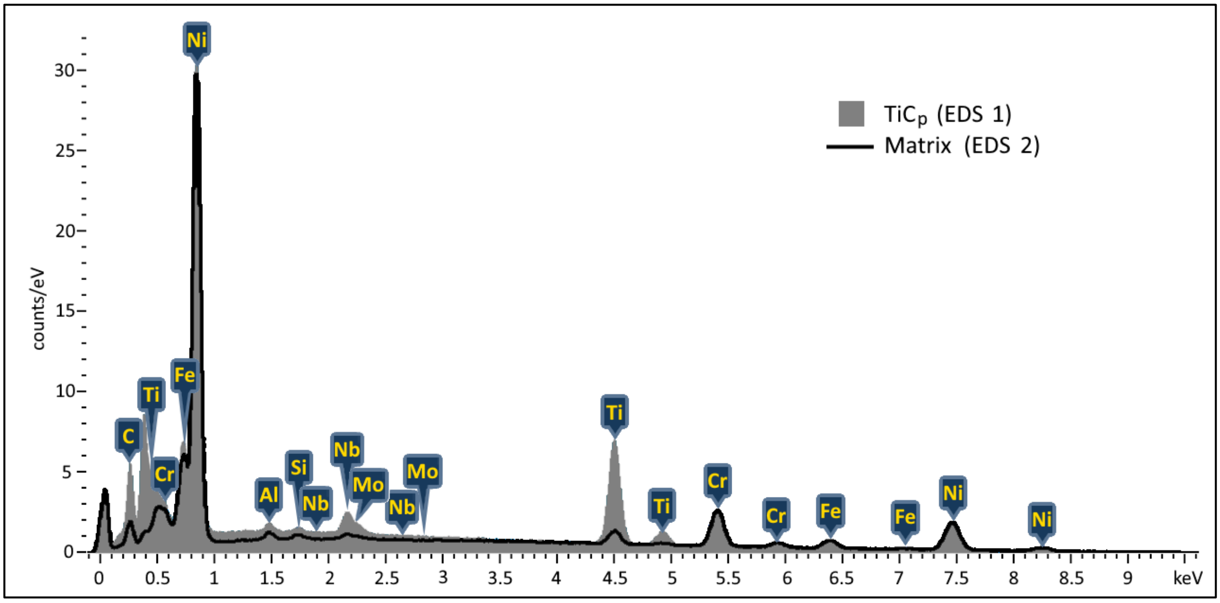

Source: Author

Figure 29 sustains the hypothesis exposed one paragraph earlier, indicating that not only TiC particles ease corrosion, or etching, but also that corrosion occurs aligned to the materials' crystallographic planes. Otherwise there is no explanation to why all holes in a grain are equally orientated or in such geometric shapes. More so, these holes were also found in the non-treated samples, however, in a considerably scarcer dispersion and smaller in size and spread out along the whole samples. Proving that this corrosion mechanism is inherent to the alloy but is intensified by chromium depletion and the inclusion of carbide particles.

A reason why the TiC particles caused preferential etching was searched and found to likely be a phenomenon called dislocation etching, or *Kristallfigurenätzung* in German [76,86–88]. This phenomenon occurs in very specific conditions, presents geometric pitting aligned to crystalline lattices, and it is even used to quantify the occurrence and distribution of dislocations along a given material, being a technic used in semiconductor research [89]. Thus, if we consider that the thermal expansion misfit between particle and matrix caused dislocation punching, as described in section 2.2, we could suppose that preferential etching occurred due to the presence of high concentrations of dislocations.

All these unexpected results lead to two suggestions for further works, which are this MMC's corrosion resistance relation to the microstructures formed by laser processing, and the search for confirmation of a higher dislocation presence around carbides through selected area diffraction patterns by TEM. However, if dislocations are indeed more present around carbides than along the matrix this could justify why gamma prime precipitated more finely around TiC particles, as it will be described further on in section 4.6.2.

4.5 Process Analysis

From here on, the remaining results are divided in two main sections, process analysis and microstructure analysis. The first, which is discussed now, will focus in analysing the fine-powdered DED-L results to determine how stable this process is.

4.5.1 Active Photogrammetry

Validating the results from the active photogrammetry measurement was essential to allow the use of the acquired data. To do such, bead transversal profiles were extracted from active photogrammetry data and superposed over micrographs taken from the same beads. Although these micrographs only represent one transversal plane along a bead, they were made as perpendicular as possible to the deposition direction, thus, they are the best representation of actual bead profiles and served as reference in validation of active photogrammetry data. One of the superpositions made is presented at Figure 30.

Figure 30 – Superposition between bead profile measured by photogrammetry and its metallography

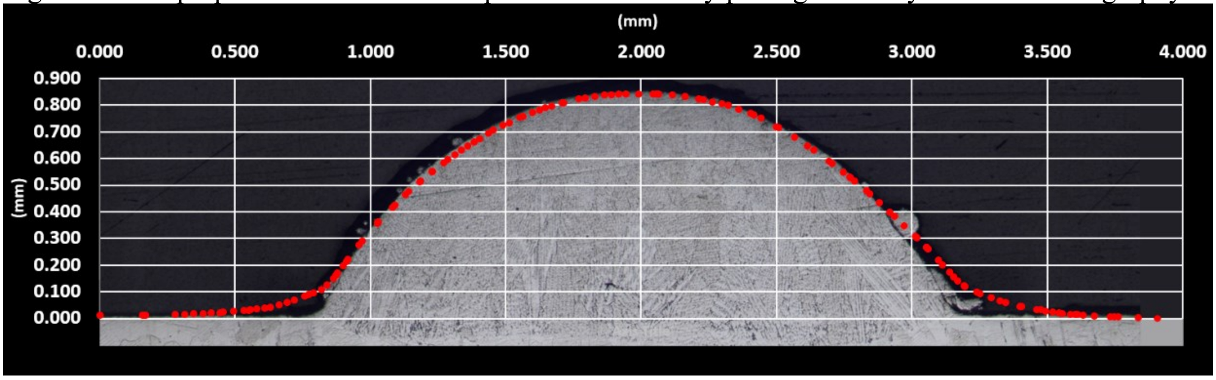

Source: Author

The superposition shows that there is a severe discrepancy near the substrate, between measured profile and actual profile. The cause of this discrepancy may have been lack of lighting, system limitations or, the most likely, lack of colour contrast, feature which helps the technique in defining edges. Regardless of the reason, this mismeasurement happened for all beads, being more noticeable in the ones with a rounder profile. The whole discrepancy resulted in the decision of setting the width measurements aside, therefore, validating only the photogrammetry's height and deposition area measurements which showed precision in superposition and parity to the values measured metallographically.

Thus, by comparing each bead's height standard deviation with the mean height deviation for all beads one could easily identify which regions in the whole parameter set that are likely to cause topographically defective beads. This comparison can be visualized at Figure 31, where all measured values are plotted against the 0.06 mm plane, which is the mean height deviation value for all beads. Points of equivalent $\dot{m}$ are linked by a surface to highlight the regions which stood out.

Figure 31 – Process stability evaluation through bead height standard deviation comparison.

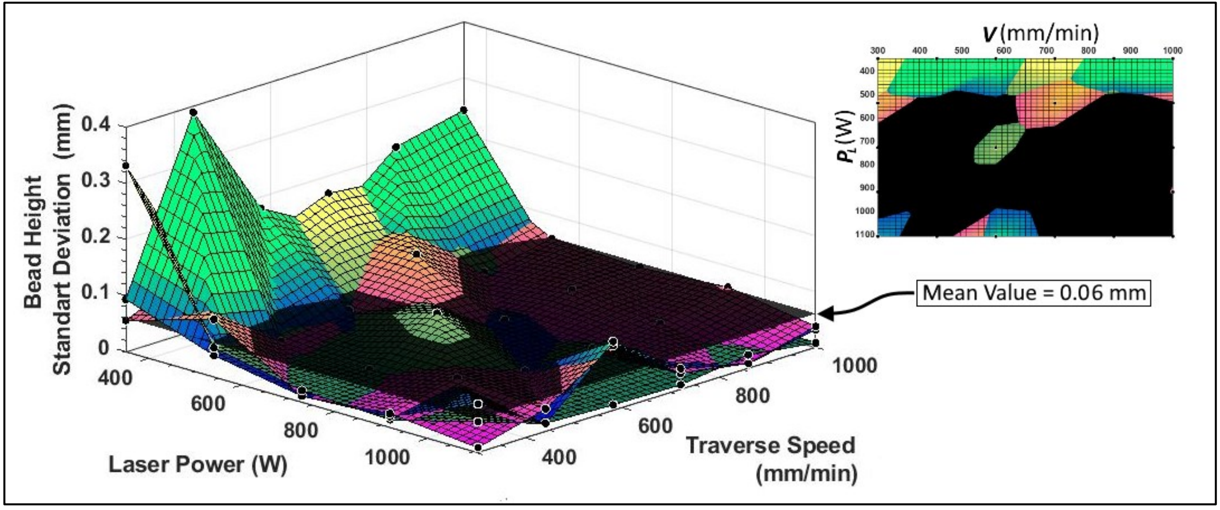

Source: Author

The standard deviation analysis allowed a first selection of process parameters, since the ones in the larger continuous region above the 0.06 mm plane where mostly sets with laser power defined as 350 W. This caused all sets which used 350 W to be disregarded as candidates for the overlaid deposition, as the beads above the threshold were confirmed to be defective due lack of substrate fusion or alike. This result led to the following conclusion, if we insert the 350 W laser power value and the minimal processing speed tested, 300 mm.s^{-1} in Equation (3), a lower limit regarding E when DED-L processing in the conditions tested can be determined, being it 70 J.mm^{-1}; of coursed, this minimal energy input would be for the Gaussian laser spot size of approximately one millimetre in diameter used. Equivalent threshold and results were also established with the mean deposition area deviation, obtaining equivalent results.

Another information extracted from the graph at Figure 31 caused concern over process stability. There were a few localized points above the 0.06 mm plane which were apart from the main region described in the previous paragraph. These points could represent an undetected instability in the process, which was not strongly related to P_L or V, as no evident connection was found between the point and these process parameters.

4.5.2 Effect of Process Parameters in Bead Quantities

With the 350W beads excluded, width (w), height (h) and deposition area (A_{dep}), were plotted against laser power and processing speed to qualitatively analyse this process behaviour. Further on, parameter set selection was to be done, therefore, the three main quantities involved in selection criteria, bead dilution (d), deposition rate ($\dot{D}$) and powder efficiency (η_{pd}), were also plotted against the same variables. At each graph plotted, parameter sets with the same $\dot{m}$ were interconnected by planes, forming surfaces. This allowed the evaluation of powder feeding rate`s effect for each quantity. All these graphs are exposed in the following, at Figure 32.

Figure 32 – Graphs expressing the effect of process parameters in bead quantities

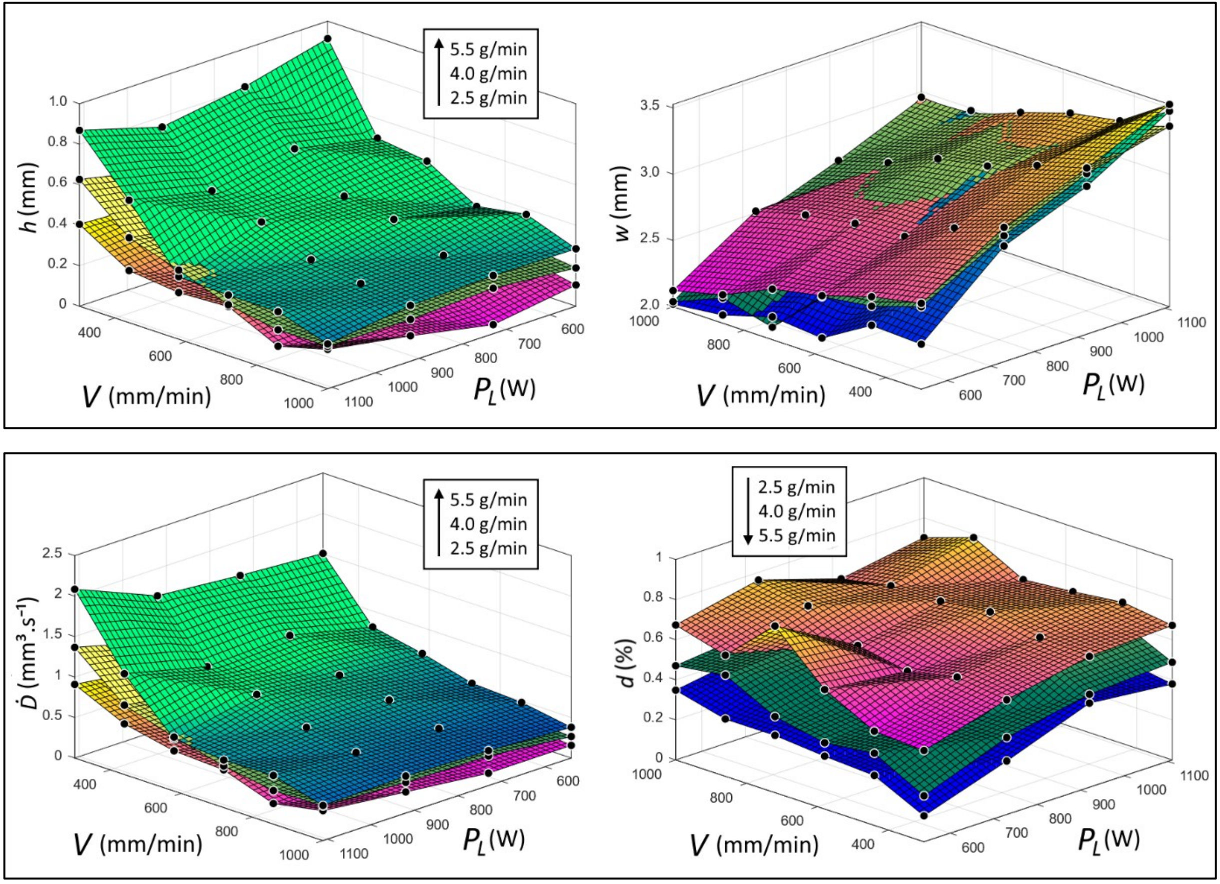

Source: Author

Figure 32 – Continuation. Graphs expressing the effect of process parameters in bead quantities

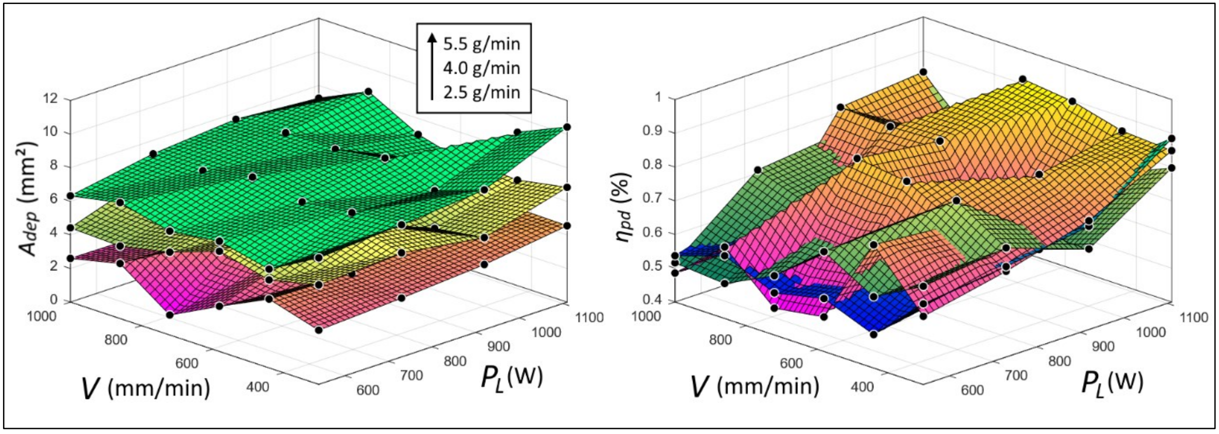

Source: Author

Both deposition area and height are more strongly affected by laser power than processing speed, however, bead width relation to laser power is stronger than to processing speed. Bead dilution and deposition rate, although dependant of processing speed and laser power, has shown greater response to changes in ṁ, albeit in different directions. Deposition rate raises with increases in ṁ, while bead dilution decreases, as it is logical to expect. Powder efficiency has not presented clear behaviour regarding ṁ, which is reasonable as the values used are within the operation range of the nozzle, however, the results indicate that powder efficiency is highly dependent of the laser power set. The higher the laser power, more efficiently will powder be melt, thus adding it to the molten pool and increasing η_{pd}.

4.5.3 Parameter Selection

The relations between outcome quantities and process parameters shown in Section 4.5.2 agree with the described in literature [15,19,20]. Hence, it was reasonable to affirm that despite the oscillations identified by the photogrammetric measurements, DED-L processing behaved in general outlines as expected. With this established, the criteria described in Section 3.3.4 was applied in the parameter set selection for the execution of the overlaid deposition. The first criterion, reduced bead dilution, essentially left a group of four candidates, which have their relevant characteristics quantified at Table 4. This data is organized as it was analysed, from lowest to higher dilutions.

Table 4 – Parameters and quantities of the candidates for the overlay experiments

Parameter Set ID	**$\dot{m}$ (g/min)**	**P_L (W)**	**V (mm/min)**	**d (%)**	**$\dot{D}$ (mm^3/s)**	**η_{pd} (%)**
35	4.0	540	300	23	5.92	69
9	5.5	540	440	25	5.88	50
41	5.5	540	580	26	6.56	56
44	5.5	730	300	27	7.87	67

Source: Author

Parameter set number 35 had the lowest dilution, without presenting lack of fusion. However, this alone was not enough justification to select this set, since in sequence there were parameter sets that resulted in practically similar dilutions but with higher deposition rates. Thus, being powder efficiency equivalent between parameters set 35 and 44, and parameter set 44 having a considerably higher deposition rate, the later was chosen to be used in the overlay experiments. This parameter dimensions, including the ones relevant to deposition modelling, are described in Table 5.

Table 5 – Quantities of the first parameter set selected for overlay experiments

ID	**Bead Width (um)**	**Bead Height (um)**	**Melt Pool Deph (um)**	**Deposition Area (mm^2)**
44	2.87	0.81	0.34	1.57

Source: Author

4.5.4 Proof-test Parameter Selection Criteria

The deposition area and the width from bead 44 completed the data required for executing the Young-Laplace model. Therefore, througth a try and error experimentation with bead overlap and bead and layer numbers, while aiming for the crosection determined by the target volume cited in Section 3.4, the predition depicted in Figure 33 was attained.

Figure 33 – Young-Laplace model prediction for parameter set/bead 44 overlay

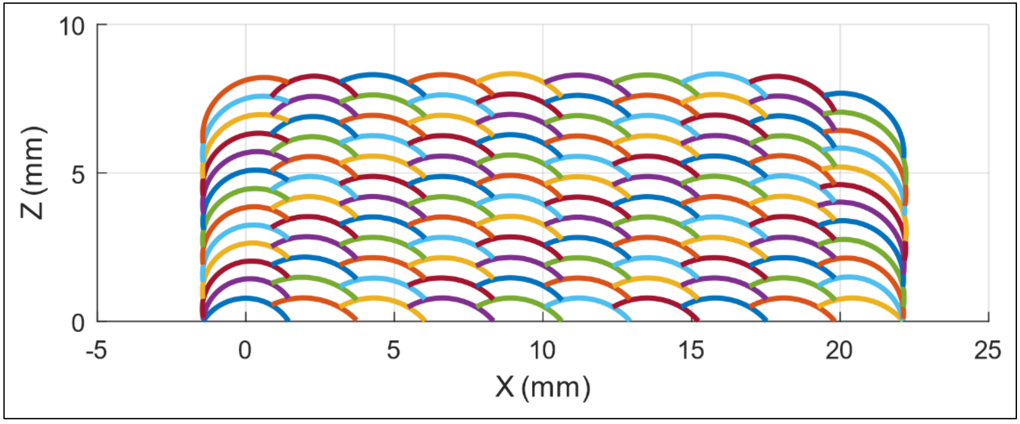

Source: Author

The prediction indicated that ten beads set aside to which other with an overlap value of 20% would form a layer wide enough and reasonably flat. This layer should then be superposed 12 times to result in a deposition with the desired height of eight millimetres. By dividing the predicted maximal height to the number of layers, a nozzle Z-step of 0.695 mm per layer was defined. The last dimension of the target volume is length, which is not modelled by any means, since setting the bead length to the desired value when laser processing is enough.

After preparing the DED-L system with substrate over cooling system, the final deposition was made following a path in agreement with the prediction just shown. The resultant deposition was different from predicted already at first layer completion. This can be seen at Figure 34, were the resultant deposition from only the first layer is depicted.

Figure 34 – First layer of the overlay test with bead 44 showing gaps between the beads

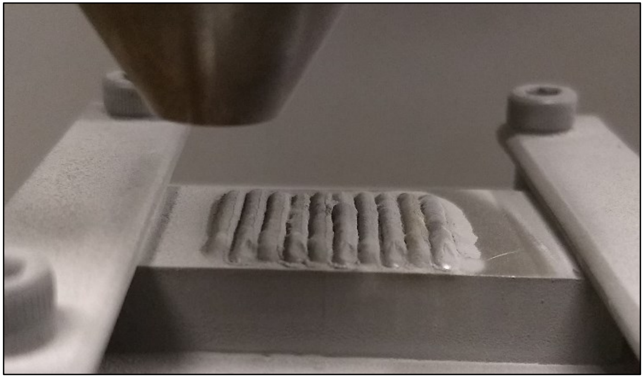

Source: Author

As shown in Figure 34, there is a gaps between the beads laid, resulting in a surface considerably more irregular than predicted. A problem with the Young-Laplace model is that it does not consider heat transfer phenomena, or the defects and perturbations caused by material transformations, such as phase changes or chemical reactions. The model simply assumes that a bead will merge perfectly with the previous. When this is true, the model supposedly shows considerable fidelity with reality, however, when this is untrue, the model fails.

The current experiments being the second case, and a deposition with 15%vol of TiC still being required for microstructural analysis, processing had to be adjusted to overcome lack of fusion. Thus, in order not to lose the costly deposition already made, laser remelting passes were added between DED-L layers to even as-deposited surfaces and remove gaps formed between beads. The paths for this remelting passes were centred exactly between beads, while process parameters were equal to DED-L ones, but without feeding powder, of course. No shift in the nozzle height was done for the remelting passes. Processing was resumed and followed through, however, regardless of the taken measure, irregular layers were still attained. Figure 35 depicts the final product of this attempt.

Figure 35 – Irregular layers achieved after overlay deposition of bead 44

Source: Author

From this result it was concluded that additionally to the defects caused by the lack of fusion between beads, there may have been another factor exerting a negative effect in processing. This factor could well be the powder flow instabilities detected in the photogrammetric measurements, however, in order to be certain, another overlaid deposition aiming for absence of defects caused by lack of fusion had to be done. Now, with an unused substrate, and since process speed was already capped at the minimal tested value, the simplest way to increase the amount of fused material was to increase laser power from parameter 44. This led to parameter set 78, which has its characteristics described at Table 6.

Table 6 – Parameters and quantities of the replacement parameter set

ID	**$\dot{m}$ (g/min)**	**P_L (W)**	**V (mm/min)**	**w (mm)**	**h (mm)**	**h' (mm)**	**A_{dep} (mm²)**	**d (%)**
78	5.5	920	300	3.12	0.75	0.58	1.66	42

Source: Author

Modelling was redone for the new inputs, resulting in the same bead and layer count but a slightly lower nozzle Z-step of 0.672 mm. Remelting passes were done with process parameters matching parameter set 78. The result of the second and final attempt to evenly deposit overlaid beads is show at Figure 36.

Figure 36 – Irregular deposition achieved after overlay deposition of bead 78

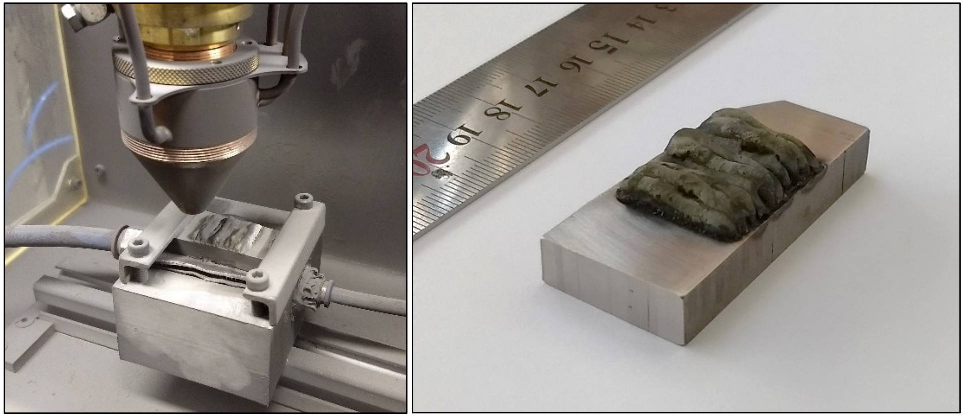

Source: Author

Although the deposition was higher than the former, its topology was severely uneven. After the two attempts, it became clear that the source for the small powder flow instabilities should be identified to allow its correction in future experiments. No further DED-L processing was possible due to time and substrate availability, therefore, investigations were done from data already available. Being the active photogrammetry measurement the actual imprint of this process behaviour regarding stability, its data was re-analysed with a focus on identifying the cause of the problem.

Each parameters set height standard deviation (S_h) and deposition area standard deviation (S_A) are a representation of how much bead dimensions oscillated during processing. This was already assumed when the 350 W beads were deemed useless, however, standard deviation values were then not correlated to power flow. By doing such, an interesting result was found, which is evidenced when adding the average of all parameters set's standard deviation for a given value of ṁ to its own standard deviation and analysing the results for the three ṁ values tested. The mathematical expressions for the described in the previous sentence, or in other words, for the stability factors of height (O_h) and deposition area (O_A), are demonstrated at Equation (15) and (16).

$$O_h = \left(\frac{(\sum_{i=1}^{n} S_h)}{n}\right) + \left(\sqrt{\frac{\sum_{i=1}^{n}(S_h - \overline{S_h})^2}{(n-1)}}\right) \tag{15}$$

$$O_A = \left(\frac{(\sum_{i=1}^{n} S_A)}{n}\right) + \left(\sqrt{\frac{\sum_{i=1}^{n}(S_A - \overline{S_A})^2}{(n-1)}}\right) \tag{16}$$

The results at Table 7 are calculated by applying these equations to the photogrammetric data.

Table 7 – Height and Area stability factors relation with powder flow rate

	O_h (mm)	O_A (mm²)
2,5 g/min	0,09	0.13
4,0 g/min	0,13	0.17
5,5 g/min	0,15	0.18

Source: Author

From Table 7 is deductible that with higher powder flows, oscillations in bead dimensions increase. Equivalent analyses were done with laser power and processing speed, however, only powder flow showed consistent influence over the stability factors. This suggests a new first criterion for parameter selection when attempting to process with a low-flowability powder such as the one used, however, since this hypothesis should be tested in actual DED-L processing, it stays only as a suggestion for further works. Nonetheless, considering that small beads are also more prone to be evened out by remelting, using a lower powder feed could be a solution for the problems faced in this final DED-L phase. Adding this new criterion to the other criteria would lead to selection of parameter set number 64, instead of the parameters sets tested. Parameters set number 64's properties are described at Table 8.

Table 8 – Candidate parameter set for future experiments; lower powder flow rate

ID	$\dot{m}$ (g/min)	P_L (W)	V (mm/min)	w (mm)	h (mm)	h' (mm)	A_{dep} (mm²)	d (%)
64	2.5	540	300	2.65	0.39	0.65	3.23	42

Source: Author

As for the reason why powder flow is influencing process instability, one can only hypothesise that the powder used does not flow from the disk continuously to the nozzle, especially when considering time periods shorter than the ones used for measuring powder flow described at Section 3.2.2.

4.6 Microstructural Analysis

The depositions made, although no long relatable to the parameters over which they were based, were still MMCs manufactured by DED-L therefore, their microstructure was produced in conditions which were ought to be controlled if more time for process parametrization would be available. Considering this, microstructural analysis was performed in the topologically defective samples, as it would still show characteristics from this MMC which are possible to be reproduced.

In counterpart, single bead tests were stable and broad enough to guarantee that trends in microstructure behaviour would be fully representative of this material's response to

DED-L. However, only one thing should be kept in mind, beads have dilution, thus, their volumetric percentage of TiC is different from one to the other, which should lead to changes in grain nucleation and TiC dissolution.

4.6.1 Overall Microstructure

Previous to heat treatment, the beads presented microstructure resultant mainly from columnar-epitaxial dendritic and equiaxed-dendritic solidification modes. Cellular solidification was also identifiable in some conditions. The ratio in which this solidification modes were seen was more relatable to bead dimensions than to process parameters. Although this ratio was not quantified, since etching was not calibrated for untreated samples; it was clear that the larger the bead, the smaller was the ratio between equiaxed-dendritic and columnar-dendritic solidification modes. Examples of the microstructure resultant from these solidification modes in a bead presenting them can be seen in the micrograph of non-heat treated sample depicted in Figure 37.

Figure 37 – Most present solidification modes in DED-L beads. On bead 39, here exposed as an example, the parameters were 540 W, 300 mm·min^{-1} and 5.5 g·min^{-1}, respectively to P_L, V and $\dot{m}$.

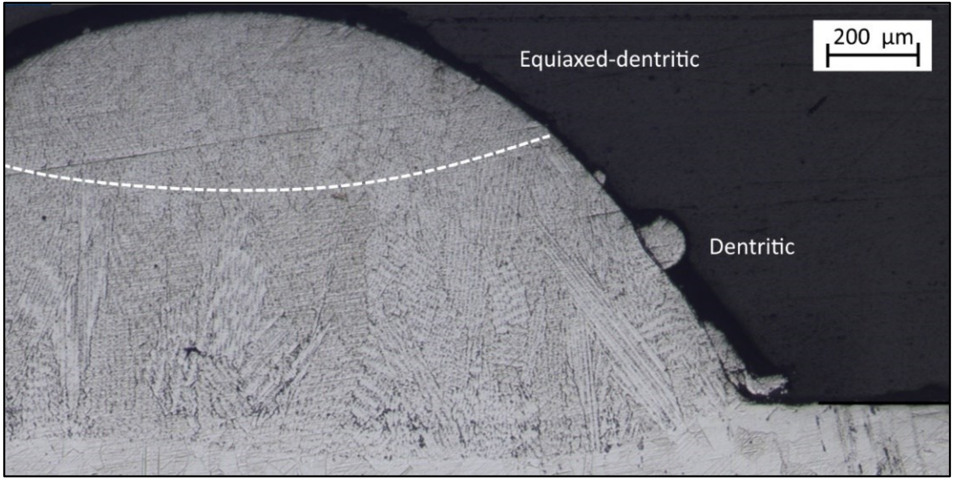

Source: Author

The majority of beads presented elongated grains aligned from the bead fusion line to where the laser heat source was acting, thus, mostly aligned upwards with the thermal gradient, as shown in Figure 37. These conditions caused mainly columnar-dendritic solidification, which gave the elongated shape to most of the grains. Grain size also changed perceptively from untreated samples to heat treated ones, which is naturally expected due to coalescence of similarly oriented grains, although the grains in the DED-L beads showed a considerably smaller grain size that the ones from the hot-rolled substrate. This alone can be considered an indication that mechanical properties were enhanced.

Titanium carbide particles were seemingly evenly distributed along each bead's volume, as no visible agglomeration or change in dispersion was detectable by the techniques used. Observation through optical, Figure 38.a, and electron microscopy, Figure 38.b, showed even distribution of carbides, except for small increase of their occurrence in grain boundaries, which due to carbide size and composition measurement was identified not to be exclusively the reinforcement particles added, but carbides that inherently form during solidification of Inconel X750. This dispersion of TiC particles is remarkable considering the density difference which this carbide has with the matrix, and especially since the particles lodged themselves inside of grains.

Figure 38 – OM (a) and SEM (b) micrographs of heat-treated samples showing $TiC_{p.}$ distribution on bead 44, which was considerably similar, if not equal, to the found in all other beads.

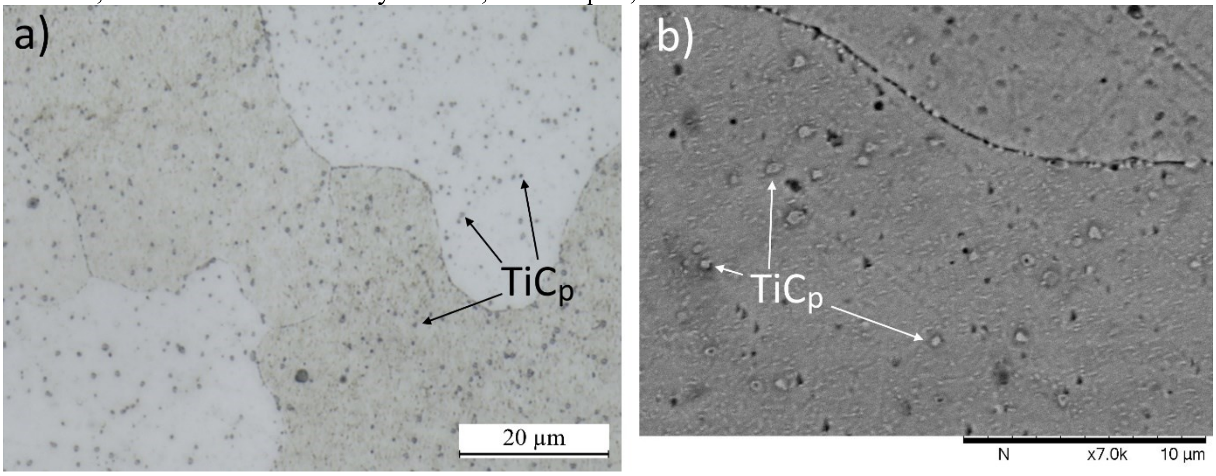

Source: Author

Carbides lodged within the crystalline lattice of grains are barrier to the movement of dislocations [6,50], and albeit creep resistance experiments or other bulk mechanical testing would be necessary to prove it, they are likely to enhance mechanical properties. In counterpart to when an excessive amount of these particles agglomerate exclusively in grain boundaries, were they are prone to severely impair traction creep resistance by serving as crack nucleators. However, being the case where they are dispersed in an evenly manner such as here, they will not do so, exerting only dislocations retainment while still reducing material density.

As a note, only for further reference, Vickers microhardness was measured. Heat-treated substrate microhardness was quantified as 376 ± 22 $HV_{0.1}$, while heat-treated DED-L bead number 44 microhardness was 390 ± 32 $HV_{0.1}$, both measurements were made in a Shimadzu HMV-2T E micro hardness tester. Ten seconds of loading time were used per measurement with an applied load of 980.7 mN.

4.6.2 Titanium carbide dissolution and surroundings

Differences in the chemical composition of the MMC`s matrix were not detected by SEM-EDS when comparing the overlaid samples with the Inconel X750 powder chemical composition, as shown in Table 9.

Table 9 – Matrix and powder Inconel X-750 chemical composition measured by EDS-SEM

Wt (%)	**Ni**	**Cr**	**Fe**	**Ti**	**Al**	**Nb**	**Mg**	**Si**	**S**	**Cu**	**C**	**Co**
Powder	72.3	15.6	6.6	3.0	0.9	0.9	0.2	0.2	-	-	-	-
Matrix	72.8	15.6	6.6	2.9	0.8	0.8	0.1	0.4	-	-	-	-

Source: Author

In a scenario were the carbide diluted into the matrix, it would be expected that a raise in titanium content would be detected, which was not. However, these EDS measurements were done distanced from the TiC particles in order to not be influenced by them. The smallest detection volume in the lower resolution microscope was too large for a measurement close to carbides, as shown by Figure 39.

Figure 39 – Micrograph of heat-treated bead section showing the EDS interaction area for the lower amplification SEM.

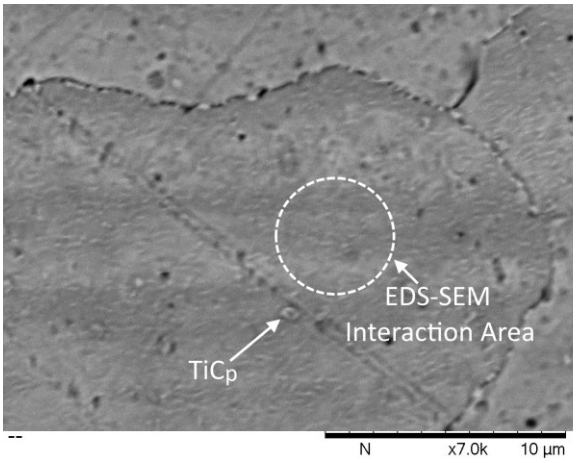

Source: Author

Therefore, dissolution was just not as intense as expected, but TiC particles could still have influenced the immediate region around them. When checking their chemical composition, still with the lower resolution microscope, an interesting result was found. All reinforcement particles point-EDS analyses showed Niobium content higher than expected, being this true for both heat-treated and untreated samples, Figure 40.

Figure 40 – Point EDS-SEM detection of Nb around TiC$_p$.

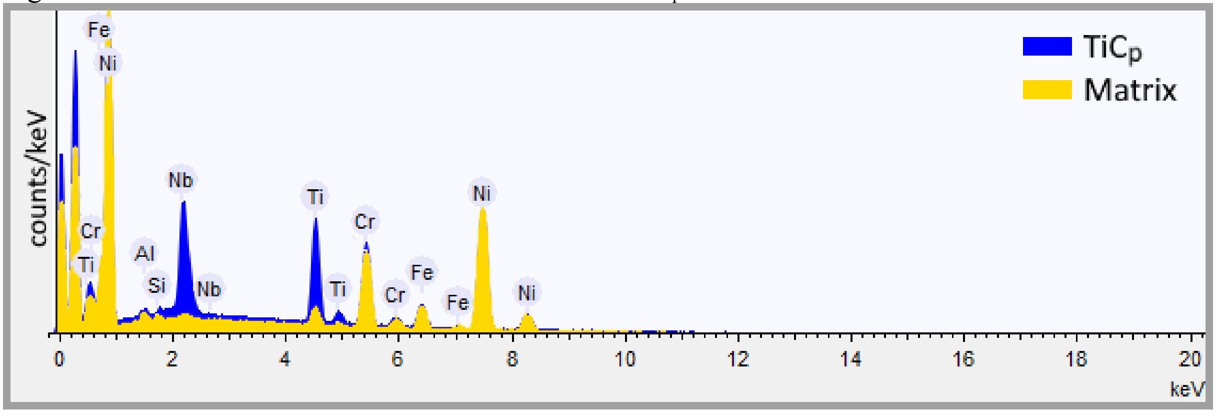

Source: Author

This indicated that Nb had reacted to TiC$_p$s presence already during solidification, precipitating around them. Since the microscope initially used did not had the resolution required to further study this phenomenon, the analysis was redone in a FEG-SEM to attempt to better characterize it. Some of the FEG-SEM-EDS analyses done, which now could be line scans instead of punctual acquisitions, are depicted at Figure 41 (heat treated sample) and at Figure 42 (untreated sample).

Figure 41 – FEG-SEM-EDS line scan over TiC particles from heat-treated bead. The bead used here for exemplification was produced with 920 W, 1000 mm·min^{-1} and 5.5 g·min^{-1}, being these values respective to P_L, V and $\dot{m}$.

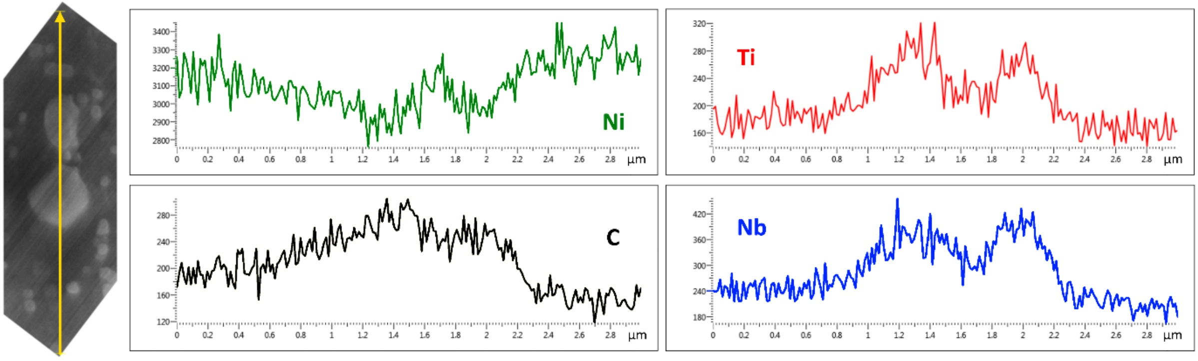

Source: Author

Niobium was again detected in all instances where the TiC particles were probed, however, increase in its occurrence was only detected when scanning over the particles and in an approximately 0.20 µm radius around them. Considering these SEM-EDS results and similar cases met in the literature [5,8], it is reasonable to assume that Nb was gathered over the TiC particles, forming Laves phases when in the matrix, or (Nb,Ti)C or NbC when adjacent to TiC particles. These affirmations were partially supported by XRD analyses which are described ahead in Section 4.6.4.

Figure 42 – FEG-SEM-EDS line scan over TiC particles from an untreated bead. The bead tested here is the same from Figure 41.

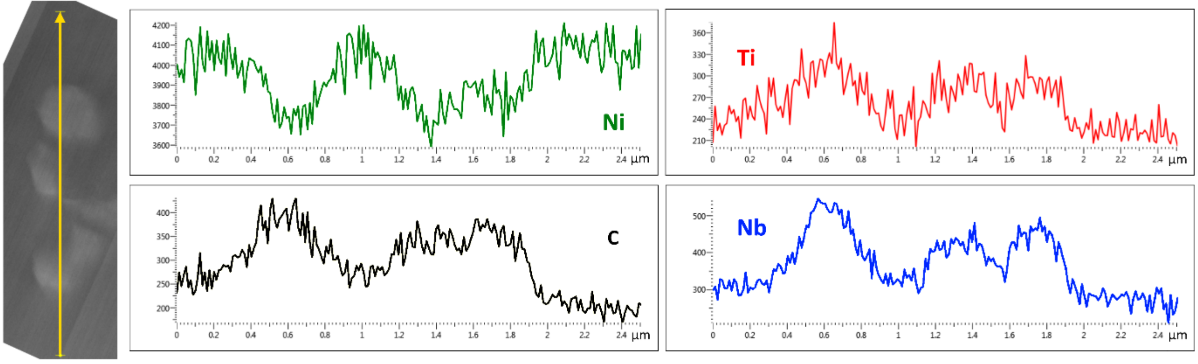

Source: Author

Transmission electron microscopy evidenced another response of the alloy to the TiC particles' presence. The gamma prime's primary precipitation was mostly absent in the TiC particles surroundings, which were filled by its secondary precipitation, as it may be behold at Figure 43 in the next page. This phenomenon may have occurred by the two following reasons, be them alone or as co-factors. The first, is the simple need of space adjacent to these particles for formation of large γ' precipitates, and the second is the existence of higher dislocation concentration around TiC$_{P}$ due to the punching effect, as described at sections 2.2 and 4.4. These reasonings are further explored ahead, however, it is necessary to justify why microsegregation was not considered a cause for the gamma prime absence around the TiCp.

As seen, the TiCp did not completely dissolve during solidification. Assuming the case that they likely acted as modifiers to the solidification conditions during DED-L, they would rather refine the dendritic solidification to happen around them instead of coarsening it. This would cause less microsegregation around the TiCp than in regions distant from them, and therefore, this lesser microsegregation would be more easily dispersed by the AMS 5668 standard dissolution heat treatment, and no heterogeneity in gamma prime precipitation would be seen. In fact, if one makes a parallel with the work of Lopez-Galilea *et al.* [38], it is possible to affirm that homogenization is faster and easier in DED-L manufactured materials than their wrought or cast counterparts. Thus, microsegregation was indeed not the cause for the localized concentration of secondary γ' precipitates and the absence of primary ones.

Figure 43 – TEM of DED-L manufactured MMC presenting γ’ precipitation behaviour around TiC_p.

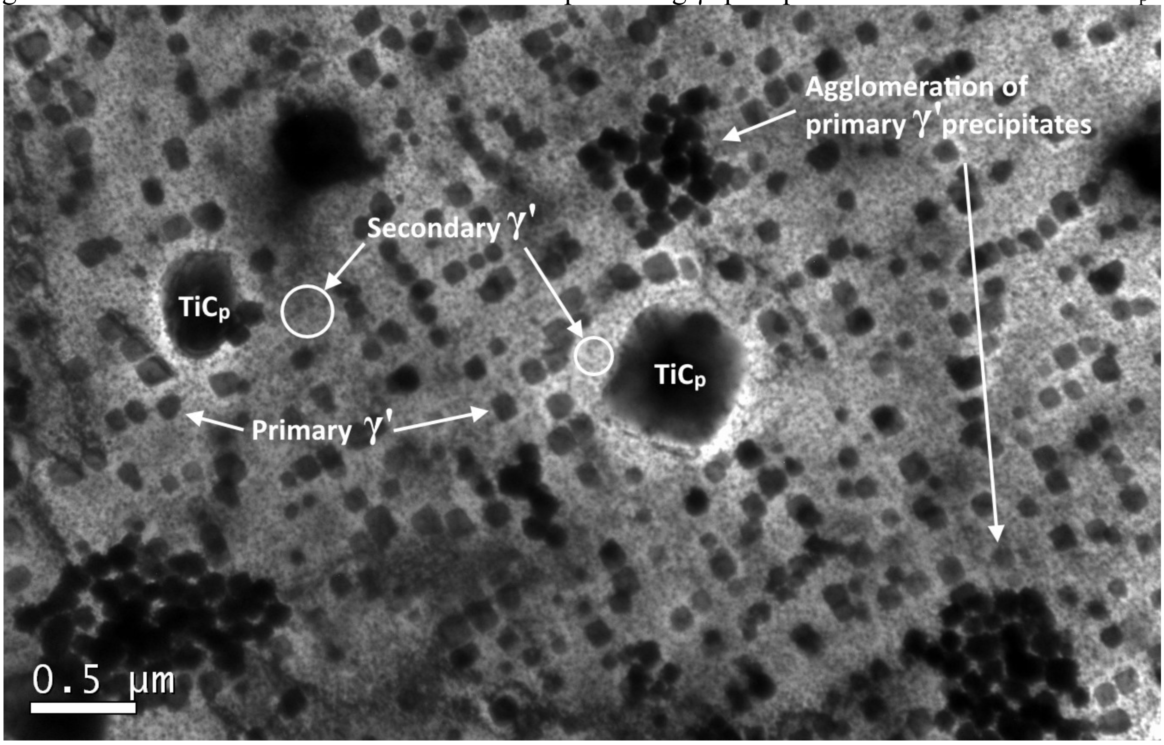

Source: Author

4.6.3 Gamma Prime

Since currently the heat-treated hot-rolled substrate is the material used to manufacture several components for actual applications, it was taken as reference to compare gamma prime formation in the DED-L overlaid samples. At Figure 44, representative bright field transmission electron microscopies from the substrate are depicted in the tandem with ones taken from the MMC.

Figure 44 – Comparison between primary γ’ precipitation in wrought Inconel X750 (a) and MMC (b).

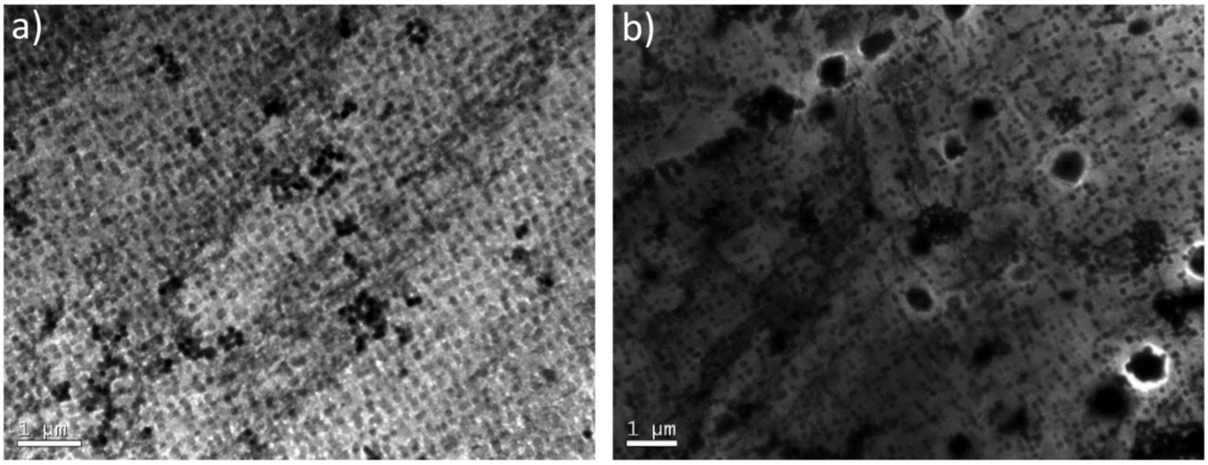

Source: Author

Figure 44 – Comparison between primary γ’ precipitation in wrought Inconel X750 (c) and MMC (d). Higher Amplification.

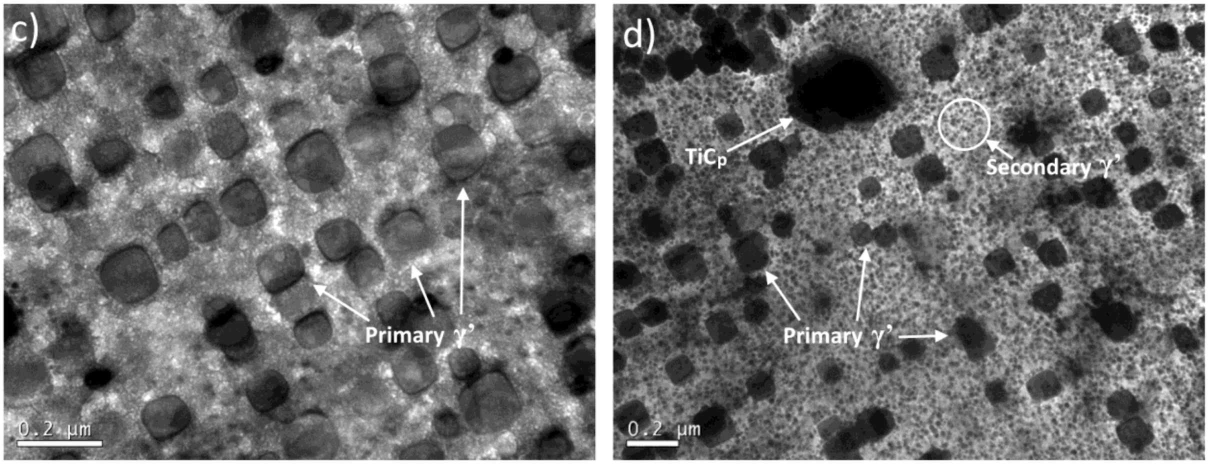

Source: Author

The hot-rolled material and the MMC had primary γ’ precipitates with practically equivalent shape and size, as all presented cuboidal shape, being their cuboid’s sides length measured as 99 ± 20 µm and 103 ± 20, respectively. The quantity of primary γ’ precipitates, however, was greater in the hot-rolled material than in the MMC, where they also were more evenly dispersed. This last fact is not due only to overall dispersion, as clustering of primary precipitates occurred more intensely in the MMC, phenomenon which was analysed no further.

Regarding γ’ volumetric fraction little can be said from the images, once that the considerably more intense secondary γ’ precipitation in the MMC may have compensated for this material’s lower amount of primary precipitates. This is easily seen between Figure 44.c and Figure 44.d. XRD analyses, refined by Rietveld’s technique, could make this comparison with precision, however, this stays as suggestion for further works.

Nonetheless, the morphology and size of the secondary γ’ precipitates could still be compared between the materials. Figure 45, shows close ups of this microstructure for each of them. Be aware that unfortunately the scales from the micrographs from Figure 45 in specific are different from one another. Secondary γ’ precipitates presented rounded shapes tending to cuboids in both materials but were slightly larger and considerably more scarce in the hot rolled substrate averaging in diameter around 13 ± 2 nm, while 9 ± 3 nm for the DED-L manufactured MMC.

Figure 45 – Comparison between secondary γ’ in wrought Inconel X750 (c) and MMC (d).

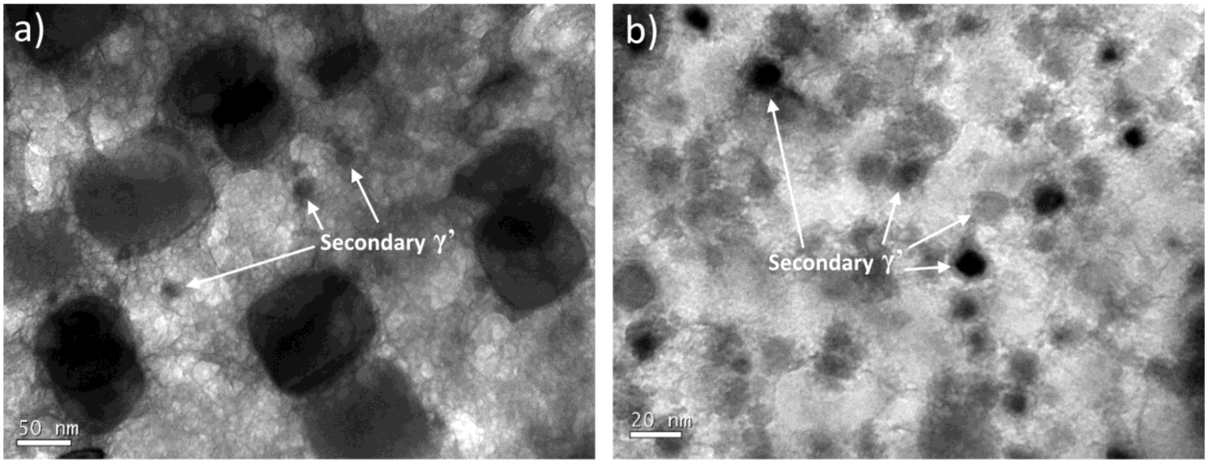

Source: Author

There is certainty that the microstructures referred to as secondary γ’ precipitation are indeed such, since in dark field imaging with the dislocated small aperture normally used for SAD, both primary and secondary precipitates shone together with the material`s primary precipitates. In other words, this represents that they have the same diffraction pattern, meaning the same crystalline structure and atomic spacing. At Figure 46, two dark field images from the same region than the one shown at Figure 44.d are exposed. Figure 46.a, was done by shifting aperture, as described, while the other, Figure 46.b, was attained by shifting the electron beam. Both technics obtain the same result, but with different image qualities.

Figure 46 – TEM dark field imaging of MMC. Bright regions prove identity of secondary γ’.

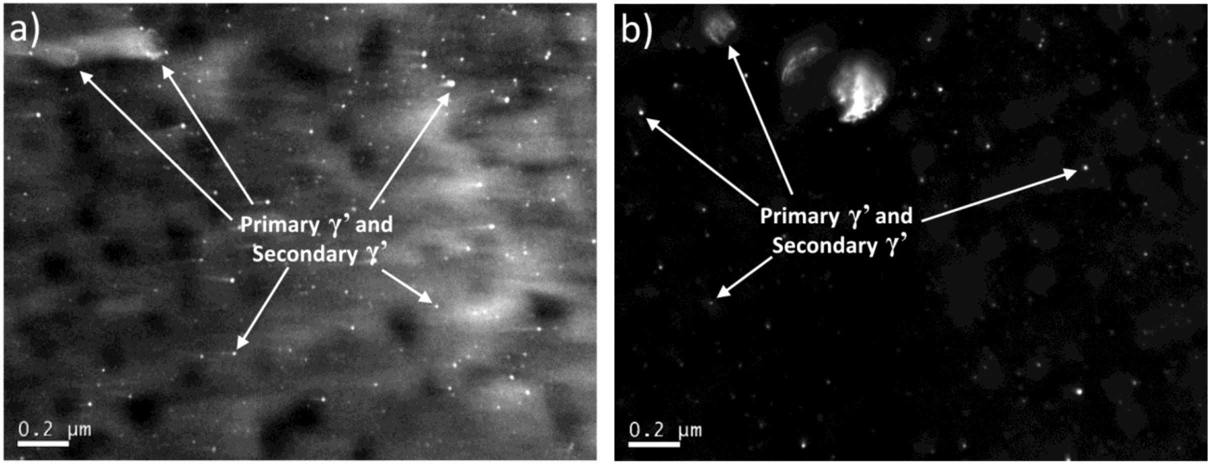

Source: Author

FEG-SEM was not exclusively used to analyse the TiC carbides, it was also used to observe the γ’ precipitates formed near grain boundaries, which could not be seen clearly through TEM since electrochemical polishing preferentially reacted with these regions. In Figure 47, a micrograph taken from a triple point gives a good representation of the results found in all three beads analysed by this technique. TiC particles can be seen inside of grains and, when in grain boundaries, can be differentiated due to their size and shape from other carbides inherent from the Inconel X750 matrix. Gamma prime precipitates show their characteristic behaviour of being aligned to the crystalline lattice, and since each grain has a different orientation, precipitate orientation also differs from one grain to the other. No additional observation regarding carbide morphology was needed, as TEM and SEM presented equivalent results.

Figure 47 – FEG-SEM imaging of triple point showing carbide distribution and γ’ orientation. The heat-treated bead here represented was produced under following conditions, 540 W, 440 mm·min^{-1} and 4 g·min^{-1}, being these values respective to P_L, V and $\dot{m}$.

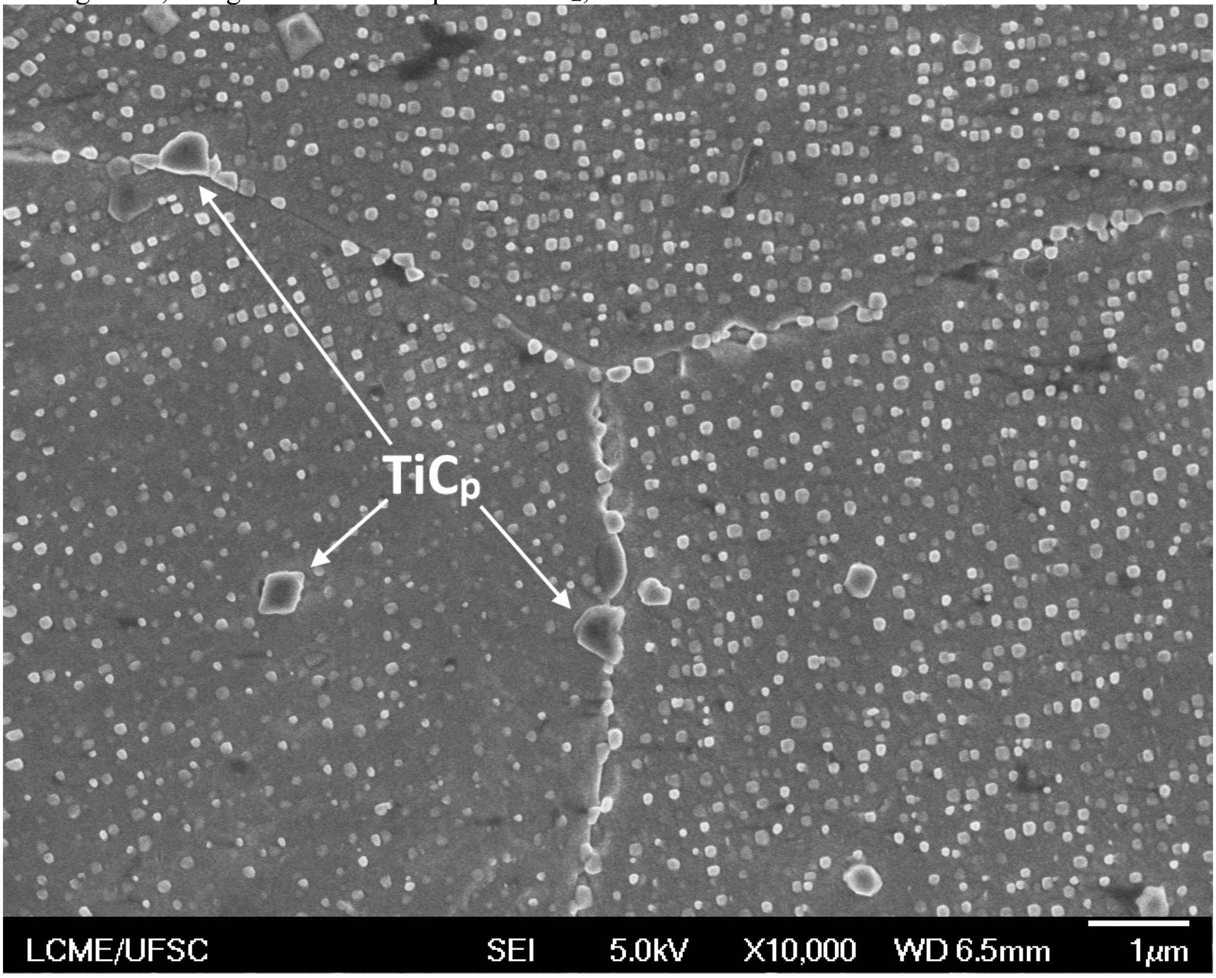

Source: Author

Differently from TEM, SEM analyses not a volume but a surface, therefore, γ’ precipitates seem to be less present in certain grains, as perceivable in the lower-left grain from Figure 47. This is but an impression given by preferential etching due the γ’ precipitates` different orientation. Although, primary γ’ precipitation was indeed less present in grain boundaries than it was along the grains’ volume, albeit its secondary precipitation reached the grains very edges, as presented in Figure 48. It was not expected that secondary gamma prime could be seen with the given metallographic preparation by FEG-SEM, this alone also stays as contribution for further works.

Figure 48 – FEG-SEM imaging of MMC showing carbide and γ' distribution at grain boundaries. The bead analysed here is the same from Figure 41.

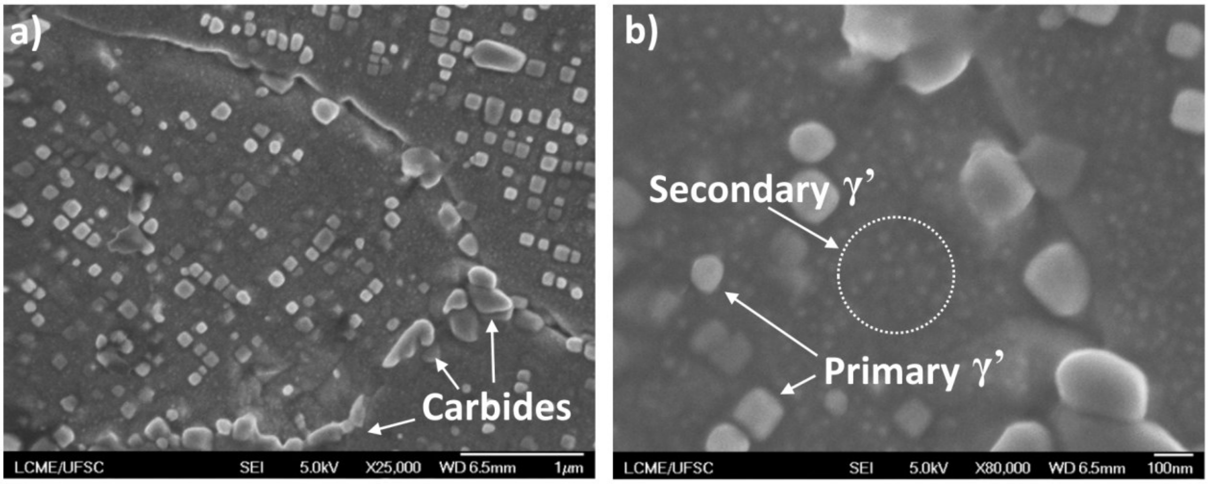

Source: Author

The presence of γ' precipitates in grain boundaries is important to the material's resistance to creep, since their absence may induce even greater stress concentration at grain boundaries by localized material softening. Their occurrence in these regions is also useful to difficult grain boundary movement, hinder coble creep, and inhibit dislocation movement [52,90].

4.6.4 X-Ray Diffractometry

X-Ray diffraction results allowed to infer over the identity of Niobium compounds which formed over the TiC particles and detect other phases present in the material. However, due to reduced sample size and thickness, and limited access to reference spectrum databases, not all diffraction peaks were possible to be identified. The only diffraction pattern taken is shown at Figure 49, it is referent to a sample in preparation for TEM analysis with three millimetres in diameter and 0.8 mm in thickness.

Figure 49 – XRD pattern of the TEM sample extracted from the last deposition after heat treatment.

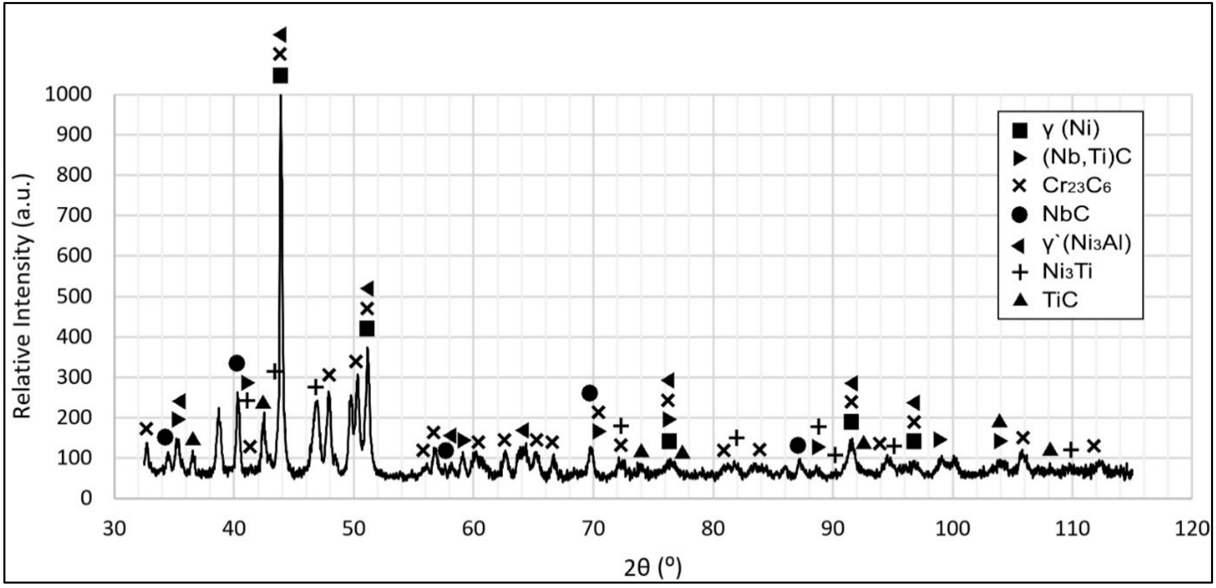

Source: Author

All the indexed phases have been reported by other authors in analysing equivalent materials [8,9], the missing major peaks respective to double theta equal to 38.6°, 49.8° and 100.3° were not relatable to substances possible to be found in this material and also listed in the available spectra database.

No Laves phases were detectable, as expected due to data quality, but both (Nb,Ti)C and NbC diffraction patterns were recognized and, thus, the theory that Nb reacted partially to the added TiC particles and formed these compounds was supported. The precise effect in mechanical properties caused by this needs to be further explored, as Nb depletion from γ' precipitates may reduce their tensile strength [52], whilst Nb-related carbides formation may stabilize TiC particles or increase their bond with the matrix.

Gamma prime's volume fraction was not quantifiable due to data quality, but its presence and gamma phase's were easily detected. The carbides found in grain boundaries seem to be in part Cr23C6, being this result similar to the one Lemos et al. [8] and expected from Inconel X750 [63,64]. Titanium carbide was also detected, concluding that the reinforcement particles' inner volume was not chemically altered by reactions with niobium.

The η phase was only detected by XRD, which is surprising, due to the relatively high intensity of its diffraction peaks, it would be reasonable to assume that microscopy should have been able to detect it. A recommendation stays here to perform the XRD analysis of larger samples and use more complete databases for spectrum comparison, before moving to conclusions over the amount of η phase present.

5 CONCLUSION

The new powder feeder silo with the steeper inner angle was ineffective in providing flow, and powder had to be intermittently supplied to the powder feeder metering system. Powder feed rate measurements at the DED-L nozzle outlet confirmed a consistent linear relation ($R^2 = 0.99$) between powder feed rate and the revolutions per minute of the feeder's disk, but this measurement method's relatively large acquisition periods hid minor powder flow oscillations, which were seen only after processing, and then considered deleterious to the manufacture of higher depositions through overlapping. Nonetheless, DED-L of the TiC_p-reinforced Inconel X750 MMC was made possible to a certain extent regardless the low flowability observed for the powder mixture.

Two methods to analyse process stability were devised based on active photogrammetry of DED-L beads. Measurement through photogrammetry was seen imprecise for bead width but was proven remarkably useful in measuring bead height and deposition area, and thus, to analyse process stability. The first method was based on comparison of individual bead height standard deviation with the overall bead height standard deviation. The comparison proved that a minimal value of 70 $J.mm^{-1}$ is required for processing in the tested conditions, establishing a lower boundary for process parameters. The second method used to analyse process stability was again a comparison, but between what it was then called stability factors (O_h and O_A). Their results indicated that lower powder feed rates are likely to increase process stability, contradicting the usually found in literature when refereeing to flow behaviour of bulk solids, but only indicating this powder just as an exception to the rule when processed under the conditions described.

Despite the difficulties met in processing such fine-powdered bulk solid, enough consistency in deposition was achieved to allow the evaluation of MMC microstructure and the relation between process parameters and deposition quantities. All relations met here followed what is described in the literature, being bead height, bead dilution, deposition rate, and deposition area strongly dependent of powder feed rate, while powder efficiency and bead width not. Laser power and scan speed had different effects to each listed parameter, being such described in the text's body.

Several techniques were used to analyse the microstructure of both single beads and the overlapped depositions. Sample analysis after and before heat treatment was essential to understand the formation of the MMC's final microstructure. The metallographic etching optimized and described here made possible to analyse gamma prime's secondary precipitation through FEG-SEM, which is usually done only with TEM. The XRD analysis done was impaired due to sample dimensions and lack of access to diffraction databases, however, it still enabled qualitative characterization of the major Inconel X750 constituents in the MMC, the TiC added, and the Nb compounds formed during DED-L processing. These results, together with FEG-SEM-EDS scans, indicated that Niobium reacted with TiC_p during solidification, likely forming NbC and/or (Nb,Ti)C around the reinforcement particles. If these Nb compounds' properties similarities with TiC are disregarded, one may assume that the observed TiC particles may have suffered degradation, however, Nb-compound formation was minimal, being only approximately 20 nm thick around the particles. The matrix chemical composition remained nominally equivalent to the one from Inconel X750, reinforcing the evidence that the degradation suffered by the particles captured during deposition may be of likely insignificance when this MMC follows for future thermo-mechanical testing.

The most characteristic reinforcement phase of Ni-base superalloys, the gamma prime precipitates, showed high levels of occurrence in both the MMC`s matrix and the hot-rolled Inconel X750 substrate. This phase's volumetric ratio in relation to the gamma phase, and its cuboidal morphology were seemingly similar between materials, however, gamma prime's precipitate size and size distribution did not follow the pattern. This phase primary precipitates were of equivalent size from MMC to hot-rolled material, being around 101 nm in width, but considerably more present in the hot-rolled material; while its secondary precipitates were slightly smaller in the MMC, from 13 nm to 9 nm in width, being also more abundant in it.

TiC particles were evenly distributed along the MMC, being present inside grains and at grain boundaries. They may, therefore, exert positive influence in two reinforcement mechanisms, like the anchoring of dislocations and the restriction of grain boundary slippage. Another interesting microstructural characteristic was caused by the inclusion of $TiC_{p.}$ Their surroundings were mostly absent of primary γ` precipitates but filled with their secondary precipitation. Although the exact effect of this requires mechanical testing and posterior fracture analysis, it was evidenced that a larger presence of dislocations is likely be located around these particles. The cause of this dislocation concentration would be the thermal coefficient misfit between matrix and reinforcement particulate, while the evidences for their concentration are the detected dislocation etching phenomenon around TiC_p and the likely high nucleation of the secondary gamma prime precipitates from the dislocations themselves.

No major defect or material degradation occurred which could be used to discard further mechanical testing or the possibility of processing this MMC composition by DED-L. Only hardness was measured here, being slightly higher for the MMC than that of the pure alloy. Below the four main conclusions taken from this work are reiterated and organized in a list for clarity's sake:

a) The chemical composition chosen for the MMC is promising as it did not presented defects that could evidently hinder further research or impede this composition's plausibility of application;

b) Two methods based in active photogrammetry were devised to analyse process stability through measurements of individual beads were proven effective;

c) The Inconel X750 and titanium carbide powder mixture characterized here, presented low flowability, requiring system improvements or changes in flow-related characteristics to allow lengthy DED-L processing;

d) Secondary gamma prime concentration around titanium carbide particles and the dislocation etching found around the same indicate large concentration of dislocation around the reinforcement particles even after AMS 5668 heat-treatment.

6 SUGGESTIONS FOR FURTHER WORKS

Since DED-L operation at 2.5 g/min will restrict applications and the scope of future researches, the development of a powder feeder which allows processing low-flowability powders at higher rates, like the one used here, stay as suggestion for further works. Some promising system designs are listed in the literature review, but another likely solution, that would not require the complete replacement of the powder feeding system, is the addition of a rod linearly oscillating through the exhaust hopper in a direction coincident to the powder silo axis. The rod would push the powder into the disk`s notch by breaking the bonds between the powder particles which are forming an arc-like structure over the silo's exit, likely solving the problem for the current case and others.

The coherence between literature and results regarding deposition behaviour shows that the MMC powder will behave as required by DED-L once the powder flow problem is solved. As suggestion for further works also stays the modelling of these relations to allow the deposition of higher volumes and more complex shapes as well as easing the automate control of deposition, thus, creating a considerably more robust system.

In further works, it would be most interesting to study the use of XRD-related technics to quantify the MMC's and the hot-rolled Inconel X750's gamma-gamma prime volumetric ratios, while also measuring the amount of Nb-compounds and the gamma prime clustering in the MMC, thus allowing correlation between these quantities to different DED-L processing conditions and heat treatments. The quantification of the MMC's gamma prime volumetric percentage could also be attempted through image analysis, weighting after gamma phase solubilization, or other. Complementary to theses evaluations, equivalent measurements of DED-L manufactured Inconel X750 are also recommended, since they would allow to isolate the effects of DED-L processing from the inclusion of the titanium carbide particulate. For example, this would allow to identify which portion of the grain refinement presented in this work is due to crystal nucleation from the carbides and which is due to the rapid cooling provided by laser processing.

Lastly, once the powder flowability issues have been solved, larger samples could be manufactured and, thus, a thorough mechanical evaluation would be recommended for further works. An interesting property to analyse would be the resistance to traction creep, if this property presents itself equivalent or higher in the MMC than in the raw alloy, gains in component lifetime could then have been already achieved, since the density reduction attained by the addition of the titanium carbide particulate would reduce one of the stress components present in turbine blades under operation, the imposed centrifugal forces.

BIBLIOGRAPHY

[1] MIRACLE, D.B. **Metal matrix composites - From science to technological significance**, Composites Science and Technology. Vol. 65 pp. 2526–2540 (2005). https://doi.org/10.1016/j.compscitech.2005.05.027.

[2] WANG, Y.; SHI, J.; WANG, X.; WANG, Y. **In Situ AFM Characterization of Deformation Behavior of Nano TiC Reinforced Inconel 718 Superalloy Prepared by Selective Laser Melting**, Volume 2B: Advanced Manufacturing. pp. V02BT02A046 (2015). https://doi.org/10.1115/IMECE2015-52426.

[3] BI, G.; SUN, C.N.; NAI, M.L.; WEI, J. **Micro-structure and mechanical properties of nano-TiC reinforced Inconel 625 deposited using LAAM**, Physics Procedia. Vol. 41 pp. 828–834 (2013). https://doi.org/10.1016/j.phpro.2013.03.155.

[4] HONG, C.; GU, D.; DAI, D.; ALKHAYAT, M.; URBAN, W.; YUAN, P.; CAO, S.; GASSER, A.; WEISHEIT, A.; KELBASSA, I.; ZHONG, M.; POPRAWE, R. **Laser additive manufacturing of ultrafine TiC particle reinforced Inconel 625 based composite parts: Tailored microstructures and enhanced performance**, Materials Science and Engineering A. Vol. 635 pp. 118–128 (2015). https://doi.org/10.1016/j.msea.2015.03.043.

[5] XU, X.; MI, G.; XIONG, L.; JIANG, P.; SHAO, X.; WANG, C. **Morphologies, microstructures and properties of TiC particle reinforced Inconel 625 coatings obtained by laser cladding with wire**, Journal of Alloys and Compounds. Vol. 740 pp. 16–27 (2018). https://doi.org/10.1016/j.jallcom.2017.12.298.

[6] CHAWLA, N.; SHEN, Y.-L. **Mechanical Behavior of Particle Reinforced Metal Matrix Composites**, Advanced Engineering Materials. Vol. 3 pp. 357–370 (2001). https://doi.org/10.1002/1527-2648(200106)3:6<357::AID-ADEM357>3.0.CO;2-I.

[7] CHAWLA, K.K. **Metal Matrix Composites**, in: Materials Science and Technology, Wiley-VCH Verlag GmbH & Co. KGaA, Weinheim, Germany, 2006. https://doi.org/10.1002/9783527603978.mst0150.

[8] LEMOS, G.; FREDEL, M.C.; PYCZAK, F.; TETZLAFF, U. **Development of a TiC_p Reinforced Ni-base Superalloy MMC, with High Creep Resistance and Reduced Weight**, Key Engineering Materials. Vol. 742 pp. 189–196 (2017). https://doi.org/10.4028/www.scientific.net/KEM.742.189.

[9] LEMOS, G.; FREDEL, M.C.; PYCZAK, F.; TETZLAFF, U. **Influence of Distinct Manufacturing Processes on the Microstructure of Ni-base Metal Matrix**

Composites Submitted to Long Thermal Exposure, Key Engineering Materials. Vol. 809 pp. 79–86 (2019). https://doi.org/10.4028/www.scientific.net/KEM.809.79.

[10] SOUSA, J.M.S. **Análise das propriedades tribológicas de revestimentos de Ni-Cr-B-Si depositados via laser cladding a pó**, Universidade Federal de Santa Catarina, POSMEC, 2019, pp. 1–123.

[11] SOUSA, J.; DE SOUZA PINTO PEREIRA, A.; SILVA, R.G.N.; AMARAL, C.; PEREIRA, M. **Tribological evaluation of Ni-Cr-B-Si coatings deposited by laser metal deposition and treated by laser remelting**, in: Proceedings of the 25th International Congress of Mechanical Engineering, ABCM, 2019. https://doi.org/10.26678/ABCM.COBEM2019.COB2019-1489.

[12] DE SOUZA PINTO PEREIRA, A.; WEINGAERTNER, W.L.; PEREIRA, M.; GUTJAHR, J. **Laser Cladding a Pó de AISI 316L em Substrato de SAE 1020 para Proteção de Maquinário à Corrosão**, Anais Do IX Congresso Brasileiro de Engenharia de Fabricação. pp. 1–7 (2017). https://doi.org/10.26678/abcm.cobef2017.cof2017-0658.

[13] DE SOUZA PINTO PEREIRA, A.; WEINGAERTNER, W.L.; PEREIRA, M. **Laser Remelting as Mean to Reduce Clad Misorientated Volume Deposited throught Laser Cladding when Applied to Single Cristaline Turbine Blades**, in: Anais Do IX Congresso Brasileiro de Engenharia de Fabricação, ABCM, 2017. https://doi.org/10.26678/ABCM.COBEF2017.COF2017-0673.

[14] GUTJAHR, J. **Desenvolvimento e Implementação de um sistema CNC, Modular e Reconfigurável, para Processos LASER**, Universidade Federal de Santa Catarina, POSMEC, 2016, pp. 198.

[15] TOYSERKANI, E.; KHAJEPOUR, A.; CORBIN, S. **Laser Cladding**, 1st ed., CRC Press LLC, Boca Raton, Florida 33431, 2004, pp. 263.

[16] DASS, A.; MORIDI, A. **State of the art in directed energy deposition: From additive manufacturing to materials design**, Coatings. Vol. 9 (2019). https://doi.org/10.3390/COATINGS9070418.

[17] ASTM INTERNATIONAL. **F2792-12a - Standard Terminology for Additive Manufacturing Technologies**, 2013, pp. 10–12. https://doi.org/10.1520/F2792-12A.2.

[18] ASTM. **ASTM F3187 - 16: Standard Guide for Directed Energy Deposition of Metals**, (2016). https://doi.org/10.1520/F3187-16.

[19] ION, J.C.; ION, J.C. **Chapter 12 – Cladding**, Laser Processing of Engineering Materials. pp. 296–326 (2005). https://doi.org/10.1016/B978-075066079-2/50015-5.

[20] POPRAWE, R. **Tailored Light 2**, Springer Berlin Heidelberg, Berlin, Heidelberg, 2011,

pp. 605. https://doi.org/10.1007/978-3-642-01237-2.

[21] KAIERLE, S.; BARROI, A.; NOELKE, C.; HERMSDORF, J.; OVERMEYER, L.; HAFERKAMP, H. **Review on Laser Deposition Welding: From Micro to Macro**, Physics Procedia. Vol. 39 pp. 336–345 (2012). https://doi.org/10.1016/j.phpro.2012.10.046.

[22] KOU, S. **Welding Metallurgy**, John Wiley & Sons, Inc., Hoboken, NJ, USA, 2002, pp. 466. https://doi.org/10.1002/0471434027.

[23] ACHARYA, R.; BANSAL, R.; GAMBONE, J.J.; DAS, S. **A Coupled Thermal, Fluid Flow, and Solidification Model for the Processing of Single-Crystal Alloy CMSX-4 Through Scanning Laser Epitaxy for Turbine Engine Hot-Section Component Repair (Part I)**, Metallurgical and Materials Transactions B. Vol. 45 pp. 2247–2261 (2014). https://doi.org/10.1007/s11663-014-0117-9.

[24] CAIAZZO, F.; CAGGIANO, A. **Laser Direct Metal Deposition of 2024 Al Alloy: Trace Geometry Prediction via Machine Learning**, Materials. Vol. 11 pp. 444 (2018). https://doi.org/10.3390/ma11030444.

[25] THOMPSON, S.M.; BIAN, L.; SHAMSAEI, N.; YADOLLAHI, A. **An overview of Direct Laser Deposition for additive manufacturing; Part I: Transport phenomena, modeling and diagnostics**, Additive Manufacturing. Vol. 8 pp. 36–62 (2015). https://doi.org/10.1016/j.addma.2015.07.001.

[26] MA, M.; WANG, Z.; ZENG, X. **Effect of energy input on microstructural evolution of direct laser fabricated IN718 alloy**, Materials Characterization. Vol. 106 pp. 420–427 (2015). https://doi.org/10.1016/j.matchar.2015.06.027.

[27] MOKADEM, S.; BEZENÇON, C.; HAUERT, A.; JACOT, A.; KURZ, W. **Laser repair of superalloy single crystals with varying substrate orientations**, Metallurgical and Materials Transactions A: Physical Metallurgy and Materials Science. Vol. 38 A pp. 1500–1510 (2007). https://doi.org/10.1007/s11661-007-9172-z.

[28] GÄUMANN, M.; BEZENÇON, C.; CANALIS, P.; KURZ, W. **Single-crystal laser deposition of superalloys: Processing-microstructure maps**, Acta Materialia. Vol. 49 pp. 1051–1062 (2001). https://doi.org/10.1016/S1359-6454(00)00367-0.

[29] GÄUMANN, M.; TRIVEDI, R.; KURZ, W. **Nucleation ahead of the advancing interface in directional solidification**, Materials Science and Engineering: A. Vol. 226–228 pp. 763–769 (1997). https://doi.org/10.1016/S0921-5093(97)80081-0.

[30] SIVA PRASAD, H.; BRUECKNER, F.; KAPLAN, A.F.H. **Powder catchment in laser metal deposition**, Journal of Laser Applications. Vol. 31 pp. 022308 (2019). https://doi.org/10.2351/1.5096130.

[31] GANDIN, C.A.; RAPPAZ, M.; WEST, D.; ADA, B.L. **Grain texture evolution during the columnar growth of dendritic alloys**, Metallurgical and Materials Transactions A. Vol. 26 pp. 1543–1551 (1995). https://doi.org/10.1007/BF02647605.

[32] WOLFF, S.; LEE, T.; FAIERSON, E.; EHMANN, K.; CAO, J. **Anisotropic properties of directed energy deposition (DED)-processed Ti–6Al–4V**, Journal of Manufacturing Processes. Vol. 24 pp. 397–405 (2016). https://doi.org/10.1016/j.jmapro.2016.06.020.

[33] TURNBULL, D. **Kinetics of heterogeneous nucleation**, The Journal of Chemical Physics. Vol. 18 pp. 198–203 (1950). https://doi.org/doi:10.1063/1.1747588.

[34] SCHULZE, D. **Powders and Bulk Solids**, Springer Berlin Heidelberg, Berlin, Heidelberg, 2007, pp. 517. https://doi.org/10.1007/978-3-540-73768-1.

[35] LIU, Z.; ZHANG, H.C.; PENG, S.; KIM, H.; DU, D.; CONG, W. **Analytical modeling and experimental validation of powder stream distribution during direct energy deposition**, Additive Manufacturing. Vol. 30 pp. 100848 (2019). https://doi.org/10.1016/j.addma.2019.100848.

[36] ABIOYE, T.E.; FARAYIBI, P.K.; MCCARTNEY, D.G.; CLARE, A.T. **Effect of carbide dissolution on the corrosion performance of tungsten carbide reinforced Inconel 625 wire laser coating**, Journal of Materials Processing Technology. Vol. 231 pp. 89–99 (2016). https://doi.org/10.1016/j.jmatprotec.2015.12.023.

[37] COOPER, D.E.; BLUNDELL, N.; MAGGS, S.; GIBBONS, G.J. **Additive layer manufacture of Inconel 625 metal matrix composites, reinforcement material evaluation**, Journal of Materials Processing Technology. Vol. 213 pp. 2191–2200 (2013). https://doi.org/10.1016/j.jmatprotec.2013.06.021.

[38] LOPEZ-GALILEA, I.; RUTTERT, B.; HE, J.; HAMMERSCHMIDT, T.; DRAUTZ, R.; GAULT, B.; THEISEN, W. **Additive manufacturing of CMSX-4 Ni-base superalloy by selective laser melting: Influence of processing parameters and heat treatment**, Additive Manufacturing. Vol. 30 pp. 100874 (2019). https://doi.org/10.1016/j.addma.2019.100874.

[39] HÖGANÄS AB. **Thermal Surfacing Powder Choice With Ease**, pp. 1–12 (2017). https://www.hoganas.com/globalassets/media/sharepoint-documents/BrochuresanddatasheetsAllDocuments/Powder_choice_with_ease.pdf Accessed in: February 10, 2020.

[40] ALVES, J.A.; E SILVA, R.H.G.; DUTRA, J.C. **Development of a powder-feed device and procedures for the application of an experimental alloy in overhead PTA-P welding**, Soldagem e Inspecao. Vol. 20 pp. 412–422 (2015).

https://doi.org/10.1590/0104-9224/SI2004.08.

[41] PENG, Y.; ZHAO, K.; YANG, Y.; PU, H.; SUN, Y.; LIU, N.; LIU, Y.; XIE, S.; LUO, J. **Highly precise and efficient powder feeding system based on gravimetric feedback**, Powder Technology. Vol. 354 pp. 719–726 (2019). https://doi.org/10.1016/j.powtec.2019.06.043.

[42] SURI, A.; HORIO, M. **A novel cartridge type powder feeder**, Powder Technology. Vol. 189 pp. 497–507 (2009). https://doi.org/10.1016/j.powtec.2008.08.001.

[43] KUMAR, P.; SANTOSA, J.K.; BECK, E.; DAS, S. **Direct-write deposition of fine powders through miniature hopper-nozzles for multi-material solid freeform fabrication**, Rapid Prototyping Journal. Vol. 10 pp. 14–23 (2004). https://doi.org/10.1108/13552540410512499.

[44] HAGHSHENAS, M. **Metal–Matrix Composites**, Reference Module in Materials Science and Materials Engineering. pp. 1–28 (2016). https://doi.org/10.1016/b978-0-12-803581-8.03950-3.

[45] NISHIDA, Y. **Introduction to Metal Matrix Composites**, Springer Japan, Tokyo, 2013, pp. 1–16. https://doi.org/10.1007/978-4-431-54237-7.

[46] CHAWLA, N. **Metal Matrix Composites**, Kluwer Academic Publishers, Boston, 2006. https://doi.org/10.1007/b101197.

[47] IBRAHIM, I.A.; MOHAMED, F.A.; LAVERNIA, E.J. **Particulate reinforced metal matrix composites — a review**, Journal of Materials Science. Vol. 26 pp. 1137–1156 (1991). https://doi.org/10.1007/BF00544448.

[48] TAYA, M.; MORI, T. **Dislocation Punching From Ceramic/Metal Interfaces**, Journal of Engineering Materials and Technology. Vol. 116 pp. 408–413 (1994). https://doi.org/10.1115/1.2904306.

[49] SHIBATA, S.; TAYA, M.; MORI, T.; MURA, T. **Dislocation punching from spherical inclusions in a metal matrix composite**, Acta Metallurgica et Materialia. Vol. 40 pp. 3141–3148 (1992). https://doi.org/10.1016/0956-7151(92)90477-V.

[50] ABBASCHIAN, R.; ABBASCHIAN, L.; REED-HILL, R.E. **Phisical Metallurgy Principles**, Fourth, Cengage Learning, 2009.

[51] T. S. SRIVATSAN, YUZHENG ZHANG, W.C.H. **Metal-Matrix Composites Innovations, Advances and Applications**, Springer International Publishing, Cham, 2018. https://doi.org/10.1007/978-3-319-72853-7.

[52] DONACHIE, M.J.; DONACHIE, S.J. **Superalloys: A Technical Guide**, Superalloys: A Technical Guide. pp. 1–409 (2002).

[53] REED, R.C. **The Superalloys: Fundamentals and applications**, Cambridge University Press, Cambridge, 2006, pp. 1–390. https://doi.org/10.1017/CBO9780511541285.

[54] DRUAND-CHARRE, M. **The Microstructure of Superalloys**, CRC Press, 1997, pp. 1–124.

[55] HONG, C.; GU, D.; DAI, D.; GASSER, A.; WEISHEIT, A.; KELBASSA, I.; ZHONG, M.; POPRAWE, R. **Laser metal deposition of TiC / Inconel 718 composites with tailored interfacial microstructures**, Optics and Laser Technology. Vol. 54 pp. 98–109 (2013). https://doi.org/10.1016/j.optlastec.2013.05.011.

[56] CAO, S.; GU, D. **Laser metal deposition additive manufacturing of TiC/Inconel 625 nanocomposites: Relation of densification, microstructures and performance**, Journal of Materials Research. Vol. 30 pp. 3616–3628 (2015). https://doi.org/10.1557/jmr.2015.358.

[57] WILSON, J.M.; SHIN, Y.C. **Microstructure and wear properties of laser-deposited functionally graded Inconel 690 reinforced with TiC**, Surface and Coatings Technology. Vol. 207 pp. 517–522 (2012). https://doi.org/10.1016/j.surfcoat.2012.07.058.

[58] MEHER, S.; AAGESEN, L.K.; CARROLL, M.C.; POLLOCK, T.M.; CARROLL, L.J. **The origin and stability of nanostructural hierarchy in crystalline solids**, Science Advances. Vol. 4 pp. 1–11 (2018). https://doi.org/10.1126/sciadv.aao6051.

[59] ORUGANTI, R.; SHUKLA, A.; NALAWADE, S.; SARKAR, S.; SIVAKUMAR, K.G.V.; VISHWANATH, T.; SONDHI, S.; WESSMAN, A.; WEI, D.; POWELL, A.; BAIN, K.; SCHAEFFER, J.; PECK, A.; ARNETT, M.; SHASTRY, G.; MASTROMATTEO, F. **A microstructure-based model for creep of gamma prime strengthened nickel-based superalloys**, Journal of Engineering Materials and Technology, Transactions of the ASME. Vol. 141 pp. 1–6 (2019). https://doi.org/10.1115/1.4040554.

[60] BÜRGER, D.; PARSA, A.B.; RAMSPERGER, M.; KÖRNER, C.; EGGELER, G. **Creep properties of single crystal Ni-base superalloys (SX): A comparison between conventionally cast and additive manufactured CMSX-4 materials**, Materials Science and Engineering A. Vol. 762 pp. 138098 (2019). https://doi.org/10.1016/j.msea.2019.138098.

[61] LUO, S.; HUANG, W.; YANG, H.; YANG, J.; WANG, Z.; ZENG, X. **Microstructural evolution and corrosion behaviors of Inconel 718 alloy produced by selective laser melting following different heat treatments**, Additive Manufacturing. Vol. 30 pp. 100875 (2019). https://doi.org/10.1016/j.addma.2019.100875.

[62] Cao, G.H.; Sun, T.Y.; Wang, C.H.; Li, X.; Liu, M.; Zhang, Z.X.; Hu, P.F.; Russell, A.M.; Schneider, R.; Gerthsen, D.; Zhou, Z.J.; Li, C.P.; Chen, G.F. **Investigations of γ' γ'' and δ precipitates in heat-treated Inconel 718 alloy fabricated by selective laser melting**, Materials Characterization. Vol. 136 pp. 398–406 (2018). https://doi.org/10.1016/j.matchar.2018.01.006.

[63] Special Metals. **INCONEL Alloy X-750**, Special Metals. pp. 1–28 (2004). https://www.specialmetals.com/assets/smc/documents/alloys/inconel/inconel-alloy-x-750.pdf Accessed in: January 30, 2020.

[64] Cardarelli, F. **Materials Handbook: A Concise Desktop Referece**, 2nd ed., Springer London, London, 2008, pp. 1364. https://doi.org/10.1007/978-1-84628-669-8.

[65] Tolochko, N.K.; Khlopkov, Y. V.; Mozzharov, S.E.; Ignatiev, M.B.; Laoui, T.; Titov, V.I. **Absorptance of powder materials suitable for laser sintering**, Rapid Prototyping Journal. Vol. 6 pp. 155–161 (2000). https://doi.org/10.1108/13552540010337029.

[66] Liu, X.; Rutman, D.; Lou, N.; Patole, S.; Wang, Y.; Shi, J. **Experimental Investigation of macro-machinability of Nano-TiC Reinforced Inconel fabrication by Direct Metal Laser Melting**, ASME 2015 International Mechanical Engineering Congress and Exposition IMECE2015. pp. 8 (2015).

[67] Shi, Q.; Gu, D.; Xia, M.; Cao, S.; Rong, T. **Effects of laser processing parameters on thermal behavior and melting/solidification mechanism during selective laser melting of TiC/Inconel 718 composites**, Optics & Laser Technology. Vol. 84 pp. 9–22 (2016). https://doi.org/10.1016/j.optlastec.2016.04.009.

[68] Bakkar, A.; Ahmed, M.M.Z.; Alsaleh, N.A.; Seleman, M.M.E.S.; Ataya, S. **Microstructure, wear, and corrosion characterization of high TiC content Inconel 625 matrix composites**, Journal of Materials Research and Technology. Vol. 8 pp. 1102–1110 (2019). https://doi.org/10.1016/j.jmrt.2018.09.001.

[69] Zhou, J.; Xie, F.Q.; Jia, J.F.; Lin, N.M.; Wu, X.Q. **Microstructure and Dry Sliding Wear Behavior of Laser Cladding (TiC+TiN)-NiCrWC Powder Composite Coating on DZ125 Superalloy**, Advanced Materials Research. Vol. 557–559 pp. 1699–1703 (2012). https://doi.org/10.4028/www.scientific.net/AMR.557-559.1699.

[70] Gopagoni, S.; Hwang, J.Y.; Singh, A.R.P.; Mensah, B.A.; Bunce, N.; Tiley, J.; Scharf, T.W.; Banerjee, R. **Microstructural evolution in laser deposited nickel – titanium – carbon in situ metal matrix composites**, Journal of Alloys and Compounds. Vol. 509 pp. 1255–1260 (2011).

https://doi.org/10.1016/j.jallcom.2010.09.208.

[71] HUEBNER, J.; RUTKOWSKI, P.; KATA, D.; KUSIŃSKI, J. **Microstructural and Mechanical Study of Inconel 625-Tungsten Carbide Composite Coatings Obtained by Powder Laser Cladding**, Archives of Metallurgy and Materials. Vol. 62 pp. 531–538 (2017). https://doi.org/10.1515/amm-2017-0078.

[72] JANICKI, D. **Laser cladding of Inconel 625-based composite coatings reinforced by porous chromium carbide particles**, Optics and Laser Technology. Vol. 94 pp. 6–14 (2017). https://doi.org/10.1016/j.optlastec.2017.03.007.

[73] RAMAKRISHNAN, A.; DINDA, G.P. **Functionally graded metal matrix composite of Haynes 282 and SiC fabricated by laser metal deposition**, Materials and Design. Vol. 179 pp. 107877 (2019). https://doi.org/10.1016/j.matdes.2019.107877.

[74] GONÇALVES, D.A. **A Convolutional Neural Network Approach on Bead Geometry Estimation for a Laser Cladding System**, Universidade Federal de Santa Catarina, PGEAS, 2019, pp. 91.

[75] TURAZI, A. **Metodologia de Avaliação de Grau de Degradação e Rejuvenescimento de Superligas à Base de Níquel**, Universidade Federal de Santa Catarina, PGMAT, 2014, pp. 1–197.

[76] VANDER VOORT, G.F. **Metallography: Principles and Practice**, ASM International, 1984. https://doi.org/10.1361/mpap1999p509.

[77] SALEHI, R.; SAMADI, A.; SAVADKOOHI, M.K. **Influence of Etchants on Quantitative/Qualitative Evaluations of the γ' Precipitates in a Nickel-Base Superalloy**, Metallography, Microstructure, and Analysis. Vol. 1 pp. 290–296 (2012). https://doi.org/10.1007/s13632-012-0043-7.

[78] VOLEK, A. **Erstarrungsmikrostruktur und Hochtemperatureigenschften rheniumhaltiger, stängelkristalliner Nickel-Basis Superlegierungen**, pp. 175 (2002).

[79] MOKADEM, S.; BEZENÇON, C.; DREZET, J.M.; JACOT, A.; WAGNIÈRE, J.D.; KURZ, W. **Microstructure control during single crystal laser welding and deposition of Ni-base superalloys**, Solidification Processes and Microstructures: A Symposium in Honor of Wilfried Kurz. pp. 67–76 (2004).

[80] VANDER VOORT, G.F. **George Vander Voort - Molybdic Acid Reagent**, (2020). https://www.georgevandervoort.com/?s=nickel+alloys.

[81] NENADL, O.; KUIPERS, W.; KOELEWIJN, N.; OCELÍK, V.; DE HOSSON, J.T.M.; HOSSON, J.T.M. DE. **A versatile model for the prediction of complex geometry in 3D direct**

laser deposition, Surface and Coatings Technology. Vol. 307 pp. 292–300 (2016). https://doi.org/10.1016/j.surfcoat.2016.08.090.

[82] DEL RÍO, O.I.; NEUMANN, A.W. **Axisymmetric drop shape analysis: Computational methods for the measurement of interfacial properties from the shape and dimensions of pendant and sessile drops**, Journal of Colloid and Interface Science. Vol. 196 pp. 136–147 (1997). https://doi.org/10.1006/jcis.1997.5214.

[83] RICCI, E.; GIURANNO, D.; NOVAKOVIC, R.; MATSUSHITA, T.; SEETHARAMAN, S.; BROOKS, R.; CHAPMAN, L.A.; QUESTED, P.N. **Density, Surface Tension, and Viscosity of CMSX-4® Superalloy**, International Journal of Thermophysics. Vol. 28 pp. 1304–1321 (2007). https://doi.org/10.1007/s10765-007-0257-0.

[84] BRILLO, J.; EGRY, I. **Surface tension of nickel , copper , iron**, Calphad Computer Coupling Of Phase Diagrams And Thermochemistry. Vol. 0 pp. 2213–2216 (2005).

[85] GARANDET, J.; HAYASHI, M.; MILLS, K.C.; PASSERONE, A.; QUESTED, P.N.; RICCI, E.; SCHMIDT-HOHAGEN, F.; SEETHARAMAN, S.; FECHT, H.-J.; WUNDERLICH, R.K.; GARANDET, J.; HAYASHI, M.; MILLS, K.C.; PASSERONE, A.; QUESTED, P.N.; RICCI, E.; SCHMIDT-HOHAGEN, F.; SEETHARAMAN, S. **Thermophysical Properties of in738Lc , Mm247Lc and Cmsx-4 in the Liquid and High Temperature Solid Phase**, Superalloys 718, 625, 706 and Derivatives 2005. pp. 467–476 (2005).

[86] CZOCHRALSKI, J. **Moderne Metallkunde in Theorie und Praxis**, Springer Berlin Heidelberg, Berlin, Heidelberg, 1924. https://doi.org/10.1007/978-3-642-50742-7.

[87] CARNEGIE MELLON UNIVERSITY. **Dislocation Etching: Polygonization Experiment**, (2020). http://mimp.materials.cmu.edu/rohrer/defects_lab/polygoniz.html Accessed in: February 2, 2020.

[88] MAENG, S.-C. **Dislocations in Sodium-Chloride Crystals**, Zeitschrift Für Naturforschung A. Vol. 21 (1966). https://doi.org/10.1515/zna-1966-0322.

[89] PANDEY, A.; YADAV, B.S.; RAO, D.V.S.; KAUR, D.; KAPOOR, A.K. **Dislocation density investigation on MOCVD-grown GaN epitaxial layers using wet and dry defect selective etching**, Applied Physics A: Materials Science and Processing. Vol. 122 pp. 1–10 (2016). https://doi.org/10.1007/s00339-016-0143-3.

[90] MIURA, N.; KONDO, Y.; KUBUSHIRO, K.; TAKAHASHI, S. **Change in microstructure at grain boundaries with creep deformation of polycrystalline nickel-based superalloy, in-100 at 1273k**, Advanced Materials Research. Vol. 278 pp. 132–137 (2011). https://doi.org/10.4028/www.scientific.net/AMR.278.132.

[91] VANDER VOORT, G.F. **Applied Metallography**, Springer, Boston, MA, 1986.

https://doi.org/10.1007/978-1-4684-9084-8.

[92] VANDER VOORT, G.F. **Metallography of magnesium die-cast alloys**, Metallurgia Italiana. Vol. 94 pp. 37–41 (2002).

APPENDIX A – Metallographic Etchants Testing and Results

The experiments to define which reagent would be used to reveal the microstructure of all non-transmission microscopy came to be divided in three stages, the initial etching tests, the try-outs with the MoO3-based etchant, and the etching time optimization of the adjusted MoO3-based etchant. Below is the list that excludes the final etchant and describes the chemical composition of the ones used in the initial etching tests.

- HF-based [75,76]: 61 ml lactic acid, 36 ml nitric acid (65%) and 3 ml hydrofluoric acid;
- Kalling's no. 2 [76] or Waterless Kalling: 100 ml hydrochloric acid (32%), 100 ethanol and 2 g copper chloride (II);
- Reagent 3 [76,77]; 25 ml nitric acid (65%), 50 ml hydrochloric acid (32%), 200 ml distilled water and 2 g copper chloride (II);
- MoO_3-based [78,79]: 15 ml nitric acid (65%), 100 ml hydrochloric acid (32%), 15 ml distilled water, 1 g Molybdic acid and 5 ml of neutral dish soap;

These etchants were applied through immersion etching during the initial tests. All etching procedures were done at room temperature. Three etching times were set to each, being the time values determined based in information present in the literature. The results were initially evaluated by optical microscopy (OM), followed by SEM from the more promising results. This time the SEM microscope used was the one available at LabMat, model Vega3 from Tescan. The micrographs taken by OM are presented from Figure 50 to 53. When not cited otherwise they are from the substrate of heat-treated samples, since it was simpler to photograph the substrate than the DED-L beads, and since that the addition of this TiC_p volume percentage did not altered etching parameters.

Figure 50 – HF-based etching results.

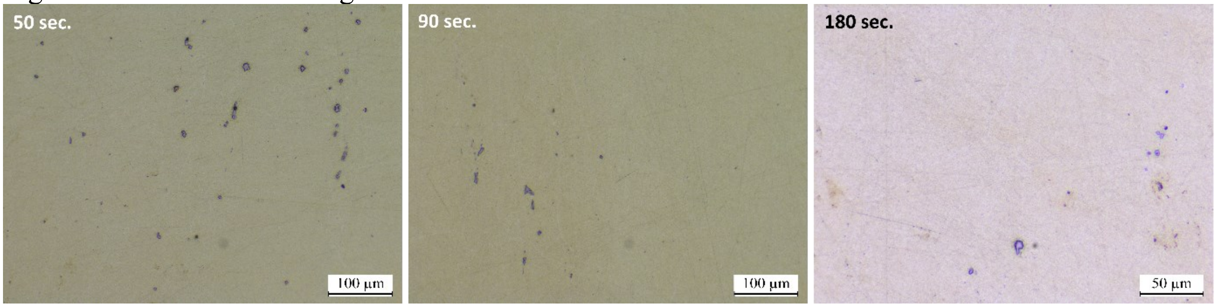

Source: Author

Figure 51 – Kalling’s no. 2 etching results.

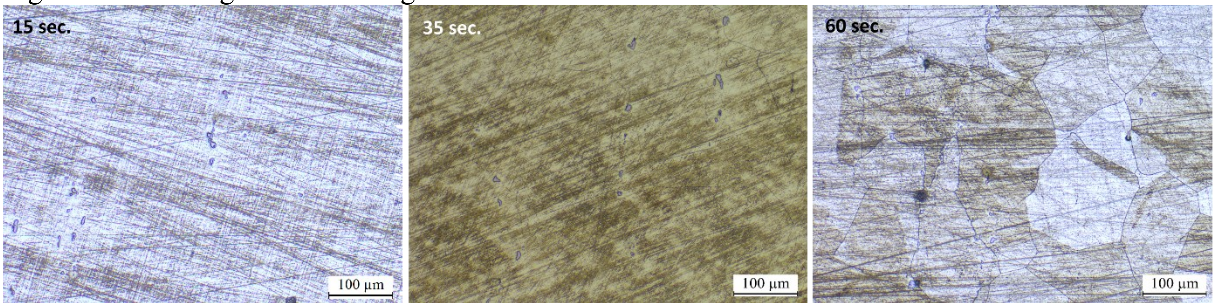

Source: Author

Figure 52 – Reagent 3 etching results.

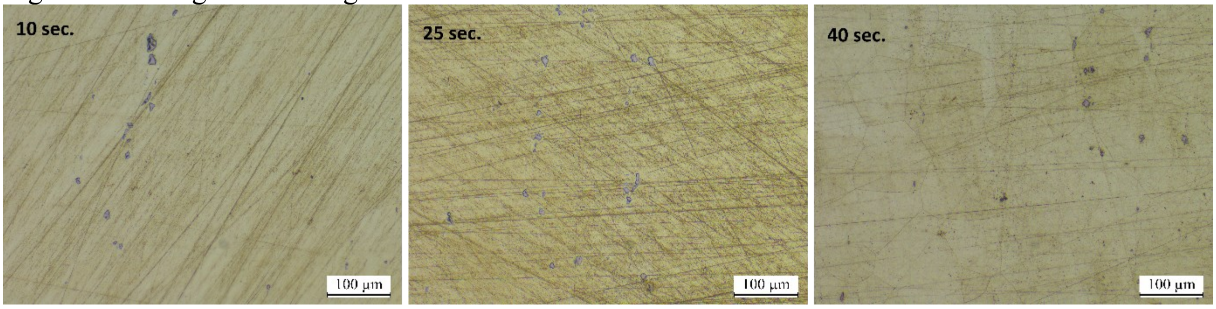

Source: Author

Figure 53 – MoO_3-based etching results.

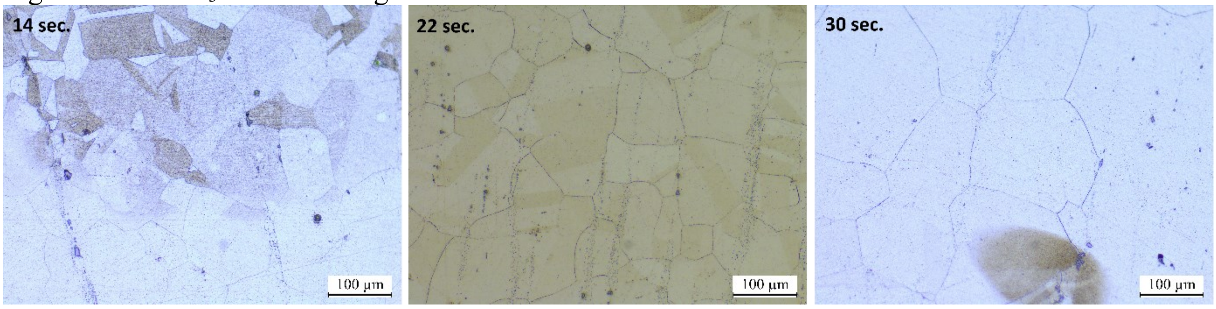

Source: Author

Although only slightly evident in Figure 50, the HF-based etchant revealed the material grain boundaries as whiter lines and proved to have high reproducibility, one of the most important factors in metallographic etching multiple samples.

Kalling’s no. 2 etchant and Reagent 3 revealed scratches in several directions albeit the etchings were done by immersion and that samples were completely polished beforehand. The cause for this was assumed to be tensions inserted during grinding that formed regions susceptible to preferential etching [76,91]. Despite this problem, the samples etched with these reagents for longer periods had their grains revealed by it, while also showing their differences in crystallographic orientation and crystal twinning.

The MoO_3-based etchant revealed no scratch marks while also showing differential etching dependent on crystallographic orientation. Thus, it revealed grain boundaries and crystal twins. However, this etchant did not etch the sample evenly, as it formed spots or regions where it not seemingly reacted with the sample.

Summing up the results from the initial parametrization, no further use was done of Kalling's no. 2 etchant and Reagent 3 or analysis from their etched samples, since too much effort would be necessary to grind them with finer sandpaper grits or polishing agents to avoid the them formed scratches. Only the HF-based and the MoO_3-based etchants were taken to the SEM for analysis, being one micrograph of each depicted at Figure 54. The goal was to observe if and which of these etchants better revealed the γ' precipitates and the material's carbides.

Figure 54 – SEM micrographs of triple points taken from the sample etched with the HF-based etchant through 180 seconds (a) and the one etched with the MoO_3-based etchant along 30 seconds.

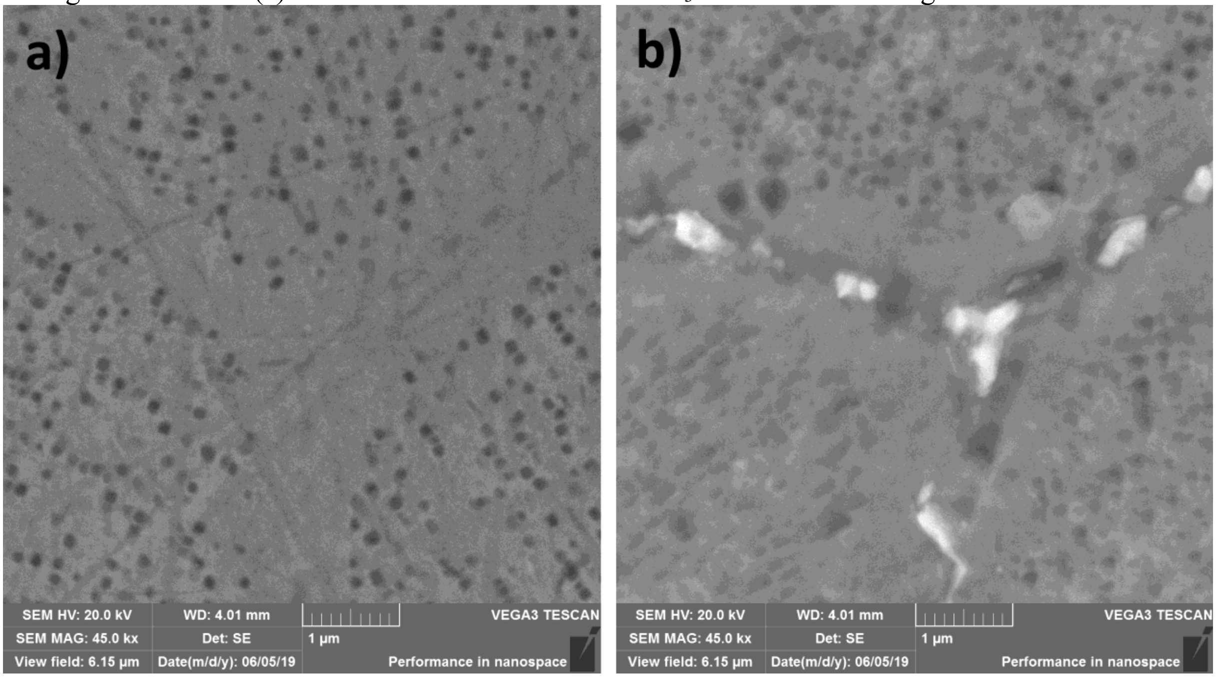

Source: Author

As expect of an etchant based in hydrofluoric acid, the HF-based etchant removed all the ceramic phases present in the sample surface, leaving only light grey marks of where the grain boundaries were. However, it did reveal the gamma prime precipitates as it also etched them out. This etchant was them discarded since it would not allow the evaluation of the added TiC_p, one of this work's main objectives.

The MoO_3-based etchant revealed both γ' precipitates and left the ceramic phases seemingly intact. Thus, satisfactorily revealing the interest phases and grain boundaries. Nonetheless, its problem regarding reproducibility still required attention and, therefore, the second phase in the etching experiments was entered, as several attempts to obtain reproducibility were done. This proved to be a laborious and time-consuming phase, were samples had to be analysed through SEM between each etching time tested. Small changes in etchant composition, such as the removal or substitution of the surfactant and reduction of MoO_3 content were attempted, leading to a certain degree of improvement. Immersion etching was replaced by swabbing with cotton puffs, and although results were promising no solution was found to the scratching that was caused by the cotton during etching. This scratching phenomenon by such soft materials was surprising, especially since it perfectly followed the swabbing path done with the cotton. This phenomenon is reported in metallographic preparation of Mg-alloys [92]. Some of the etching defects found are depicted in the following at Figure 55.

Figure 55 – Etching defects found while experimenting with the MoO_3-based etchant; bubble like spots (a), uneven etching (b) and scratches from swabbing with cotton puffs (c) and (d).

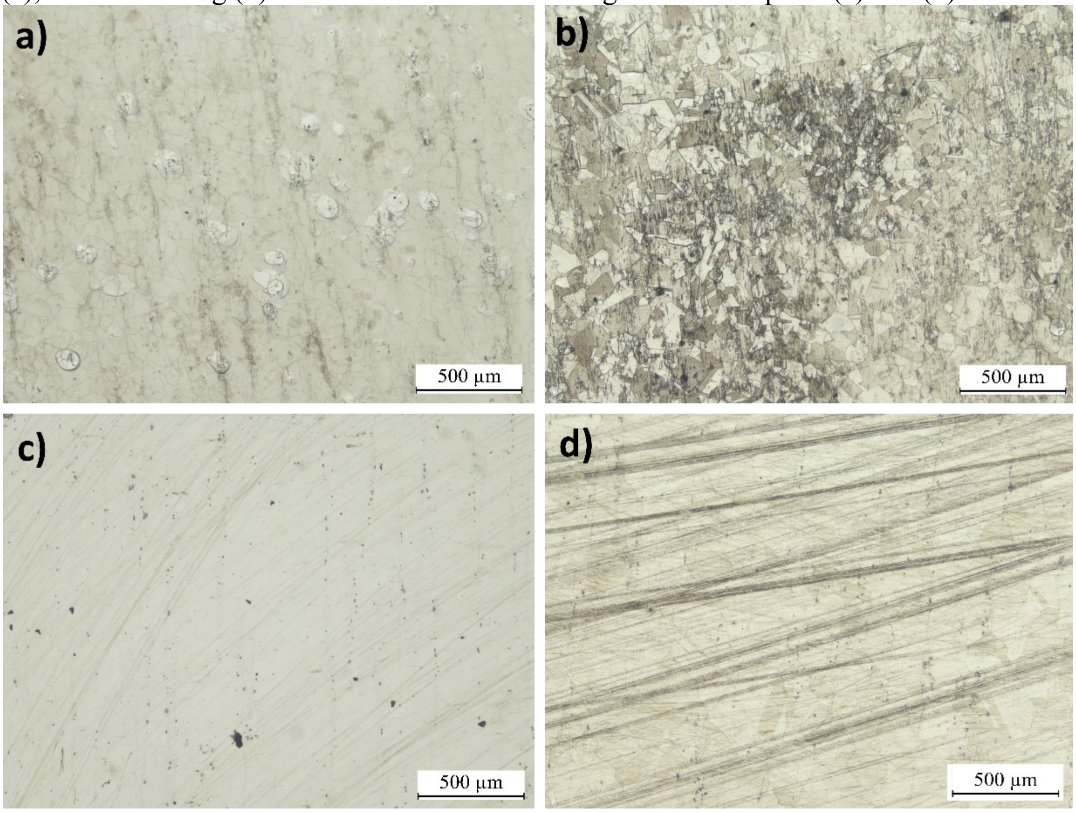

Source: Author

After concluding that it was the cotton puffs that were scratching the sample, a solution was devised by using long-stringed lens cleaning tissues to perform the swabbing. This combined with an adjusted etchant composition finally provided a reliable etching procedure which revealed the target microstructure. Long and straight and strokes while rotating the sample are recommended. The final chemical composition of the etchant used was 30 ml nitric acid (65%), 30 ml hydrochloric acid (32%), 30 ml distilled water and 0.3 g Molybdic acid; as described in the main part of this work. The surfactant was removed, since this allowed etchant storage. Etching time was set to 150 seconds, as it seemed that longer would not improve etching or would start degrading it. The microstructure reveal progression is depicted at Figure 56 by images taken on the lower amplification MEV.

Figure 56 – Etching time and effect for the adjusted MoO3-based etchant.

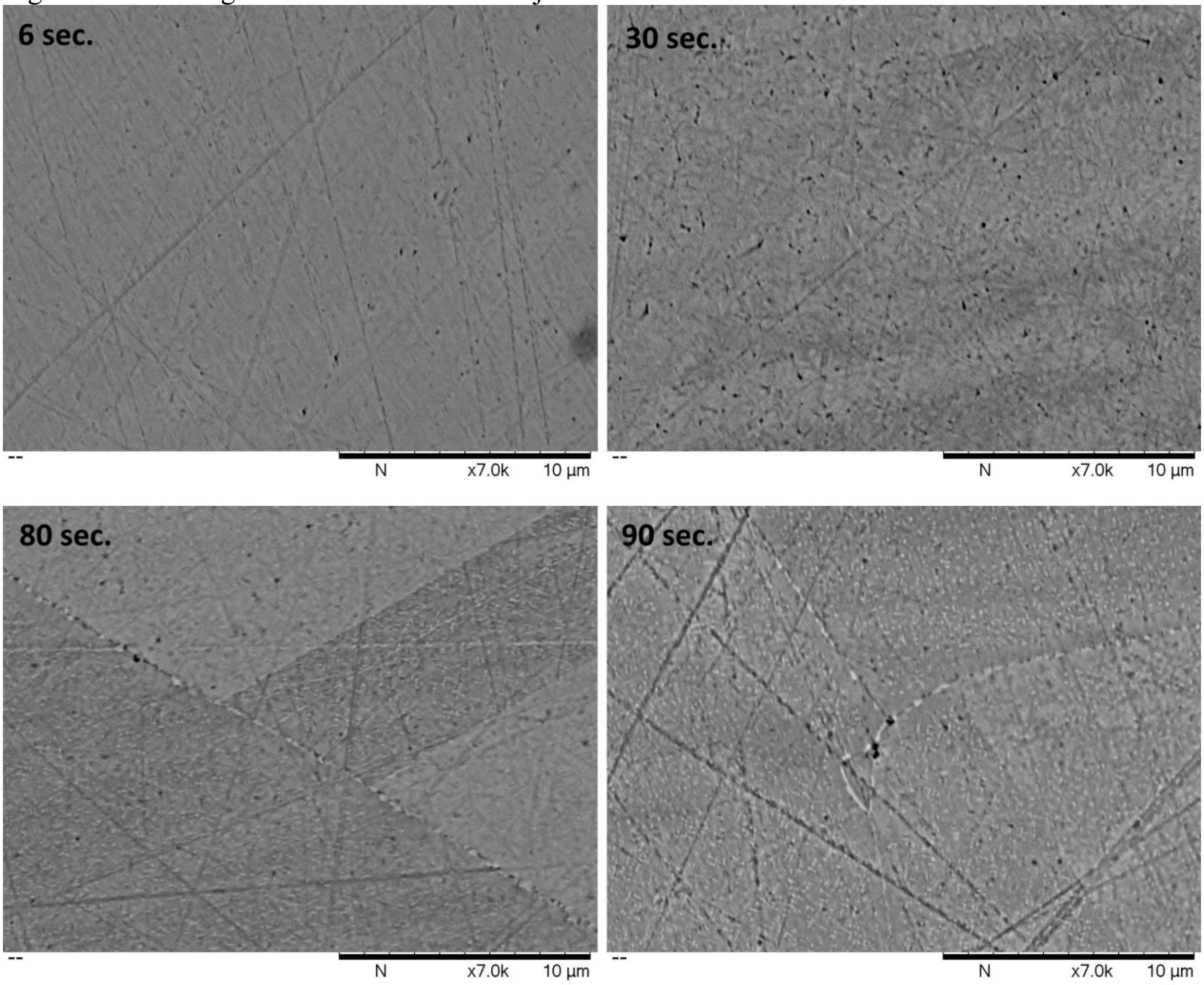

Source: Author

Figure 56 – Continuation. Etching time effect for the adjusted MoO_3-base etchant

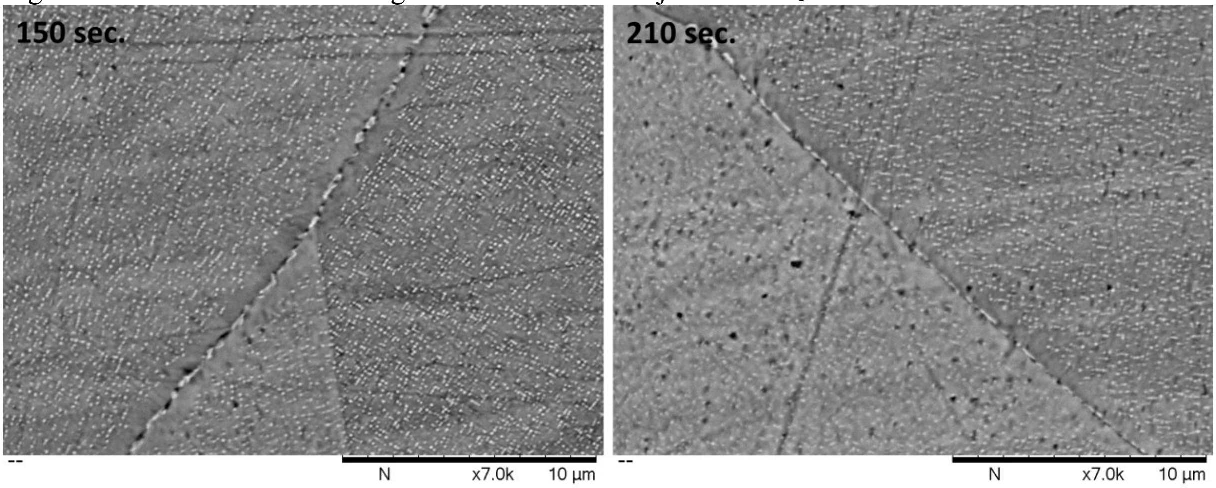

Source: Author

The adjusted MoO_3-based etching caused the sample to present a slight yellow tint to the naked eye. A micrograph of an MMC DED-L bead showing the primary γ' precipitates and the TiC_p, prepared with this etchant and procedure, is depicted at Figure 57.

Figure 57 – FEG-SEM Micrograph of an MMC bead prepared with the adjusted MoO_3-based etchant

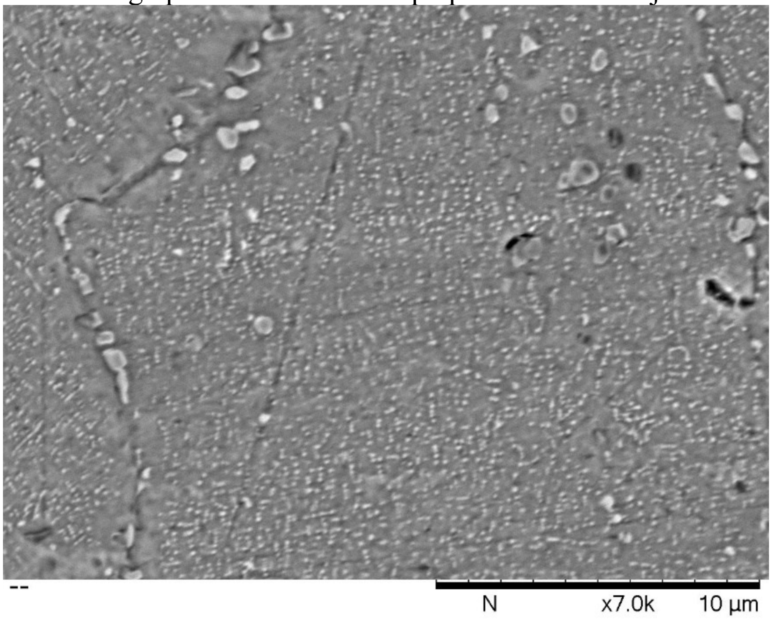

Source: Author

APPENDIX B – Sample Preparation and Electropolishing Procedure for Transmission Electron Microscopy of Inconel X750-base TiC$_P$-reinforced MMCs

DISCLAIMER NOTE: The procedure described below is only a guideline given with the best of intentions to help future researches, however, the author does not assume any responsibility regarding its use or interpretation. Regardless of the described in this procedure, always follow standardized and recommended safety procedures given by competent organizations or institutions.

The following procedure was based and optimized from the knowledge of co-workers, the doctor thesis of Almir Turazi [75], the ASTM standard E1558 and previous experiments performed by Guilherme Maziero Volpato:

1. Depending on initial sample size, perform cutting with a metallographic precision disc-saw, EDM-machine or diamond wire cutter to form 0.5 mm thick plates. If necessary, sand the resultant plates to achieve flat surfaces with roughness as if they were grinded with a Mesh 120 – sandpaper;
2. Prepare both sides of the sample sides using a Disc Grinder (exemplars found in LCME or LMP). Each sample side must be grinded to Mesh 1200 and polished with 3 or 1 μm diamond paste. The target sample thickness must lie between 80 and 150 μm. Check sample thickness with a micrometre, not a calliper. Regardless of the thickness achieved, it is highly recommended to leave all samples with similar thicknesses, as this factor affects electropolishing results and parametrization;
3. Cut the polished plates with a disc puncher (found at LCME) forming discs with 3 mm in diameter. Depending on plate size it is possible to generate several TEM samples from the same plate.
4. Electropolishing reagent preparation:
   - Supervision of the entire reagent handling and preparation, and the use of Electropolisher (TenuPol-5) by an experienced operator is strongly recommended. Never handle harmful chemical reagents alone. Always have someone present or close to provide assistance in case of an accident.
   - The chemical used was a mixture of a third of methanol with two thirds of nitric acid (65%) at -10°C, as described at standard ASTM E1588-09 for when polishing aluminium alloys. If this reagent fails, other options may prove viable. This reagent is normally used for aluminium-based samples. Both methanol and

nitric acid are highly toxic, check their handling safety instructions and hazard warnings in datasheets provided by suppliers;

- The minimum volume of reagent for the operation of TenuPol-5 is one litre. This volume can be reused, but its use must be restricted to a type of material to avoid contamination (e.g. super alloys or steels). A small portion of the reagent is always lost in each preparation, so it is recommended that more than the minimum volume be produced;
- The preparation of the nitric acid and methanol mixture must be carried out according to the following steps in order to avoid accidents:
    i. The use of personal protective equipment is imperative (full face mask, powder-free nitrile gloves, long sleeve lab coat with elastic bands, long pants and closed shoes);
    ii. Always handle liquids exposed to the atmosphere inside the chapel.
    iii. Measurement of volumes should be done before mixing them. This prevents unnecessary handling of large volumes of harmful reagents.
    iv. The final mixture must be carried out by pouring the acid into the alcohol, the latter being inside a beaker with the capacity to contain the volume of the two reagents. An increase in temperature of the mixture is expected, but this increase should not become high enough that it does not allow the beaker to be handled. For one litre of reagent, 30 seconds were spent adding one reagent to the other and no problems due to excessive heating were found (CNTP).
    v. After mixing the two reagents, they must be completely poured into a vial that allows the reagent to be sealed. This sealed flask must be immediately immersed in a cold bath, with temperatures below minus 10ºC in order to control the exothermic reaction resulting from reagent mixing. For the case in question, an ice bath (10 kg) with salt (1 kg) and a small portion of water and ethanol (50 ml each) was used, reaching temperatures below -14ºC. The bath was produced inside a thermal box made of Styrofoam.
    vi. For one litre of this reagent, the waiting time until it reaches the temperature required to perform the electro polishing (-10ºC), was from five to seven hours. Colling must be started right after mixing.

5. Electrolytic polishing:

- The part of TenuPol-5 that contains the corrosion cell must remain inside the chapel during processing and when contaminated with the reagent.
- The tested electrolytic polishing parameters that obtained the acceptable results are found in Table 10:

Table 10 – Range of electropolishing parameters tested which present acceptable results

Etchant Initial Temperature (⁰C)	**Polishing Time (s)**	**Sample Thickness (µm)**	**Applied Voltage (V)**	**Automatic Hole Detection**
-3.4 to +1.2	26 to 100	70 to 100	4.5 to 5	Yes

Source: Author

- The best electropolishing parameter set had etchant initial temperature equal to 2.2°C, polishing time of 27 seconds, sample thickness around 70 µm, used automatic hole detection and an applied voltage of 5V.
- Right after electropolishing and before removing sample from the support, carefully immerse it three times in methanol and once in ethanol to wash off residues and reagent droplets.
- Remove sample from the support with delicate and fine-tipped tweezer, use preferably inverse tweezers, in order not to exaggerate the pressure and bend the sample. The sample is extremely fragile at this state;
- It is recommended to analyse the sample at the TEM up to two days apart from the day when the electrolytic polishing was performed;
- The sample must be transported inside a closed Petri dish - or equivalent - over a plain paper, which was cut in dimensions suitable for handling.
- Do not forget to clean the TenuPol-5 and the environment of any harmful reagents before leaving the laboratory. Store the reagent in a dedicated and refrigerated compartment around 4°C to contain evaporation.

6. Recommended amplifications at the JEM1011 TEM:

    - 80.000X for overall microstructure comparison.
    - 500.000X for secondary γ’ precipitate morphology (~10 nm).